POLITECNICO DI TORINO

Master's degree course in Structural Civil Engineering

Thesis of master's degree


# Influence of ground motion characteristics on the optimal single concave sliding bearing properties of isolated continuous bridges

Supervisor: PhD. Eng. Castaldo Paolo

Candidate:

Sabino Soldani 223332

March 2018

*“Un vincitore*

*è semplicemente*

*un sognatore*

*che non si è mai arreso”*

***Nelson Mandela***

# THANKSGIVINGS

To my parents, Mario and Maria, who have allowed me to support my studies economically and morally over the years to reach this great aim.

To Teresa that was next to me to share every moment for the whole university career.

To my classmates Daniele, Alessandro, Silvio and Ilmi with whom I shared this experience full of satisfactions but also difficulties.

To my supervisor Paolo Castaldo for the trust, patience, humility and professionalism with which we have dealt with this work.

To myself for persevering and for the sacrifices I had to make to achieve this fantastic goal that will only be the beginning of something bigger.

# Index of contents

# ABSTRACT

The following work of thesis examines the influence of ground motion characteristics on the optimal friction properties of single concave sliding bearings employed for the seismic isolation of the structural systems. The evaluation of the optimal properties is carried out by considering a non-dimensional formulation which employs the peak ground acceleration (PGA) and the peak ground acceleration-to-velocity (PGA/PGV) ratio as ground motion parameters. A six degree of freedom (5+1 d.o.f) model is employed to describe the isolated system and the two different families of records representative respectively of near fault and far field seismic inputs are considered. Following the nondimensionalization of the equation of motion for the proposed ground motion parameters, it is shown that the non-dimensional response obtained for the two types of seismic inputs are similar. This result confirms that PGA/PGV is a good indicator of the frequency content and of other characteristics of ground motion records, helping to reduce the scatter in the response. Regression expressions are also obtained for the optimal values of the friction coefficient that minimizes the superstructure displacements relative to the base as a function of the abovementioned ground motion parameter and of the dimensionless system parameters. These expressions can be used for the preliminary estimation of the optimal properties of isolation bearings with a single concave sliding surface.

# 1. BASIS OF SEISMOLOGY

## 1.1 Seismic ground classification of Italy

The seismic ground classification of Italy consists in a partition of the Italian country in some specific areas, characterized by a common seismic hazard.
Currently, the seismic area classification of the country survives only for statistical and administrational reasons. Indeed, with the codes, becomes law on 2009, it means the NTC 08 ones, after the earthquake interested the city of L'Aquila, with referring to seismic design, nowadays it is used a new method to determine the seismic hazard based on statistical point by point approach. Therefore, every point of the country is characterized from a precious value of peak ground acceleration (PGA) depending on a return period time which is the interval of time that on average is between two events with the same intensity or go beyond a fixed intensity value.

Previously, according to the provision taken on 2003 (Ordinanza del Presidente del Consiglio dei Ministri n. 3274 del 20 marzo 2003), every Italian district has been classified in four main categories, suggestive with referring of their seismic hazard, based on the peak ground acceleration, event frequency and intensity measure. Moreover, the district classification is continuously undergoing an update every time that new territorial studies have been made by the region of pertinence or for statistical variation over a long time. So, the four categories are:

- Zone 1: High seismicity (PGA > 0.25g), involving 708 districts,
- Zone 2: Medium-High seismicity (0.15g<PGA<0.25g), involving 2345 districts with some exceptions for few district of Toscana,
- Zone 3: Medium-low seismicity (0.05<PGA<0.15g), involving 1560 districts,
- Zone 4: low seismicity (PGA<0.05g), involving 3448 districts.

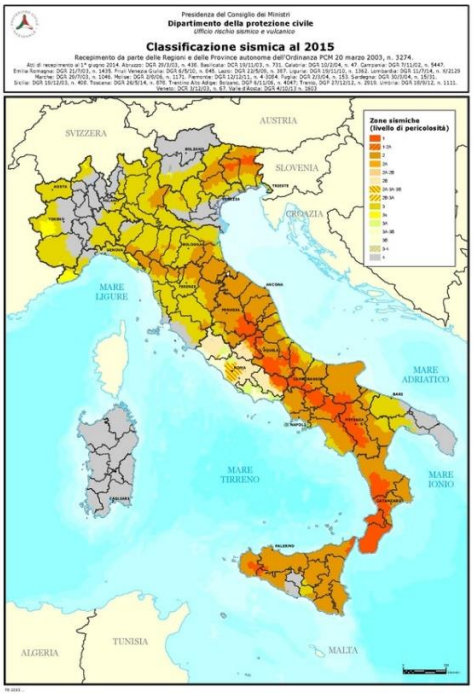


Figure 1-Seismic hazard classification map of Italy

Although, with the introduction, of D.M. on the 14/01/2008 (Norme tecniche per le Costruzioni), it has been defined a new method to determine the seismic hazard of each site, and then for evaluating the seismic design action for new and existing constructions. In particular, they have been developed seismic hazard maps in terms of PGA, with probability of exceedance in fifty years amounting to: 81%, 63%, 50%, 39%, 30%, 22%, 10%, 5% and 2%, corresponding respectively to the return periods of 30, 50, 72, 101, 140, 201, 475, 975 and 2475 years. Each processing led to generating the hazard curves that represent the median (50th percentile), the 16th and the 84th percentile of the distribution of the PGA values.

## 1.2 Characterization of earthquakes

The movements of the tectonic plates make, at the depths of the earth's crust, stress condition and storing of elastic energy, so when the material, composing the layers of the crust, reach its strength limit, the elastic stored energy is released and generates a fracture, which is renamed fault, and earthquakes.

The point in which the earthquake takes place is the hypocentre, the seismic source, and its projection on the earth's surface is the epicentre one. With respect to the site of recording of seismic waves they can be defined two kinds of distances, the hypocentral and epicentral distances, which respectively are the distance between the hypocentre and the point of the site and the one between

the epicentre and the point of the site again, meanwhile the distance between this last two is called focal depth.

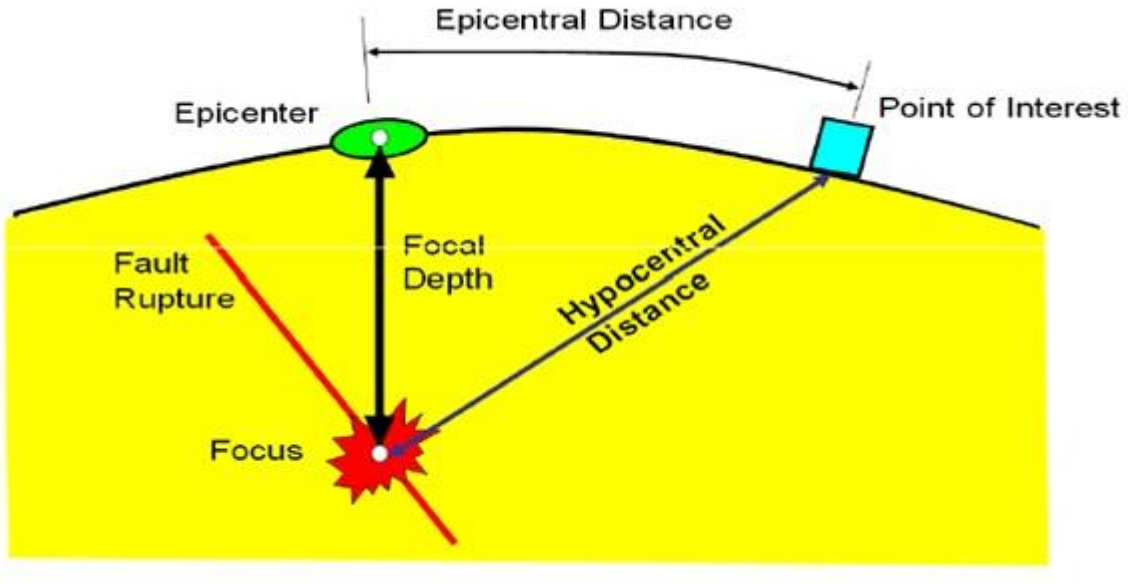


Figure 2-Seismic source and relative distances from the site

The energy released from the hypocentre is spread through the soil as acoustic body wave reaching the earth's surface while dissipate their energy. These waves can be distinguished between:

- Longitudinal waves: also noted as primary waves or P waves, moving with a speed between 1.5 and 8 km/s through the earth's crust. These are the first recorded by the seismograph and are compressional waves. The P waves speed can be determined with the expression $v_p = \sqrt{((k + 3/4 * \mu)/\rho)}$, where $k$ is the incompressibility modulus, $\mu$ is the tangential elastic modulus and $\rho$ is the density of the material crossed.

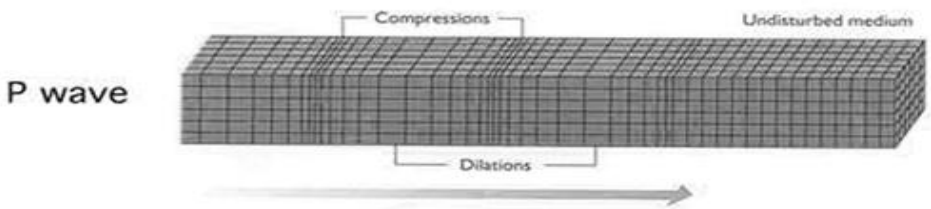


Figure 3-P waves

- Transversal waves: also noted as secondary waves or S waves, moving slower than the primary ones, usually with the 60% or 70% of the speed of the P waves. These are the second recorded by the seismograph and are shear waves. The S waves speed, whereas, is given by $v_s = \sqrt{\mu/\rho}$, where it can be deduced, missing the k contribution, why is lower than the P one.

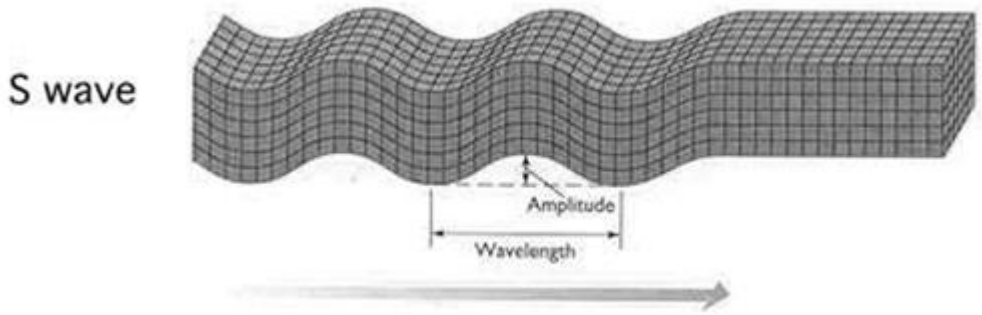


Figure 4-S waves

Once the previous explained waves got to the earth's surface, generate two other types of waves. These are called superficial waves and induce shear stresses in the ground which produce the majority of the damages in presence of a seismic event, they are:

- Rayleigh's waves: cause the surface particles to move in ellipses in planes normal to the surface and parallel to the direction of propagation, the major axis of the ellipse is vertical. At the surface and at shallow depths this motion is retrograde, that is the in-plane motion of a particle is counter clockwise when the wave travels from left to right.

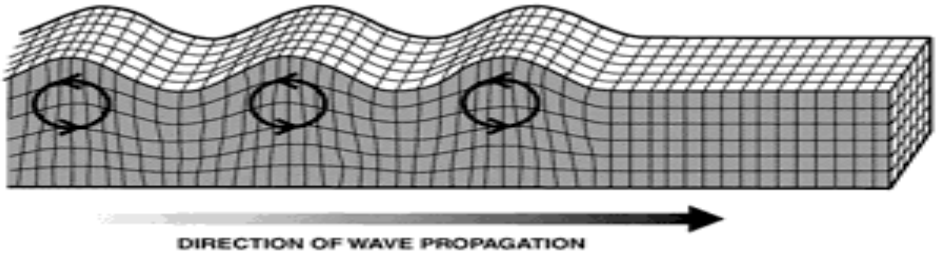


Figure 5-Rayleigh waves

- Love waves: cause the particles to move in the horizontal plane to the surface and transversal to the direction of propagation. The movements of the particles decay with the depths.

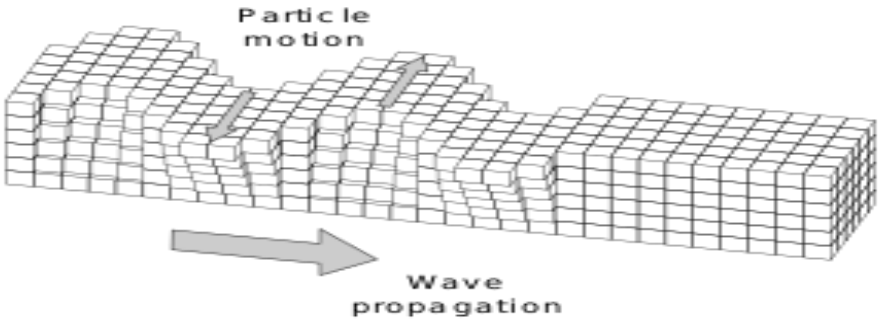


Figure 6-Love waves

It is, also, possible to estimate the time passing between the P and S waves, reading it on the graph carried out from the seismograph or with a simplification knowing two speed waves and the distance between the epicentre and the site of recording.

$$Dt_{S-P} = d \cdot \left(\frac{1}{v_s} - \frac{1}{v_p}\right) \tag{1.1}$$

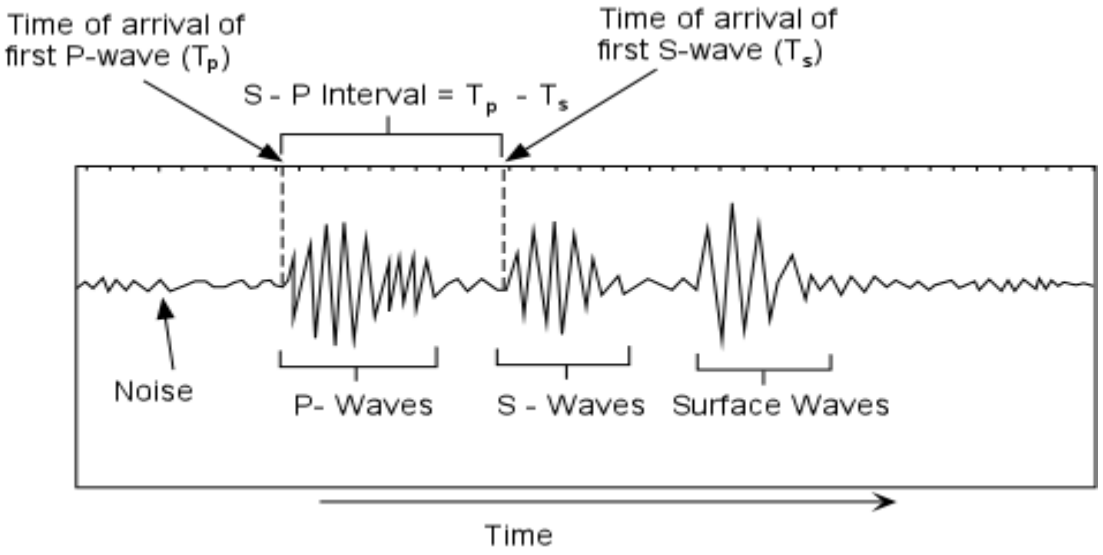


Figure 7-Succession time of waves

On the other hand, depending on the depth of the hypocentre, the earthquakes can be classified as following:

- Superficial earthquakes: with hypocentre between 0 and 70 km far from the earth's surface. They represent about the 85% of the earthquakes recorded every year.

- Medium earthquakes: with hypocentre between 70 and 300 km far from the earth's surface. They represent about the 12% of the earthquakes recorded every year.

- Deep earthquakes: with hypocentre beyond 300 km far from the earth's surface. They represent about the 3% of the earthquakes recorded every year.

Nevertheless, they can be also classified depending on the epicentral distance:

- Local earthquakes: with a distance smaller than 100 km;

- Regional earthquakes: with a distance between 100 and 1500 km;

- Upper mantle earthquakes: with a distance between 1500 and 3000 km;

- Teleseismic earthquakes: with a distance bigger than 3000 km.

## 1.3 Local seismic response

As before explained, the seismic waves have different characteristics based on the depth of the layer that have to cross and with the equality of the other factors, so the waves reaching the site at a moderate epicentral distance, up to 25 km called “near-fault” shocking waves, produce larger effects than the waves coming far from more than 25-50 km called “far-field ones.

The seismic waves attenuate with the increasing of the epicentral distance, in fact, whether in proximity of the epicentre it may have huge damages on the structures, but moving away, it can be appreciated the diminishing of the damages. The law which rules this phenomenon is the law of attenuation.

The law of attenuation depends on the type of soil that has to be crossed by seismic wave, but this may be very different from one site to each other. So, the soil can change suddenly its geological features point by point, therefore it may cause a variation in the way of propagation of the seismic waves even if the sites are very close to each other, in this case it is talking about local seismic response.

Furthermore, depending on the type of the soil and its characteristics there may occur various scenarios, such as local amplification effects in presence of alluvial soil, liquefaction phenomenon of the soil due to increasing of interstitial pressure inside a not cohesive soil (i.e. sand, gravel) causing the loss of strength and shear rigidity as consequence of shocking waves and permanent deformations, and landslides in presence of slopes with high acclivity consisting in detritus or silty soil.

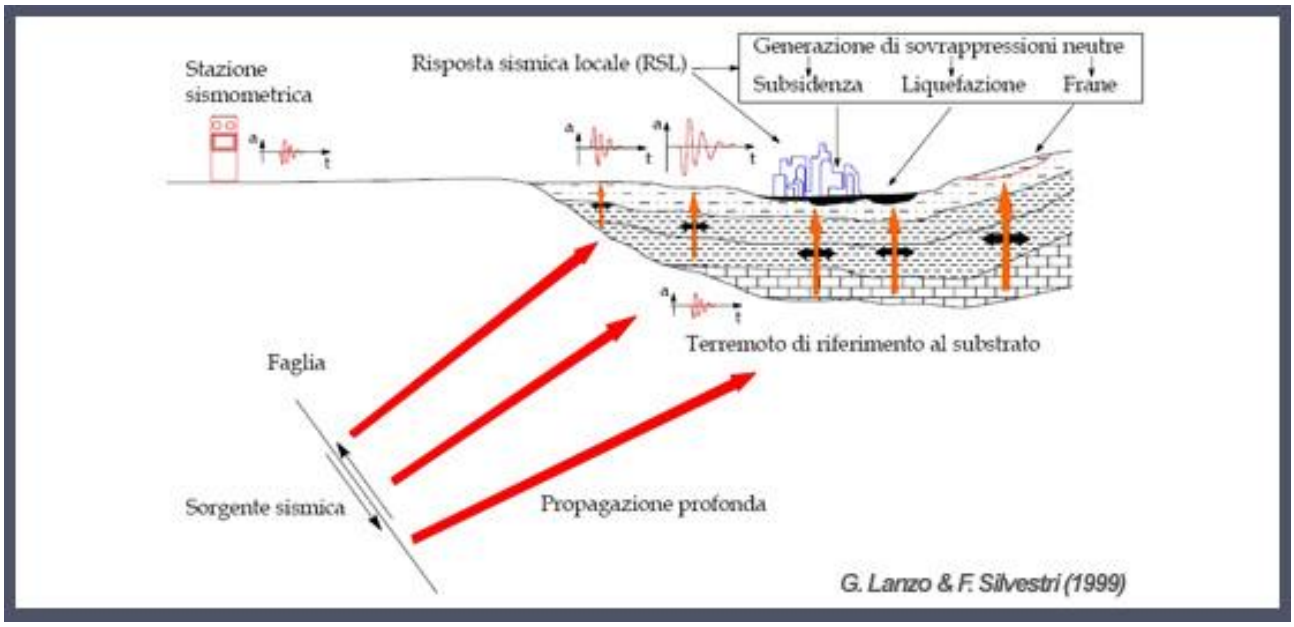


Figure 8-Seismic local response and relative effects

Moreover, it has to be taken into account the possible problem of double resonance that take place when the natural frequency of the soil is close to the one of the structures. In these conditions, it means during an earthquake, both soil and structures start to oscillate at the same frequency, so the oscillation amplitudes tend towards the failure of the structures.

As a first approximation the natural frequency of the soil, whether it is composed of an only homogeneous layer placed on rigid lower layer can be evaluated with the following expression:

$$Ts = 4 * \frac{H}{v_s} \tag{1.2}$$

where $H$ is the depth of the layer given in m and $v_s$ is the speed of the shear waves given in m/s.

# 2. EVALUATION OF SEISMIC ACTION

## 2.1 Elastic seismic response

According to this last provision, the country has been detached by means of a mesh with steps of 5 km. For each node of the mesh, the parameters required for the construction of elastic response spectrum with reference to the limit states provided by the performance-based design method. By means of a technique of interpolation among the nodes of the mesh closer to the site, it is possible to attain this few parameters which are:

- the peak ground acceleration ($a_g$) at the bedrock, depending on the specific limit state and its probability of exceeding associated in the reference period ($V_R$)
- the maximum amplification factor ($F_o$)
- the value of the period where the section with constant velocity starts ($T_c^*$)

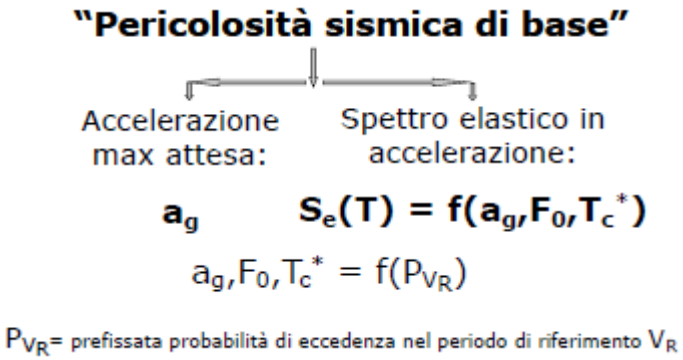


Figure 9-Initial seismic hazard

$$S_e(T) = f(a_g, F_0, T_c^*)$$

**Tabella 3.2.I** – *Probabilità di superamento $P_{V_R}$ al variare dello stato limite considerato*

| Stati Limite | | $P_{V_R}$ : Probabilità di superamento nel periodo di riferimento $V_R$ |
|---|---|---|
| Stati limite di esercizio | SLO | 81% |
| | SLD | 63% |
| Stati limite ultimi | SLV | 10% |
| | SLC | 5% |

Figure 10-probabilities of exceeding

Furthermore, to reach the elastic response spectrum it has to pass through some coefficients that take into account the importance of the construction and the properties of the site.

The first ones depend on the using classes of the construction and structure life reference time ($V_R$) that permit to evaluate the design life time of the structure ($V_N$), so there are four using classes, each one, representing the strategical value of the structure that has to be considered:

- Class I: structure rarely used or not used at all,
- Class II: structure frequently used and with normal crowd,
- Class III: structure very frequently used and/or with significant crowd,
- Class IV: strategical structures (Hospitals, military base, bridges, etc) very frequently used and/or with significant crowd

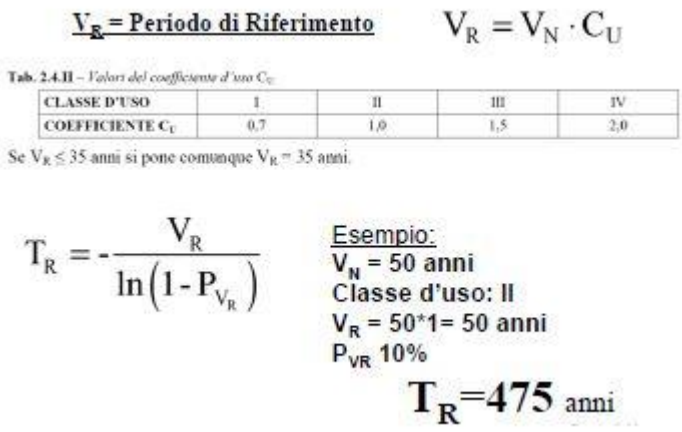


Figure 11-Period of return

Whereas, the second ones depend on the morphology of the ground at the site, it means the topographical and subsoil features that permit to calculate the effective constant velocity period ($T_c$) and the soil coefficient (S).

As regards the topographical coefficient $S_s$ and $C_c$, it distinguishes among five kinds of subsoil characterized with their shear wave velocity diffusion at 30 meters depth ($V_{s,30}$), hit number of standard penetration test ($N_{spt}$) and the undrained shear resistance ($c'_u$), these are:

- Soil A: $V_{s,30} > 800m/s$;
- Soil B: $360m/s < V_{s,30} < 800m/s,\ \ N_{spt} > 50,\ \ \ c'_u > 250kPa$;

- Soil C: $180m/s < V_{s,30} < 360m/s,\ 15 < N_{spt} < 30,\ 70kPa < c'_u < 250kPa$;
- Soil D: $V_{s,30} < 800m/s,\ \ N_{spt} < 15,\ \ c'_u < 70$;
- Soil E: subsoil like C and D ones with 20 meters depth over soil A layer.

Actually, there are two special subsoil classes, not mentioned in the previous classification, which are:

- S1: $V_{s,30} < 100m/s, 10kPa < c'_u < 20kPa$, which includes a layer of at least 8 meters depth of fine soil with low compactness or at least 3 meters depth of peat or highly organic clay,
- S2: soil sensitive to liquefaction and/or not mentioned in the previous classes.

$$S = S_S \cdot S_T \qquad T_C = C_C \cdot T_C^*$$

Tabella 3.2.V – *Espressioni di* $S_S$ *e di* $C_C$

| Categoria sottosuolo | $S_S$ | $C_C$ |
|---|---|---|
| A | 1,00 | 1,00 |
| B | $1,00 \le 1,40 - 0,40 \cdot F_0 \cdot \frac{a_g}{g} \le 1,20$ | $1,10 \cdot (T_C^*)^{-0,20}$ |
| C | $1,00 \le 1,70 - 0,60 \cdot F_0 \cdot \frac{a_g}{g} \le 1,50$ | $1,05 \cdot (T_C^*)^{-0,33}$ |
| D | $0,90 \le 2,40 - 1,50 \cdot F_0 \cdot \frac{a_g}{g} \le 1,80$ | $1,25 \cdot (T_C^*)^{-0,50}$ |
| E | $1,00 \le 2,00 - 1,10 \cdot F_0 \cdot \frac{a_g}{g} \le 1,60$ | $1,15 \cdot (T_C^*)^{-0,40}$ |

Figure 12-Topographical coefficients $S_T$ and $C_c$

Meanwhile, as concern, the topographical coefficient ($S_s$) can be determined with local response analysis for complex topographical ground condition or a simple classification for superficial soil configurations as exposed in the categories below:

- T1: flat area, slopes and isolated elevations with a mean inclination of $i < 15°$;
- T2: slopes with a men inclination of $i > 15°$;
- T3: elevations with much larger width at the top side than the base and a mean inclination of $15° < i < 30°$;
- T4: elevations with much larger width at the top side than the base and a mean inclination of $i > 30°$.

$$S = S_S \cdot S_T \qquad T_C = C_C \cdot T_C^*$$

**Tabella 3.2.VI** – *Valori massimi del coefficiente di amplificazione topografica* $S_T$

| Categoria topografica | Ubicazione dell'opera o dell'intervento | $S_T$ |
|---|---|---|
| T1 | - | 1,0 |
| T2 | In corrispondenza della sommità del pendio | 1,2 |
| T3 | In corrispondenza della cresta del rilievo | 1,2 |
| T4 | In corrispondenza della cresta del rilievo | 1,4 |

**Tabella 3.2.IV** – *Categorie topografiche*

| Categoria | Caratteristiche della superficie topografica |
|---|---|
| T1 | Superficie pianeggiante, pendii e rilievi isolati con inclinazione media $i \leq 15°$ |
| T2 | Pendii con inclinazione media $i > 15°$ |
| T3 | Rilievi con larghezza in cresta molto minore che alla base e inclinazione media $15° \leq i \leq 30°$ |
| T4 | Rilievi con larghezza in cresta molto minore che alla base e inclinazione media $i > 30°$ |

Figure 13-Topographical coefficients $S_s$

Finally, with all these information, it is easy to construct the elastic spectrum response of acceleration that is made of four paths:

- Linear increasing path
- Constant acceleration path
- Constant velocity path: it is a not linear function displayed on acceleration-period graph.
- Constant displacement path: it is a not linear function displayed on acceleration-period graph.

Beside the elastic response spectrum response of acceleration there other two spectrums which are derived from the previous multiplying it, appropriately, for the frequency of the structure ($\omega_s$).

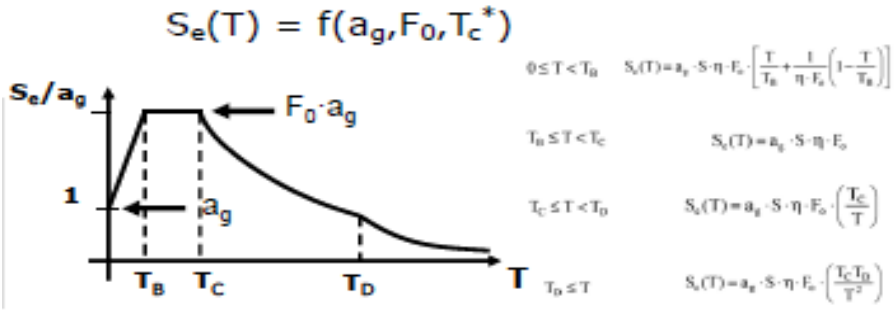


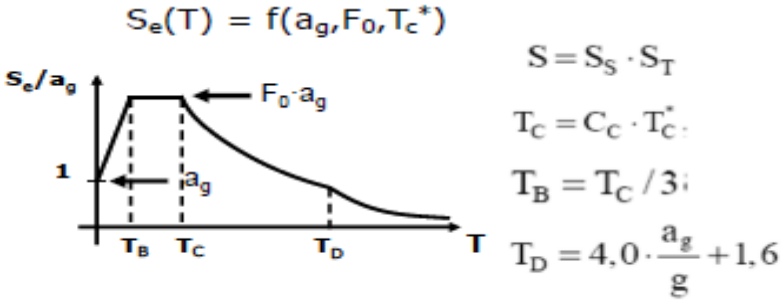


Figure 14-Elastic response spectrum laws and relative characteristic periods

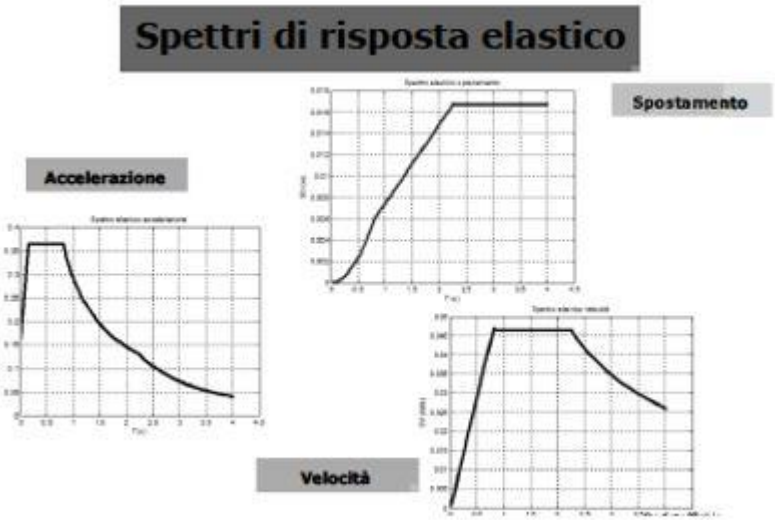


Figure 15-Elastic response spectrum in terms of accelerations, velocities and displacements

## 2.2 Design response spectrum

It is already explained in the previous chapters, how the seismic action, for structures within the elastic field behaviour, has to be evaluated.

Nevertheless, the structures can go beyond the limit of elastic field behaviour, showing some capacities in the plastic field. This behaviour is possible for those structures composed with materials able to, such as steel and reinforced concrete that exploit the plastic capacities of the steel.

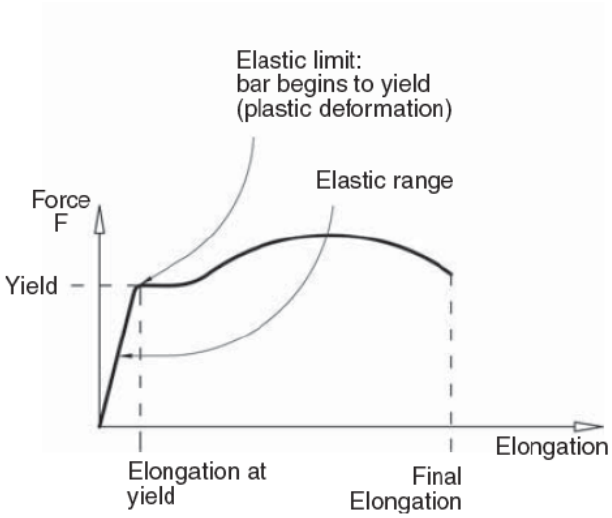


Figure 16-Force-displacement steel behaviour

Therefore, admitting this kind of behaviour, these structures can show high deformations under relatively low forces carried by the earthquakes, this means that the structural system starts to absorb the energy of the earthquake through hysteretic cycles, where the energy absorbed is given as the area circumscribed within these cycles displayed in a force-displacement graph.

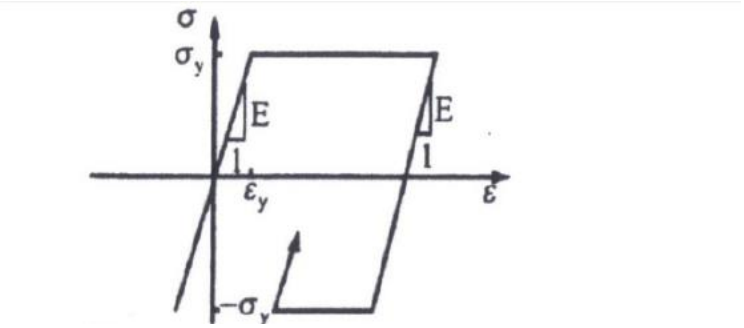


Figure 17-Elastic-plastic hysteretic cycle for steel

Thanks to this phenomenon, it can be achieved another spectrum derived from the elastic one which is called design response spectrum. It has to be defined a coefficient that resumes this plastic capacity of the structure, it is called structure factor q. Such coefficient is correlated to the ductility of the structure through two single degree of freedom systems models representing the structure, so one of them works in the elastic field (elastic oscillator) and the other in the elastic-plastic one (elastic-plastic or inelastic oscillator). The correlation between the structure factor (q) and the ductility ($\mu$) is carried out following two different hypotheses:

- Equal displacement: for very flexible structures

- Equal energy dissipation: for relatively rigid structure

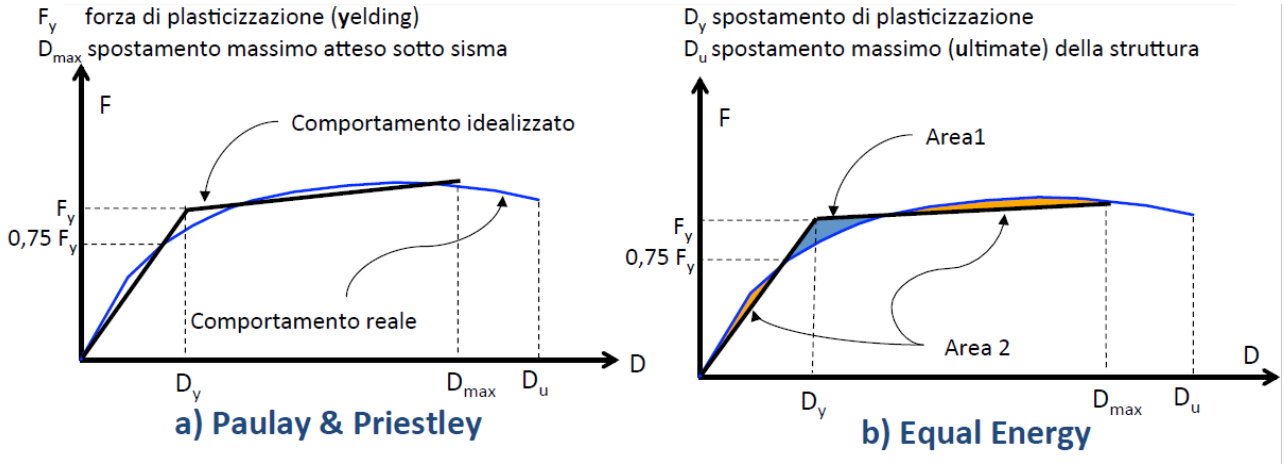


Figure 18-a) Equal displacements criterion, b) equal energy dissipation criterion

The first hypothesis, given by Paulay and Priestley, consists in equalling the displacements of both elastic oscillator and inelastic one, whereas the second, equal energy method, equals the areas under the force-displacement paths. Then, exploiting some geometrical relations and knowing the definitions of the forces related to the mechanical behaviour of the structure in exam, the structure factor q is reached.

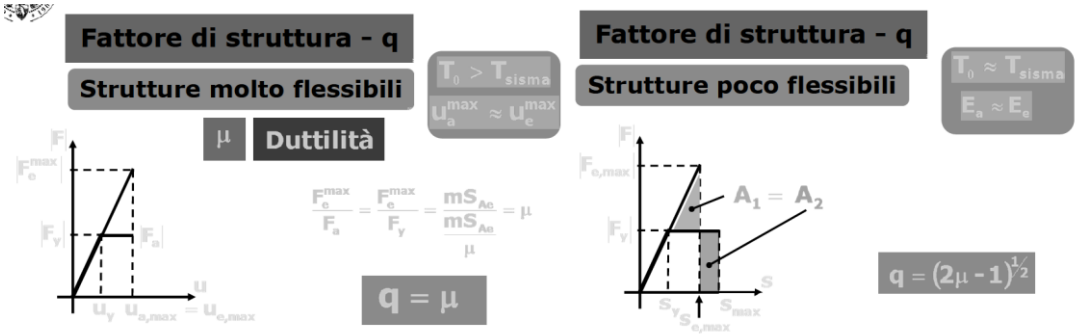


Figure 19-Evaluation of structural factor for italian codes

Finally, the elastic response spectrum can be scaled with the structure factor in order to obtain a lower force to apply to the structure, it means saving of money and a more controllable way to get the failure.

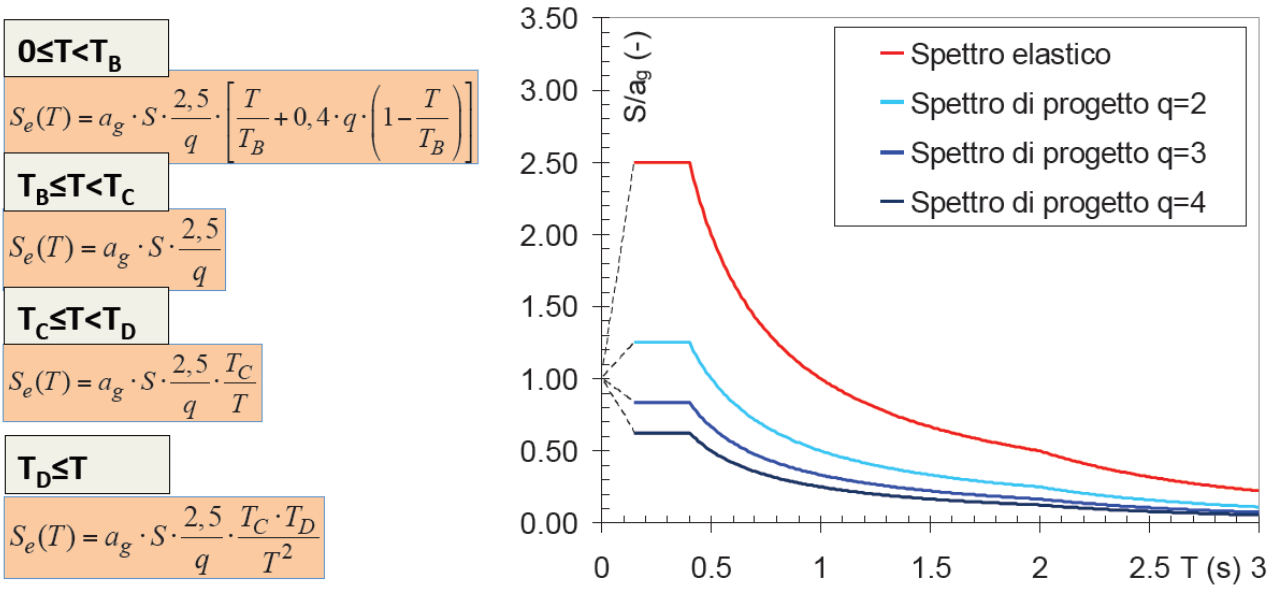


Figure 20-Elastic and design response spectrums

Actually, the codes already provide some easier procedure to determine the structure factor for constructions satisfying some requirements. These are:

- $\alpha_u/\alpha_1$: the ratio between the load multiplicator factor at the failure and at the formation of the first plastic hinge;
- $q_o$: base structure factor given by tables in the codes which depends on the ratio $\alpha_u/\alpha_1$;
- $K_R$: coefficient of regularity.

# Fattori di struttura

$$q = q_0 \cdot K_R$$

Figure 21-Simplificated procedure for structural factor evaluation for italian codes

**Tabella 7.4.I** – *Valori di* $q_0$

| Tipologia | $q_0$ | |
|---|---|---|
| | CD"B" | CD"A" |
| Strutture a telaio, a pareti accoppiate, miste | $3{,}0\alpha_u/\alpha_1$ | $4{,}5\ \alpha_u/\alpha_1$ |
| Strutture a pareti non accoppiate | 3,0 | $4{,}0\ \alpha_u/\alpha_1$ |
| Strutture deformabili torsionalmente | 2,0 | 3,0 |
| Strutture a pendolo inverso | 1,5 | 2,0 |

Figure 22-$q_o$ values related to the structural systems

Per strutture regolari in pianta, possono essere adottati i seguenti valori di $\alpha_u/\alpha_1$:

a) Strutture a telaio o miste equivalenti a telai

- strutture a telaio di un piano $\alpha_u/\alpha_1 = 1{,}1$
- strutture a telaio con più piani ed una sola campata $\alpha_u/\alpha_1 = 1{,}2$
- strutture a telaio con più piani e più campate $\alpha_u/\alpha_1 = 1{,}3$

b) Strutture a pareti o miste equivalenti a pareti

- strutture con solo due pareti non accoppiate per direzione orizzontale $\alpha_u/\alpha_1 = 1{,}0$
- altre strutture a pareti non accoppiate $\alpha_u/\alpha_1 = 1{,}1$
- strutture a pareti accoppiate o miste equivalenti a pareti $\alpha_u/\alpha_1 = 1{,}2$

Figure 23-$\alpha_u/\alpha_1$ values

# 3. SMATTERINGS OF BRIDGES FAILURES

Bridge failures can lead to injuries, loss of life, and property damage on a scale equal to plane crashes, terrorist attacks, and natural disasters. That is why bridge designers, engineers, construction workers, managers, and inspectors take their jobs so seriously. The best way for these professionals to prevent catastrophic accidents is to understand the factors that get bridges to failure.

It will be explained below, with the help of some bridges failure examples, the top reasons why bridges become seriously compromised or collapse.

## 3.1 A combination of issues

The top reason bridges fail is a mix of factors that, if they happened individually, would not cause a bridge to collapse. However, when they take place all at once, they result in devastating consequences. For example, severe winds may not be enough to cause a structure to come down. Although, when they hit a bridge that's structurally too rigid to withstand them, it leads to failure.

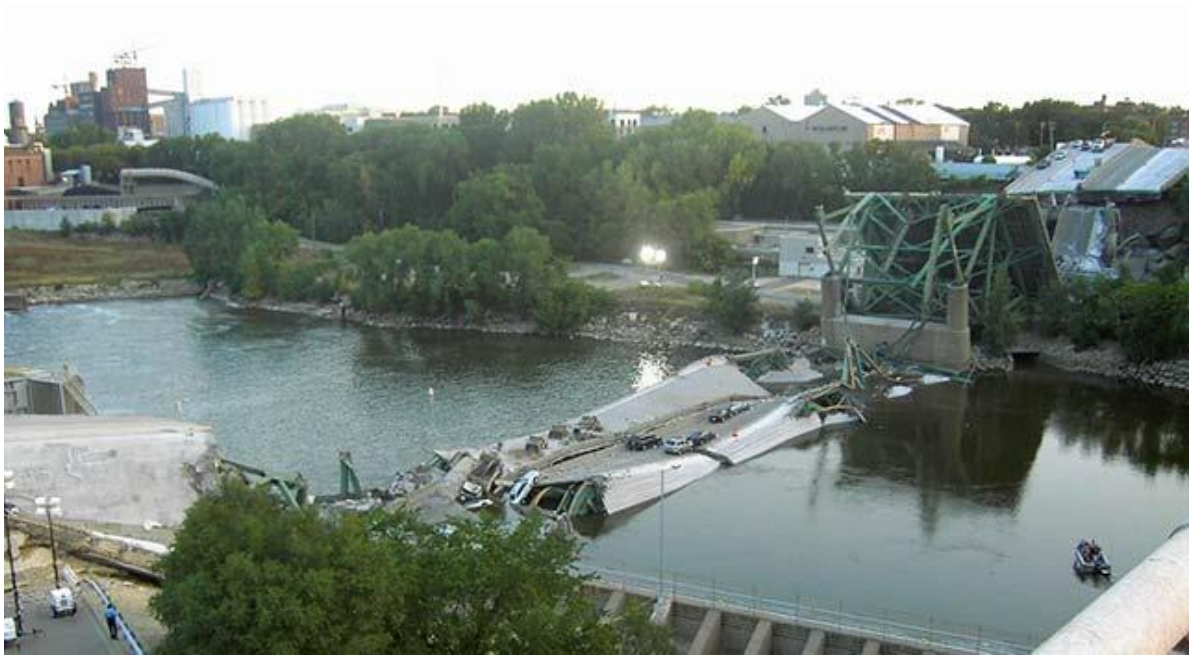

Figure 24-I-35W Mississippi River Bridge in Minneapolis

The I-35W Mississippi River Bridge in Minneapolis collapsed suddenly in August 2007. The official cause was attributed to gusset plates that were too thin and tore along a line of rivets.

The issue was that the plates had supported heavy traffic volume for 40 years. It took a secondary factor, the additional weight of construction equipment parked on the bridge at the time, to trigger the

failure. Another contributor was wear and tear on the gussets had not been identified prior to construction starting because bridge inspections had been missed.
So, while the gussets were identified as the root cause of this devastating collapse, it was really three separate factors coming together that led to disaster.

## 3.2 Infrastructure issues

According to the American Society of Civil Engineers, bridges in the United States earn a mediocre C+ rating for maintenance and safety. The group reports that one out of every nine bridges in the country is considered structurally deficient, and the average age of bridges in the U.S. is more than 42 years old. The age and condition of bridges is a contributing factor to many recent collapses.

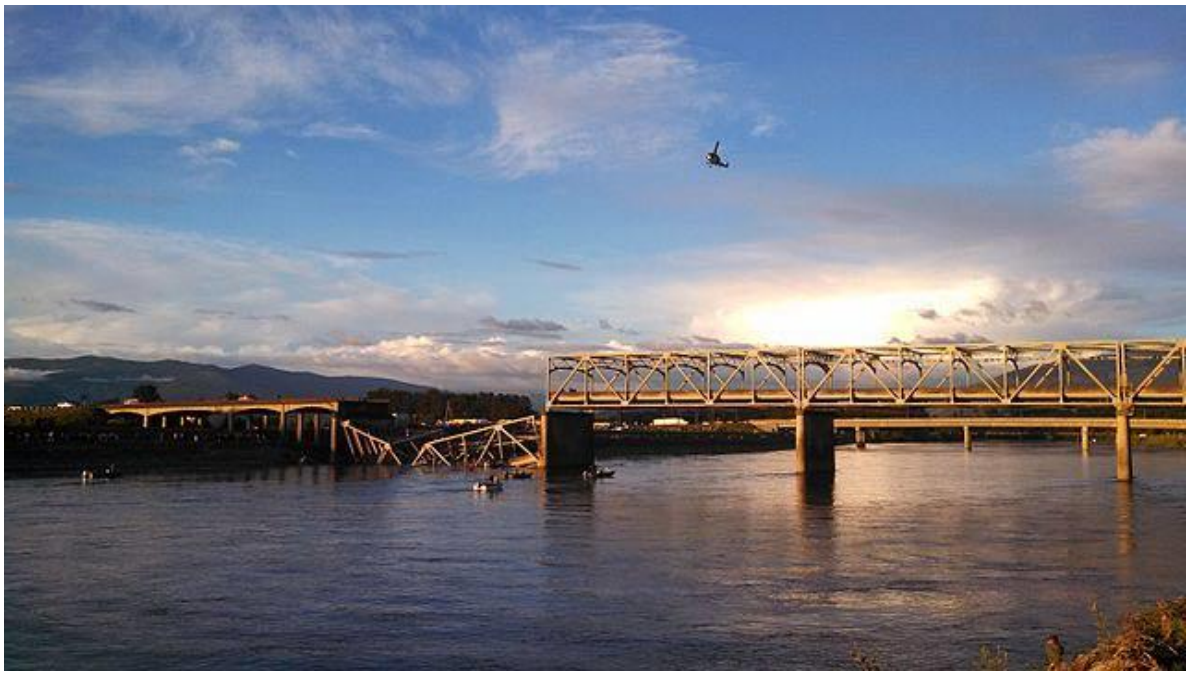

Figure 25-I-5 Skagit River Bridge in Mount Vernon

The collapse of the I-5 Skagit River Bridge (Mount Vernon, Washington) in 2013 is blamed on infrastructure-related problems. An oversized load crossing the bridge was the immediate cause of the incident. However, many weight restrictions had been placed on vehicles crossing the bridge because it had been declared functionally obsolete. This designation means it did not have the redundant structures and systems that would be required if the bridge were to be built today. The collapse could have been avoided if the antiquated bridge had been reinforced or replaced sooner, leveraging today's safer standards.

## 3.3 Floods

Today's changing climate and the extreme weather events associated with it are causing more flood-related damage to bridges. Most of this damage is not from water alone. During a flood, rivers pick up debris, such as trees and buildings, and push it forcefully against bridges, causing their foundations to wash away and structural elements to break apart.

Most collapses happen on bridges that were built a long time ago when designers could not imagine the kind of storms they would have to withstand today. It must plan structures and drainage systems that can hold up against today's storms and potentially more extreme weather events in the future.

Extreme rain in Louisiana in August 2016 caused significant flood-related damage to the Walsh Road and Stein Road bridges in Tangipahoa Parish, requiring them to be replaced. While damage to two relatively small local bridges may not seem like a big issue, closing them for more than six months caused significant economic impact to an area recovering from the storms. Better planning, including installing storm drainage systems or bridge reinforcements, could have avoided this hardship.

Figure 26- The Walsh Road and Stein Road bridges in Tangipahoa Parish

## 3.4 Unexpected events

Countless bridge incidents happen because of unanticipated structural or design-related issues. Nowadays, computer modelling and testing make it easier for engineers to see how different bridge designs hold up against a broad range and combination of unexpected conditions. Still, it is important

for them to build redundancies into structures to cover unknown possibilities in today's fast-changing world.

Figure 27- The Tsing Ma Bridge in Hong Kong

The Tsing Ma Bridge in Hong Kong is among the longest suspension bridges in the world. It is built on a site that experiences earthquakes, extreme winds, rough water, and typhoons. Prior to being completed in 1997, it underwent significant scale model, wind tunnel, and computer testing. This led to innovations that improved the design of this bridge and others that followed.

## 3.5 Accidents

Whether it is a truck hitting a support post, a train falling off the tracks or a boat colliding into a foundation, accidents are one of the leading reasons bridges are damaged or come down. Bridge engineers must plan for all types of incidents, including those caused by vehicles that exist today and ones like driverless cars, larger ocean tankers, and cruise ships, along with pilotless drones that could impact bridges in the near and distant future.

Back in 1982, a plane, the Air Florida one, took off from Washington National Airport and 30 seconds later, crashed into the 14th Street Bridge over the Potomac River. Seven vehicles traveling on the bridge were struck by the plane and drove into the freezing water. Four of the people in them perished. Amazingly, only a few hundred feet of guardrail and wall from the side of the bridge were torn away.

This is a testament to the strength and durability of the structure built near the centre of the nation's capital.

Figure 28-The 14th Street Bridge airplane accident in Washington DC

## 3.6 Construction incidents

Some bridges never make it to completion. They fail during construction. A lesson learned from these incidents is that it's just as important for designers and engineers to plan all aspects of bridge construction step by step, analysing the impact new phases will have on previous ones.

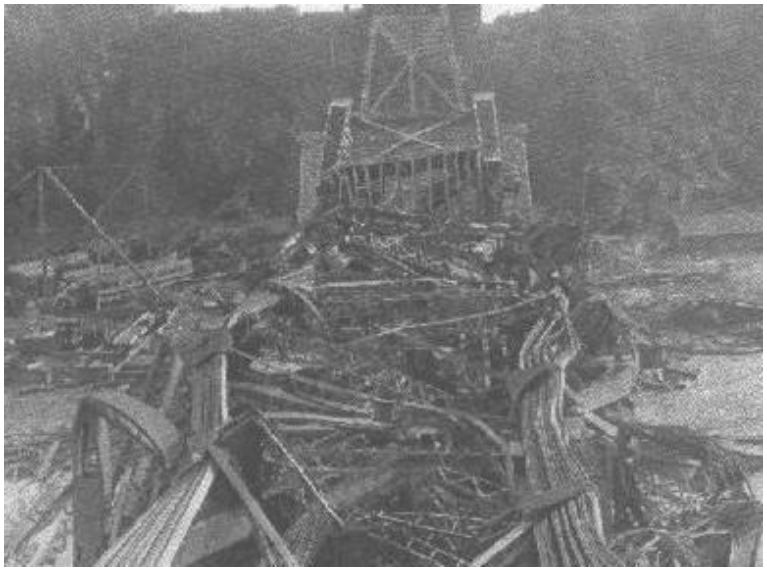

Figure 29-bridge failure happened during construction in Quebec City

Back in 1907, an epic bridge failure happened during construction in Quebec City. Designers were made aware that the bridge weighed eight million pounds more than estimated at a certain point in the construction process. However, they did not feel this was a significant enough issue to make adjustments. Soon after, an onsite engineer noticed the frame of the bridge was starting to bend. However, others did not take the observation seriously, claiming the beams were bent when they were delivered. Not long after, the structure came down, killing 75 workers. In the end, it was determined that the beams were not adequate to handle the additional eight-million-pound load.

## 3.7 Design flaws and manufacturing errors

While it is becoming less common than in the past, some bridges fail almost immediately after completion due to significant design errors or issues associated with materials used in the construction process. Frequent inspections throughout the construction process can provide a fresh view needed to identify problems and flaws. New types of lifts and equipment make it easier for inspectors to get to hard-to-reach areas of bridges.

Figure 30-Tacoma Narrows Bridge

The original Tacoma Narrows Bridge was built to cross the Puget sound in Washington state in 1940. Almost four months after opening to the public, it collapsed into the water.
A design flaw caused it to shake violently in the wind. This bridge, nicknamed “Galloping Gertie,” is still referenced in engineering textbooks as an example of how not to build bridges in extreme wind areas.

## 3.8 Fires

Fires used to be a much bigger contributor to bridge failures than they are today. More bridges used to be constructed of highly flammable wood. However, fires can still take down a bridge, especially when truck or tanker collisions or

Figure 31-The Liberty Bridge in Pittsburgh

construction incidents lead to extremely hot fires that can melt steel infrastructure components.

One step bridge designers can take to avoid super-heated conflagrations protecting utility infrastructure on bridges so gas, electrical and other utility lines do not cause or contribute to fires.

The 89-year-old Liberty Bridge in Pittsburgh was damaged significantly because of a construction-related fire in September 2016. A spark from a welding tool ignited a highly flammable plastic pipe and tarp. The fire burned so hot, it bent a critical 30-foot-long steel beam by six inches. The beam was designed to support 2.4 million pounds of pressure. Bracing and heat treatments were required to bring it back into structural alignment.

## 3.9 Earthquakes

Although rare, bridge collapses caused by earthquakes can be devastating. Swaying bridges or collapsed sections of them are often the iconic video and still images that people associate with these powerful natural events. Bridge engineers have found ways to build bridges that are lighter and add flexibility and rigidity in the right places that make it more likely to survive even the most violent quakes and aftershocks.

Figure 32-The Oakland Bay Bridge in San Francisco

It can be remembered the pictures of the section of the San Francisco Oakland Bay Bridge that fell down during the Loma Prieta earthquake in 1989. Fortunately, the devastating collapse cost only a single life. Significant improvements were made to the bridge after the incident, including replacing existing rivets with stronger, heat-treated ones and adding diagonal box beams that provide greater stability when the bridge sways side to side.

# 4. SEISMIC ISOLATION DEVICES

Nowadays, the developments on the seismic subject and the necessity to improve the seismic response of the structure in order to protect the life and to safe money for designing took out some innovative solutions like the isolation bearings. There are a lot of devices, each one depending on the function and requirements that has to satisfy. There exist two main categories of bearings:

- Elastomeric bearings

- Friction sliding bearings

## 4.1 Elastomeric bearings

The elastomeric bearings born with the aim of dissipating energy accepting high plastic deformations, by means of several hysteretic cycles. Among the various type of bearings of this family the most used are the reinforced elastomeric bearings. They consist of elastomeric material layers, with a thickness of about 5-20 mm, alternated with steel plates of 2-3 mm thick, jointed each other with the vulcanization process. The plates are shorter than elastomeric layer in order to be included inside for protecting the steel from the corrosion phenomenon and have the function of confining the elastomer that limits the vertical deformability, containing the deformation of the elastomeric bearing within about 1-3 mm in serviceability condition, enhancing the vertical bearing capacity, without influencing sensibly the shear deformability in the horizontal direction. Before this reinforced solution there was the non-reinforced one, but it showed a very high vertical deformability and the "rocking" effect took place, rotational motion around the horizontal axe.
Another important characteristic is the kind of rubber employed for the bearing, the generic chemical composition is given by the hydrocarbon $(C_5H_8)_n$. Thus, depending on this latter one two kinds of isolator can be distinguished:

- Natural rubber isolator: composed of isoprene ($C_5H_8$) layers in sequence to set up a highly elastic chain

- Synthetic rubber isolator: composed of neoprene $(C_5H_8Cl)_n$ which has many advantages like fireproof capacity, gasproof capacity and less aging tendency

On the other hand, independently to the kind of rubber, the rubber damping value acquires importance. On the basis of this parameter there can be identified:

- Low damping rubber bearings (LDRB)

- High damping rubber bearings (HDRB)

### 4.1.1 Low damping rubber bearings (LDRB)

Ease of producing and modelling, the have mechanical behaviour independent to oscillation frequency and slightly sensible to the temperature. They may be made of either natural or synthetic rubber. The only disadvantages are represented by the low damping value and high horizontal deformations for serviceability horizontal loads like wind action.

Figure 33-Low damping rubber bearing

### 4.1.2 Lead rubber bearing (LRB)

The lead rubber bearings, developed in the 1978 in New Zeland by Robinson [Robinson and Tucker, 1977], are very similar to the reinforced ones, with the only difference of having at least a lead core in order to increase the dissipative capacity of the isolator through the plasticization of the lead cores. The lead is capable to deform in the plastic field, dissipating energy without damaging itself in irreversible way. Indeed, after a cycle recrystallizes, recovering the initial conditions.

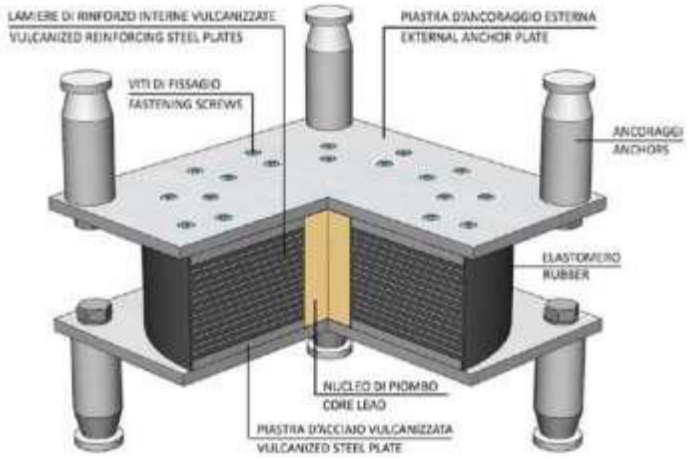


Figure 34-Lead rubber bearing scheme

The structures isolated with these systems have borne, with satisfactory results, also the strong earthquakes of Northridge 1994 and Kobe 1995. The behaviour of the systems with LRB bearings shows:

- Higher initial rigidity than other rubber isolators thanks to the lead core, presenting neglectable deformations for non-relevant actions.

- Higher damping capacity (about 30%)

- With same performance they are cheaper than the HDRB

The force-displacement behaviour is bilinear and a function of the rubber-lead combination, so it comes out from the elastic behaviour of the rubber and elastic-plastic one of the lead core. The equivalent viscous damping value, related to hysteretic cycles of the device, stays within 15-35%.

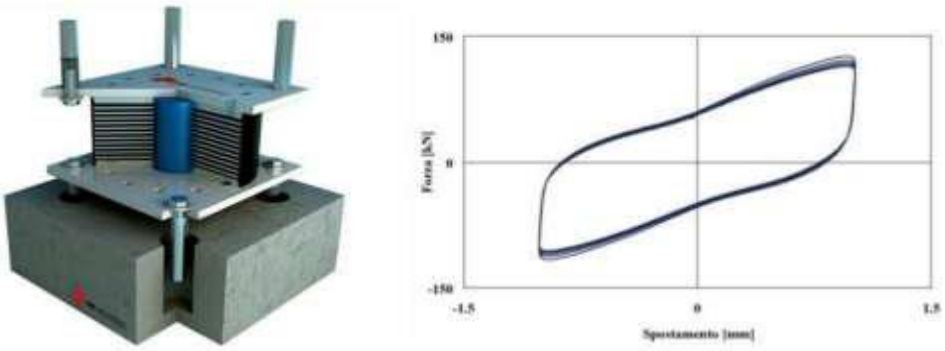


Figure 35-Force-displacement behaviour

### 4.1.3 High damping rubber bearings (HDRB)

As previous said, this solution differences from LDRB one only for the rubber composition. They were developed by Kelly in the 1985 at University of Berkeley (California).
Thanks to special additives added in the production phase, it has an increasement, from 1-2% to 10-20%, of the damping critical ratio. In particular, these additives may be carbon black and silicon. The anchoring of the bearing to the structure cannot be performed by the friction mechanism, therefore some special mechanical systems are needed (fig. 36).
Thus, the HRDB alone, performs a complete and efficient system of isolation because of both filters and dissipative capacity. Moreover, it has a good re-centring capacity too.
Looking at the force-displacement behaviour, it can be seen a higher initial rigidity, allowing the little displacements against serviceability loads such as wind without influencing the dissipative energy capacity during an earthquake (fig. 37).

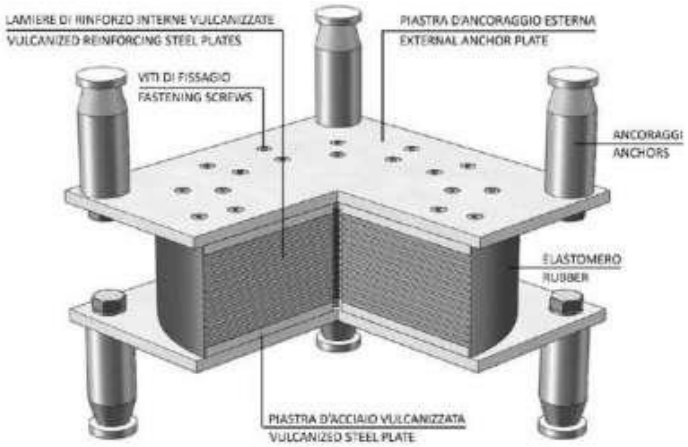


Figure 36-High damping rubber bearing scheme

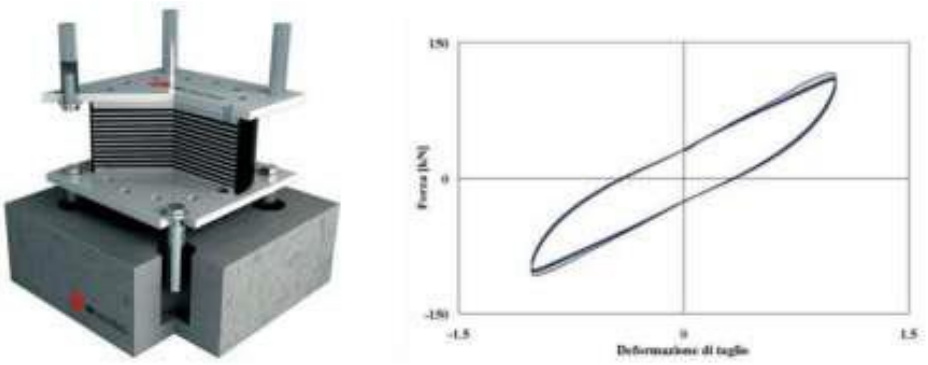

Figure 37-High damping rubber bearing force-displacement behaviour

Generally, it shows a nonlinear behaviour with high initial rigidity and damping value for shear deformations up to 20%. Furthermore, the behaviour is influenced by many factors resumed as follows:

- Rigidity and damping value dependencies varying with shear deformation level
- Variation of the hysteretic cycle shape depending on the shear deformation level
- Dependency on the strain history, it means the velocity with which the cycle is performed
- Dependency on the temperature excursion
- Softening effect on the cycles next to the first one (Scaragging effect)

## 4.2 Friction sliding bearings

### 4.2.1 Flat sliding bearings: Sliders

They are multidirectional sliding devices with low friction, generally composed of two circular or squared shaped plates which slide over each other. The materials employed, steel and Teflon usually, are chosen in order to develop a low friction. The dynamic friction coefficient goes from 5% to 20% and it reduces up to about 1-2%, in case of lubricated surfaces. In this latter case, as the horizontal forces explicated are negligible, the sliding devices are supported with elements able to improve the stiffness and to perform re-centring and dissipative features. For designing and modelling ease, in case of lubricated surfaces, the dissipation of energy is neglected, and the devices are used only for carrying vertical loads leaving the horizontal displacements free to move.

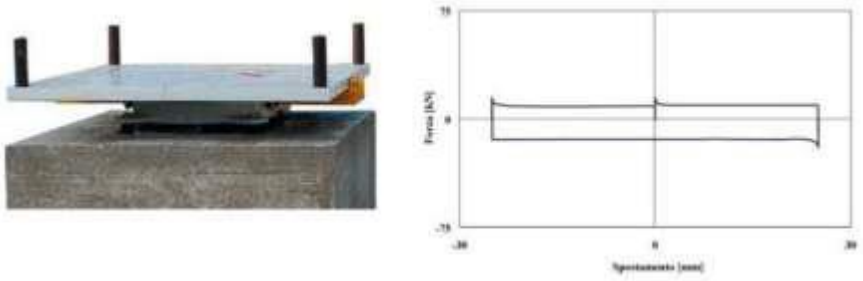

Figure 38-Flat sliding bearing and relative force-displacement behaviour

### 4.2.2 Concave sliding bearings: Friction pendulum systems (FPS)

In the next paragraphs there will be a more detailed study on the FPS characteristics, while here is given a brief introduction on its working principles. The FPS systems allow the relative displacements between the superstructure and the substructure by means of one or more concave sliding surfaces with an articulation in the middle. These devices are characterized from two principal features:

- The period of vibration of the structure is determined from the radius of curvature;
- The period of vibration of the structure is independent from mass of the superstructure.

The system works explicating a friction and a re-centring force. The first one turns out to be from the relative sliding of the surfaces thanks to the articulation, instead of the second one arising because of the concave surface, indeed there is a continuous exchange of kinetic energy and potential energy during the motion that try to take the oscillator mass in its initial stable position.

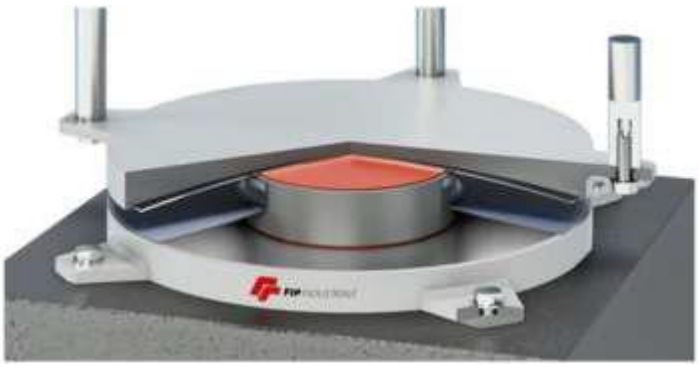

Figure 39-Single concave surface sliding bearing

# 5. PROTECTIVE STRATEGIES WITH VIBRATION CONTROL TECHNIQUES

For several decades, until 1970, the traditional methods of seismic design were based on the elastic approach without considering the ductility level related to a reduced capacity of energy dissipation (Priestley, Seible, Calvi, 1996) [8].
Nowadays is well known, how the ductility, in other words the capacity of the structural elements to develop large deformation in the plastic field, is decisive for a good seismic design approach.
A design criterion focused on the bearing capacity enhancing takes to two possible choices:

- Increasing of the structural bearing capacity, designing more expensive structure capable to take larger accelerations in the elastic field

- Increasing of the structural global ductility by means of "Capacity Design Approach", which is devoted for developing of plastic mechanisms to dissipate more energy, avoiding undesired mechanisms of failure that do not allow a good ductile behaviour of the whole structure.

Since the methods used for the protection of structures follow a common idea, this one may be renamed as "control of vibrations", because of the aim of controlling the vibrations due to wind and earthquakes by means of some devices.
The control systems can be classified under two big families:

- Open ring control systems

- Closed ring control systems

An open ring control system is a system wherein, the controlling action is independent from the output response (as shown in the figure 40).


Figure 40-Open ring control system

In this case the controller filters the seismic input before arriving to the main structure. For base isolated system, it realizes a sort of open ring passive control system where the seismic signal is filtered by the isolation level that which behaves as controller.
Whereas, in a closed ring control system the control action depends on the output response and creates a cycle (as shown in the figure 41), wherein the control action changes at every cycle.

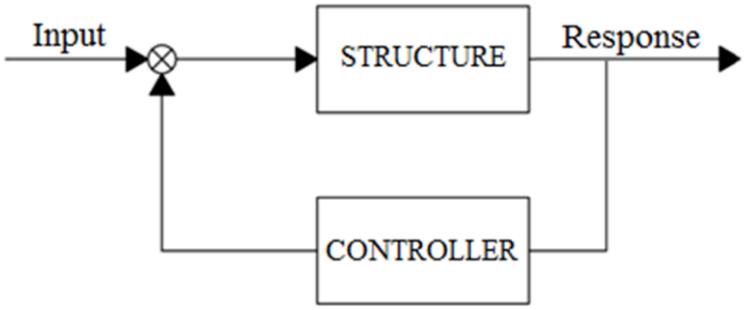


Figure 41-Closed ring control system

From the application point of view, it is possible to distinguish four control modes:

- Passive control
- Active control
- Semi-active control
- Hybrid control

## 5.1 Passive control

The passive control is the simplest and very reliable method. This technique provides the addition of PED (passive energy dissipation) devices whose change the dynamic behaviour of the structure without neither an external energy source and generating or generating external forces. The passive control system may provide sensors to measure the excitation amplitude.

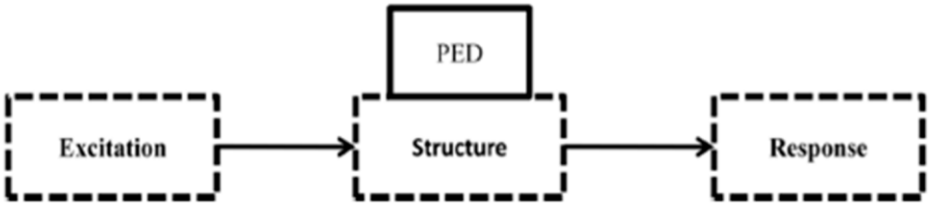


Figure 42-Passive control scheme

The main passive control techniques are:

- Seismic Isolation (fig. 43b): a low horizontal rigidity element is placed between the structure and the ground to decouple the motion of the whole structure

- Additional energy dissipation (fig. 43c): damping devices are added capable to dissipate energy by means of hysteretic, frictional and viscous behaviour.

- Tuned mass damper (TMD) (fig. 43d): additional mass counteracting in opposite phase the motion of the structure to reduce the displacements.

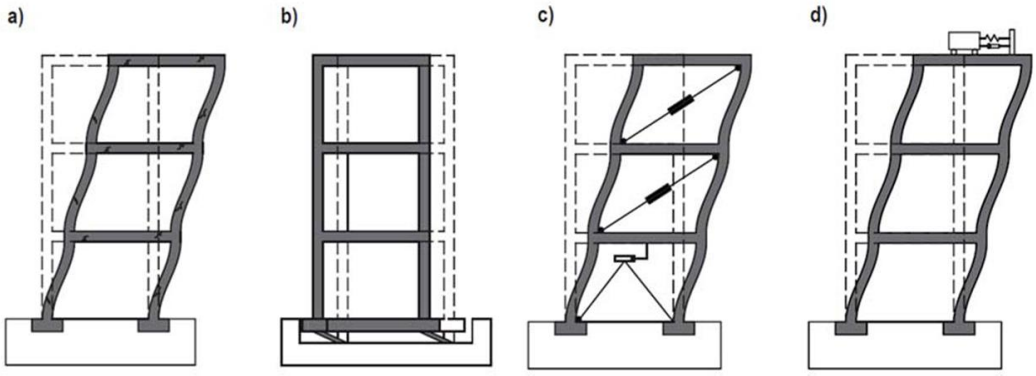


Figure 43- a) Non-protected structure; b) seismic isolation; c) additional energy dissipation; d) TMD (Foti D. & Mongelli M., 2011)

## 5.2 Active control

The active control system consists of force delivery devices, real-time data processors and sensors. The control forces are provided depending on the input signal and the structural system response recorded by sensors. Real-time data computers process the information and evaluate the needed force

to counteract the measured vibration amplitudes. The control forces are generated by electro-hydraulic actuators which need a big amount of energy from an external source. External actuators supply the necessary forces to mitigate the vibration of the structure (fig. 44).

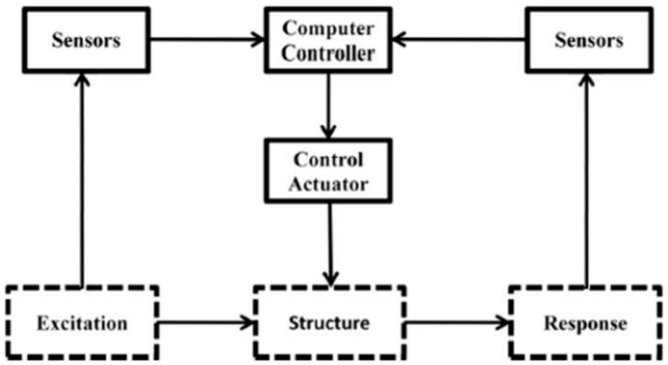


Figure 44- Active control system (Rahman, Ong, Chong, Julai, & Khoo, 2015)

## 5.3 Semi-active control

The semi-active control system combines the advantages of both active and passive controls (fig). Compared to the passive control, where the control forces are developed from the motion of the structure itself, suitable adjustable mechanical devices are used to supply these ones. Therefore, semi-active devices are often called “Controllable passive devices”. Thus, the scheme of a semi-active control system is like the one of the active control, except the external control forces. Semi-active control method seems to be the most attractive nowadays because offers reliability of passive and adaptability of active devices.

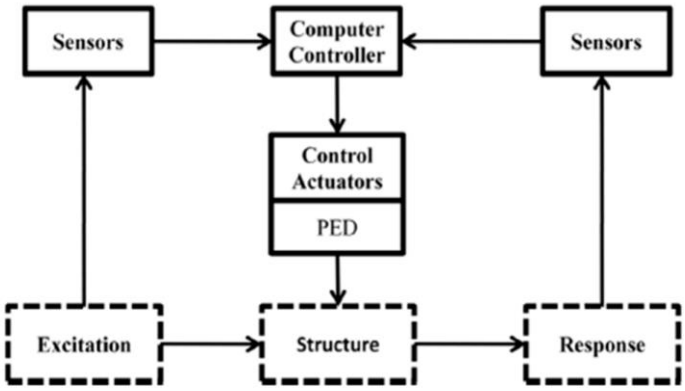


Figure 45-Semi-active control scheme (Rahman, Ong, Chong, Julai, & Khoo, 2015)

## 5.4 Hybrid control

Finally, the hybrid control consists of applying an active control system to a passive one (fig). Moreover, this system needs less energy to achieve the same performance of a structure equipped with only active control devices.

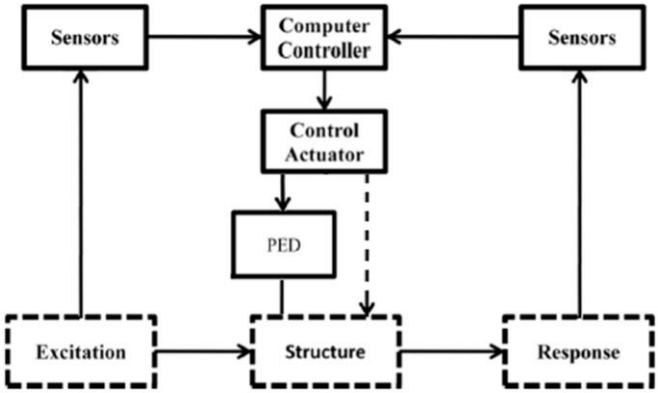


Figure 46-Hybrid control scheme

The following figure (fig. 47) shows a resume of vibration control strategies.

| Vibration Control method | Scope | Maturity degree |
|---|---|---|
| Seismic isolation | Medium height buildings | • Mature technique<br>• Many experimental results and data<br>• Many applications over the world |
| | Bridges and civil infrastructures | |
| | Instrumentation and devices | |
| Additional energy dissipation | Medium height/tall buildings | • Mature technique<br>• Many experimental results and data<br>• Many applications over the world |
| | Towers, poles, chimneys | |
| | Long span bridges and civil infrastructures | |
| Other types of passive control | Medium height/tall buildings | • Relatively mature technique<br>• Many experimental results and data<br>• Many applications over the world |
| | Towers, poles, chimneys | |
| | Long span bridges and civil infrastructures | |
| Active, semi-active and hybrid control | Tall buildings | • Mature technique<br>• Many theoretic results<br>• Some applications over the world |
| | Towers, poles, chimneys | |
| | Long span bridges and civil infrastructures | |

Figure 47-Vibration control strategies

# 6. MECHANICS OF FRICTION SLIDING DEVICES

Friction is the force resisting the relative motion of solid surfaces, fluid layers, and material elements sliding over each other. This paragraph is focused on the interpretation of the friction phenomenon from the macroscopic point of view.
The value of the friction force, in its more general expression, at the interface of sliding is given by:

$$F_f = \mu * N$$

Where $\mu$ is friction coefficient and N is the normal action to the interface surface. The friction force manifested between two surfaces at rest to each other is renamed static friction force whereas, the one explicated between two surfaces in motion over each other is called dynamic friction force.
The classical friction law used in many cases of engineering interest is the Coulomb's one which describes the behaviour assuming constant friction during the motion, so it is useless for sliding devices because it is already explained, in the previous paragraphs, that the friction coefficient is strongly dependent on sliding relative velocity and compressive stress (Constantinou et al.).
For reasons of interest, it may be useful to show the mechanisms governing the friction phenomenon at the macroscopic scale, in order to have a better idea on this topic. The major efforts in this way were performed by Bowden and Tabor (1950, 1964, 1973).

## 6.1 Adherence

When two solid bodies come into contact with each other, develop atomic bonds through the contact interfaces. Such contact regions are called junctions, and the sum of everyone consists on the effective area of contact which results sensitively smaller than the apparent area. The adherence is dominating for those cleaned interfaces sliding over each other.

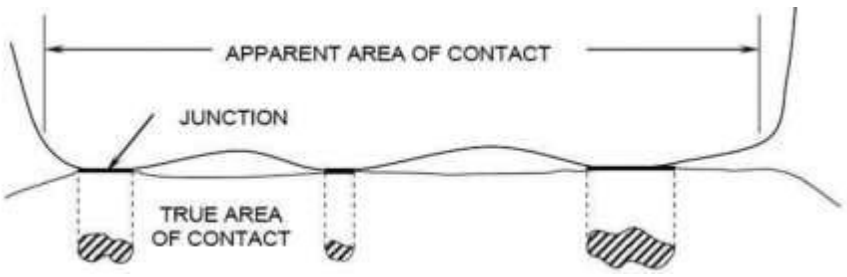


Figure 48-friction areas of contact

The junctions are characterized from interface forces representing, indeed, the adherence given by the interaction carbon-steel which makes the interfacial bonds between the cleaned surface and the Teflon.
Therefore, the friction force turns out to be the product of the effective contact area $A_r$ and the shear strength of the junctions:

$$F_a = s \cdot A_r$$

## 6.2 Plowing

Every surface has some asperities which suffer both elastic and plastic deformations due to the stresses involved by means of contact. The Plowing contribution, to the friction, is because of the dissipation of energy occurring during the plasticization of the asperities. This phenomenon may be quickly understood by considering a hard-spherical asperity over a soft-plane surface. If an axial action acts on the asperity, the same sticks to the underlying surface making contact areas, the junctions. Then, by inducing a tangential action, the asperity moves horizontally, dragging with itself a part of the underlying softer material digging a groove along the trajectory followed. As consequence, the plowing arises from this effect of dragging.

## 6.3 Viscoelastic effect

The polymers, for instance the Teflon, show a viscoelastic behaviour depending on the viscosity of the material which in turn depends on the temperature and velocity of deformation. In other words, the viscoelastic materials present both elastic and viscous characteristics. In fact, due to the viscous component, they perform additional dissipation of energy.

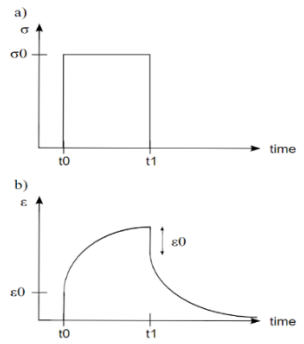


Figure 49-a) stress-time law path, b) strain-time viscoelastic law path

## 6.4 Stick and slip

The stick-slip phenomenon consists in blocking and sliding phases in sequence. It occurs in lubricated systems because of:

- The dynamic friction coefficient is lower than the static one

- The system can store elastic energy

The system stores elastic energy in the static phase for releasing it in the dynamic one due to the forces acting on. This determines an oscillation in the force and a motion with snaps.

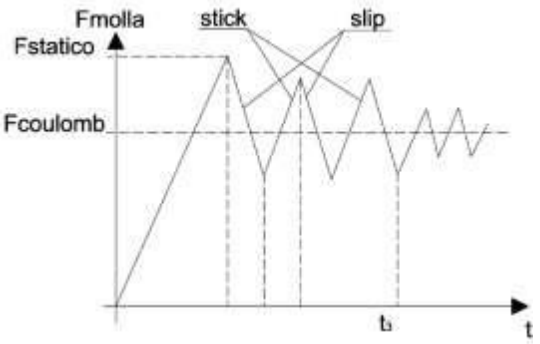


Figure 50-Stick-slip phenomenon

# 7. EXPERIMENTAL ANALYSIS ON CONCAVE SLIDING BEARINGS

For a better study of the seismic behaviour of friction pendulum systems is necessary to show the friction phenomenon property with reference to the various phases of the motion. With this aim is useful to distinguish, as already said in the previous paragraph, between dynamic friction coefficient and static friction coefficient. A very large experimental campaign of investigation allowed to extrapolate some analytical expressions which describe the dependency, of the friction coefficient, on the relative sliding velocity between the surfaces, beside the temperature and compressive apparent stress.

## 7.1 Dependency on the relative sliding velocity and compressive apparent stress

The figure below shows as the dynamic friction coefficient is characterized from a low value, immediately, after starting of the sliding, $f_{min}$, and then from an increasing together with the relative sliding velocity. Moreover, if the normal load increases, the diminishing of the friction coefficient turns out to be from (Mokha et al,1990), until a constant value for a limit value of the load. The decreasing rate is practically constant, doubling the compressive stress at the contact (from 9.36 to 18.7 MPa) a variation of the friction coefficient (from 25% at -10°C to 33.4% at 50°C) is performed [3].

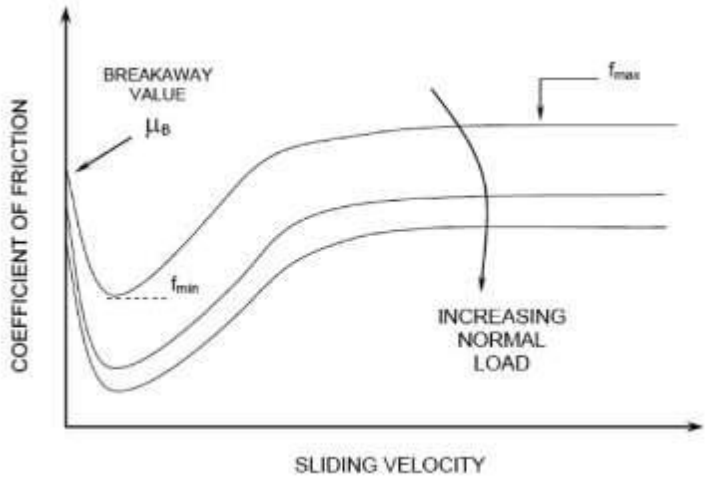


Figure 51-Friction dependency on the relative sliding velocity and compressive apparent stress

The high value of static friction coefficient, $\mu_b$, is due to the adherence phenomenon which explicates junctions characterized by high interfaces forces because of the chemical bonds.
At the beginning of the sliding, a crystalline oriented thin film of Teflon, few hundreds of Angstroms thick, is placed on the in-oxidable steel surface reducing the friction coefficient value from $\mu_b$ to $f_{min}$, this is because of the low shear strength that such material has. Increasing the relative sliding velocity, the friction coefficient increases too, until reaching its peak value equal to $f_{max}$, which can reach 5-6 times the $f_{min}$ value. In particular, the gap between the minimum and the maximum values of the dynamic friction coefficient ($D = \mu_{max} - \mu_{min}$) is higher when the compressive stress at contact is lower, assuming values from about 12% at 9.36 MPa to 7% at 28.1 MPa [4]. Otherwise, the temperature has a low influence on D. Generally, for a fixed value of the apparent compressive stress, the friction coefficient depends on the relative sliding velocity, as described by (Mokha, Costantinou, Reihorn, 1990) [5], [3] in the following expression:

$$\mu = f_{max} - (f_{max} - f_{min}) \cdot e^{-\alpha \cdot v} \tag{7.1}$$

Where $f_{max}$ is the friction coefficient of the device at high velocities (200-800 mm/s) , $f_{min}$ is the friction coefficient of the device at low velocities, v is the relative sliding velocity, α is the reverse of the characteristic relative sliding velocity value, which presents variable values of 20-30 mm/s for in-oxidable steel-Teflon devices, and has the task to control the friction coefficient variations from the minimum to the maximum values.
The curves showed in the figure below are based on the previous expression, which describes, adequately, the experimental results and show how the parameter α influences the behaviour of the non-dimensional friction coefficient with respect to the maximum one for two different values of $f_{max}/f_{min}$ (2.5 and 5). It is noteworthy how, for a relative sliding velocity higher than 150 mm/s, is sufficient to obtain the maximum value of the friction coefficient, for all that materials with Teflon based on, at normal temperature.
Finally, it can be noted that:

- The friction coefficient increases rapidly with the velocity up to such value beyond which stays constant, so this value is 150 mm/s and it is independent from both environmental temperature and compressive stress on the device;

- The friction coefficient for steel-Teflon interface devices decreases with the increasing of compressive stress on the sliding surface. The reduction rate depends on the velocity and air

temperature, it may have a maximum variation of 30% for a variation of ± 50% of the compressive stress at contact (for T=20°C, p=18.7 MPa, v≥150 mm/s), independently from the state of lubrication of the interfaces;

- The gap between the minimum and the maximum values of the friction coefficient, increases with the decreasing of the compressive stress.

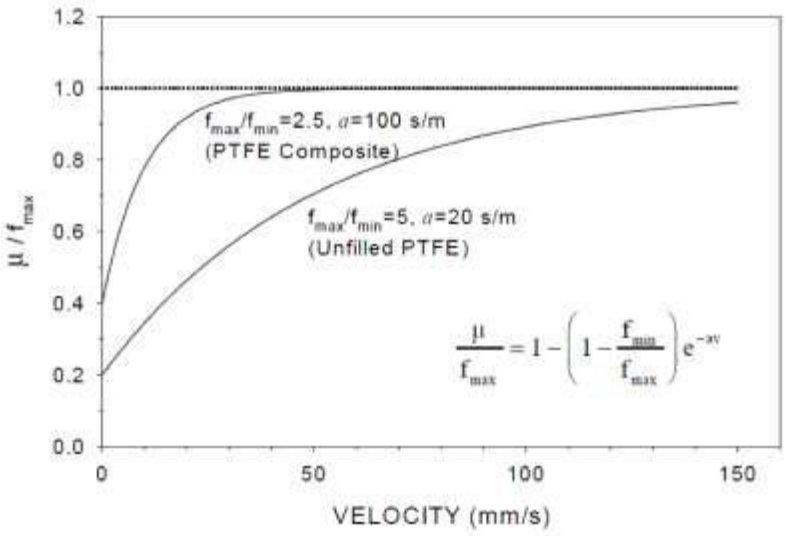


Figure 52-Effect of parameter α on the friction coefficient variation with the velocity

## 7.2 Dependency on temperature

The effects of temperature on friction sliding devices may be critical, especially as regards the static friction coefficient, $\mu_b$, and the minimum dynamic friction coefficient at low velocity, $f_{min}$.
In the figure below is reported the behaviour of the friction coefficient for fixed values of temperature. It shows the strong effect on the coefficients, $\mu_b$ and $f_{min}$, and, whereas, the limited one on $f_{max}$.

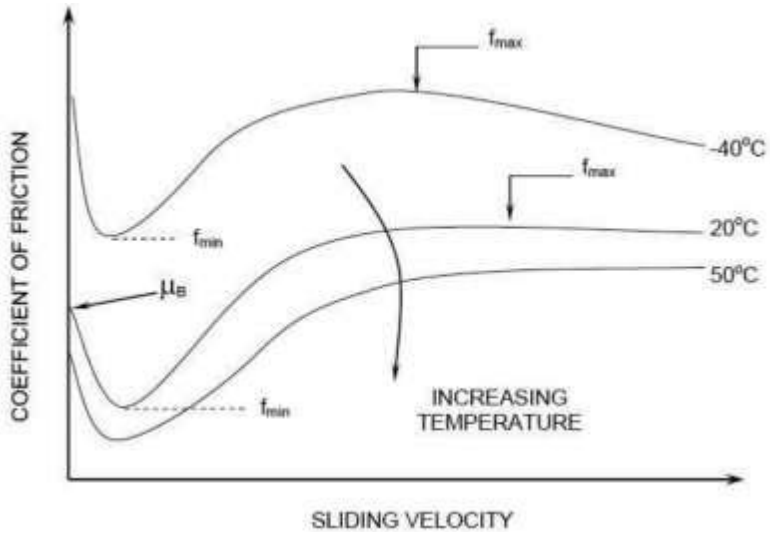


Figure 53-Friction dependency on the relative sliding velocity and temperature

Even in this case, it can be noted that:

- The friction coefficient at starting of the motion is, practically, the same of the low velocity one.

- The effects of temperature on composite Teflon devices are smaller, generally, than the ones on unfilled Teflon devices.

- The friction coefficient decreases with the increasing of environmental temperature, the reduction rate is higher if it passes from low temperatures to medium ones, rather than from medium to high ones. Furthermore, depends on the sliding velocity, whereas is independent from compressive stress at contact. The velocity for the seismic application has a reduction rate on the order of 0.15-0.3%/°C.

This latter consideration is related to the effect of warming, so the heat flow due to friction is proportional to the same one, the mean compressive stress and the sliding velocity, although, at high velocity (500 mm/s), is few hundred times higher than the one produced at low velocity (<1 mm/s). This heat flow tends to compensate the effects that the low temperatures have on the viscoelastic properties of Teflon, in this way a temperature variation from 20°C to -40°C carries out an increasing of the coefficient $f_{max}$, only of 50%.
The values reported by Constantinou are in line with the Campbell's ones (1991).

## 7.3 Effects of load permanency and covered distance

Since Teflon is a material having viscoelastic properties, it would expect that the effects of load permanency are greater and greater as much as the time spent under the acting loads is longer [Bowden and Taboor, 1964]. In Contrast, from the experiments performed (Mokha et al, 1991) [5], the static friction coefficient turns out to be the same for a load acting for both 0.5 hours and 594 days. More other tests have been performed, showing the oscillation cannot be attributed to the load permanency. On the other hand, tests performed on samples, previously subjected to other test cycles, have shown a static friction coefficient straightforwardly lower after a first load cycle, testifying the proof that a thin film of Teflon lays down on the steel surface after a first cycle.

Therefore, the experimental results (Constantinou et al., Mokha et al.) [6], [5] and [3] reveal that, when the natural variability of the friction properties obtained from different samples or test on the same specimen, considering the probable measurement errors, the static friction coefficient for steel-Teflon surfaces is not affected from the load permanency.

Generally, the dynamic friction coefficient at high velocity, $f_{max}$, decreases with the increasing of the covered distance, passing from an initial value of 12.5% to 10%, after 40 m too; whereas, reaching the threshold of 300 metres, shows an increasing again. As concern the dynamic friction coefficient at low velocity, it presents oscillation in the range 0-40 m.

It can be observed that the friction coefficient tends to decrease during high velocity load cycles due to the viscoelastic properties of Teflon, such reduction consists in about 25-30%.

## 7.4 Effects of axial load variations

The FPS devices born as unilateral vertical supports, working only in compression. This has to be taken into account in designing phase because, if tensile forces would act on the device, they could suffer damages at the interfaces and there would be also the possibility of the articulation coming out from its housing track. Besides, the compressive state is a fundamental requirement for using the linear analysis approach. While the period T depends only on the radius of curvature of the hemi-spherical surface on which the sliding motion is occurring, the equivalent period $T_{eff}$, characterized by the equivalent stiffness, and the horizontal force F performed by the isolated system, are proportional to the axial load N acting at the level of the device. In other words, $T_{eff}$ and N are subjected to the continuous variations of the load N which entail some irregularities in the force-displacement relation of the isolators.

# 8. ISOLATED SYSTEMS WITH FPS

This seismic isolation devices placed between the basement and the structure in the buildings, or between piles and deck in case of bridges, represents one of the solutions with which it is possible to grant the protection of the structure, concentrating the deformations on the devices, having few structural damages or not at all depending on the requirements and the approach of designing. This occurs because of the capacity of the sliding bearings to change the fundamental frequency, or equally the fundamental period, of the structure moving it far from the principal contents of frequency of the earthquake. In other words, thanks to these devices, it obtains a reduction of the forces transmitted to the structure, by imposing a ground acceleration given, obviously, with the earthquake, with respect to a not isolated structure. The efficiency of this technique grows when the maximum ground acceleration expected at the site is higher. Moreover, on the economic side, it is a better solution because permits the structure to stay in the elastic field or to have a small damage, meaning a reduced ductility of the structure, absorbing the displacement demand in presence of earthquake, it means the devices have to be replaced, after a strong earthquake event, instead restoring the structure and it is a more cheaper way.

Among the more recent isolator devices there are the friction pendulum system devices, which, using the physics law of the pendulum, lengthen the period of the structure (Zayas et al. 1990), (Mokha et al. 1991). The real advantage of the friction pendulum devices consists on the structural frequency which becomes independent from the mass of the structure.

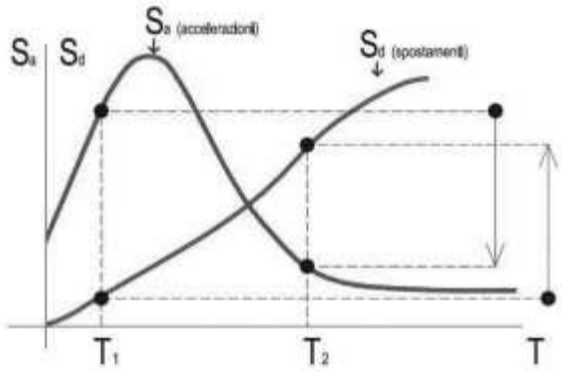


Figure 54-Shifting of isolated structure period

On the mechanical point of view, as showed in the figure 55, with reference to the single sliding concave devices, the decoupling of the isolated structure motion is given thanks to the relative sliding between the substructure and the superstructure through the hemispherical surface (Element A), in-built with the superstructure, and the articulation (Element B), linked to the substructure.

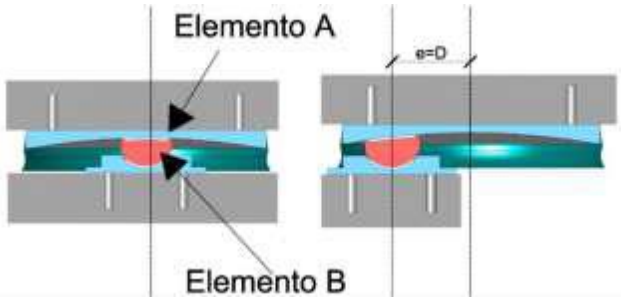


Figure 55-Single hemispherical concave device

It can be possible to use two equal hemispherical surfaces in-built with both the upper and lower sides of the structure, once again with an articulation placed in the middle making a double sliding surface.

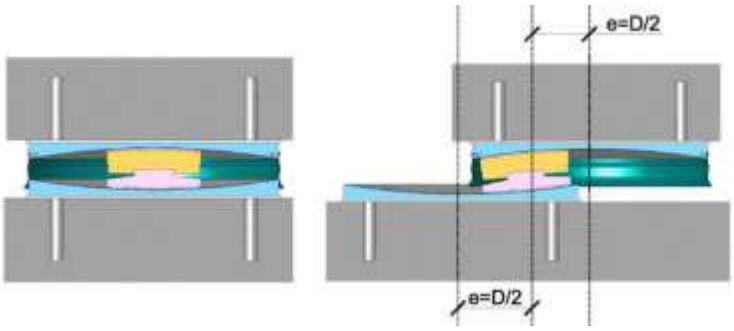


Figure 56- Single hemispherical concave device

In this last case it can be adopted, instead of a single sliding surface device with a certain radius of curvature, a double sliding surface device with a half radius of curvature of the first one.
The behaviour of the friction pendulum systems is ruled by the characterized of the interface among the elements with they are composed and paying specific attention to the radius of curvature of the sliding concave surfaces and the static and dynamic friction coefficients of the same ones. Indeed, from these lasts turn out to be the fundamental properties of the sliding devices: the capacity of dissipating energy through the not conservative force performed by the friction mechanism and the restoring force for the re-centring of the structure given by means of gravitational action and the curved geometry (radius of curvature) of the device. In detail, the first one is a force opposed to the

inertial forces acting on the structure by means of imposing accelerations to its mass due to the ground motion in presence of earthquakes, whereas, the second one is a force needed to restore the initial configuration of the device.

The current friction pendulum devices are obtained coupling a metallic surface composed with in oxidable or chromed steel and a plastic material such as Teflon not-lubricated or its composites, so with this solution it can be reached a friction coefficient from 0.03 to 0.12 and it was demonstrated with the following studies, over the years, by (Constantinou et al. 1987), (Mokha et al.1990a), (Mokha et al.1990b), (Mokha et al.1993), whose explained this phenomenon cannot be described with the Coulomb's law because the macroscopic behaviour is influenced by some physical quantities such as relative sliding velocity, compressive stress exchanged between the two surfaces, and temperature. In addition, the dynamic friction coefficient depends also on the number of cycles performed between the two sliding surfaces on contact, due to the degrading of the same surfaces (Hwang et al.1990).

## 8.1 Dynamic behaviour of pendulum system

The equations of motion are described by imposing both vertical and horizontal equilibrium of the pendulum system, as shown in the figure below:

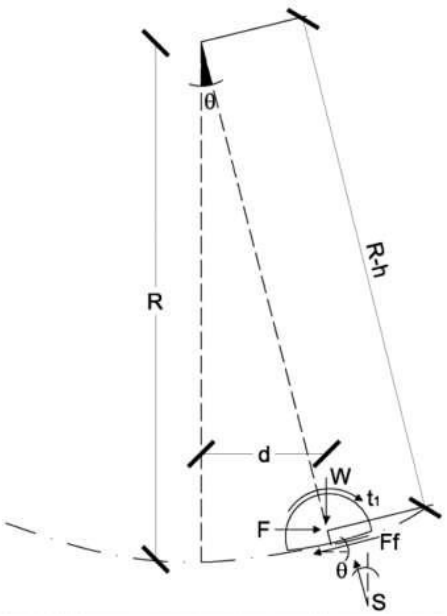


Figure 57-Pendulum scheme and acting forces

Where the forces acting on the slider are:

- The gravitational load (W=Mg) acting on the slider;
- The mass of the superstructure M;

- The lateral force F, acting on the slider;
- The friction force $F_f$, acting along the tangential direction of the sliding surface;
- The reaction S, acting normally to the concave sliding surface.

Considering the drawing above the equation of motion can be finally written:

$$W - S \cdot cos(\theta) + F_f \cdot sin(\theta) = 0 \tag{8.1}$$

$$F + S \cdot sin(\theta) - F_f \cdot cos(\theta) = 0 \tag{8.2}$$

by means of geometrical considerations, the spherical articulation displacement of the sliding surface can be written as:

$$d = R \cdot sin(\theta) \tag{8.3}$$

where R is the effective radius of curvature, evaluated as the distance between the centre of curvature of the concave surface and the centre of the spherical articulation. Using the equations (8.1), (8.2) and (8.3) it can be obtained the total force acting in the horizontal plane:

$$F = W \cdot tg(\theta) + \frac{F_f}{cos(\theta)} = W \cdot \frac{d}{R * cos(\theta)} + \frac{F_f}{cos(\theta)} \tag{8.4}$$

Introducing the hypothesis of small oscillation:

$$cos(\theta) = 1, \qquad sin(\theta) = \theta = tg(\theta) = \frac{1}{R}$$

The equation (8.4) eases in the following:

$$F = \frac{W}{R} \cdot d + F_f \tag{8.5}$$

Finally, it explicates the friction force $F_f$ which is equal to:

$$F_f = W \cdot \mu \cdot cos(\theta) \tag{8.6}$$

And as already explained in the beginning of the paragraph is not constant and varies with some physical quantities, among which the most relevant are, straightforwardly, the relative sliding velocity and the compressive stress at the contact.
Therefore, by substituting the (8.6) into the (8.5) and introducing the sign function:

$$F = \frac{W}{R} \cdot d + W \cdot \mu \cdot sgn(\dot{d}) \tag{8.7}$$

where $sgn(\dot{d})$ gives back the sign of the horizontal velocity to represent the condition in which the dissipative force is opposite or congruent to the elastic one.

Considering the equation (8.7), it can be noted the first term $W/R \cdot d$ represents the elastic contribution while the second one $W \cdot \mu \cdot sgn(\dot{d})$), the dissipative force of the total lateral force F. The elastic term may be also seen as the re-centring force generated with the uplift of the mass sliding on the concave surface during the motion, which offers a rigidity:

$$K_2 = \frac{W}{R}$$

The constitutive law of the isolation devices like FPS, during motion and with reference to the horizontal response in terms of force, is idealized as bi-linear, based on three parameters $K_1$, $K_2$ and Q, in agreement to the figure 58.

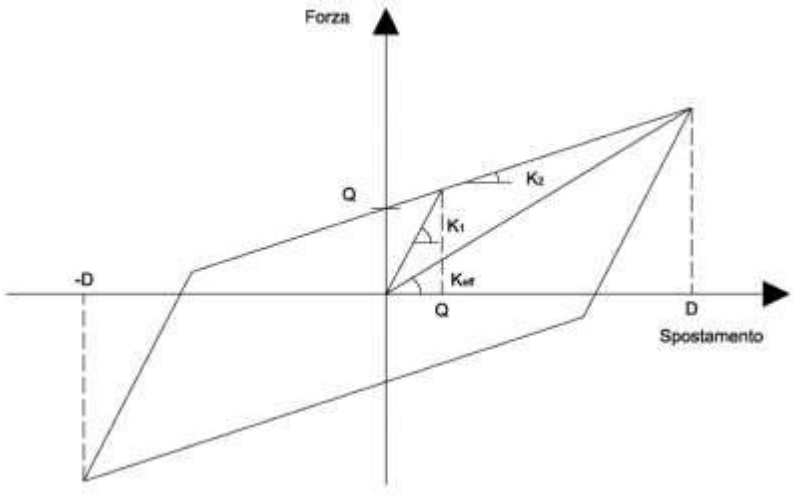


Figure 58-Constitutive law of the FPS system

The term $K_2$ is also called secondary rigidity to distinguish itself from the first one called initial rigidity $K_1$ presented by the device until developing the motion. Both of two terms give the slope of the paths of the diagram of hysteresis. Actually, the first path should be vertical simulating an infinitive rigidity because, until the lateral force reaches the static friction force, the device cannot move. On the other hand, it is assumed as a sub-vertical path and the value is estimated from the cycle of hysteresis or empirical considerations as multiple of $K_2$, Kelly suggested for instance $K_1 = 51 \cdot K_2$. So, it means, before braking the friction bonds, the relative sliding does not start, and the structure behaves as not isolated structure. Going beyond the static friction threshold the pendular motion starts following the second path with rigidity $K_2$.
As concern the figure above, it notes three different paths:

- The first path: has a slope ruled by rigidity $K_1$ and goes until the lateral force becomes equal to the static friction one, generally called characteristic force Q.

- The second path: once the lateral force has reached the static friction threshold, the friction coefficient decreases due to the starting of motion, so the lateral force continue to increase following the path characterized with a slope given by the lower rigidity $K_2$;

- The third path: the pendulum tries to invert its motion direction but to do this has to develop two times the static friction force for starting the motion again.

During the earthquake these three stages repeat in cyclic way performing the hysteretic cycles.

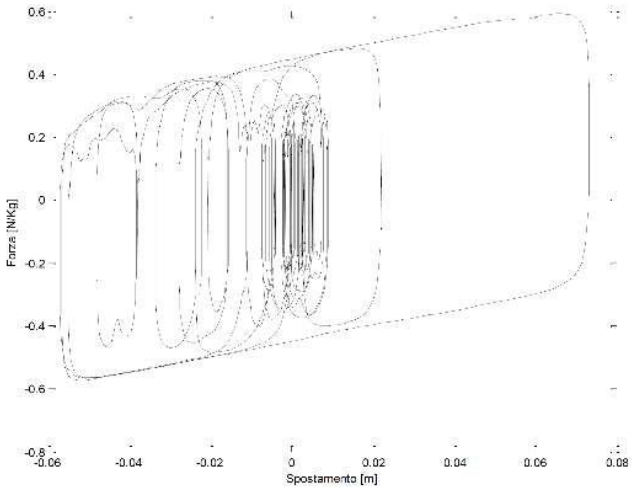


Figure 59-Typical Force-displacement hysteretic cycles

Moreover, it can be demonstrated that the fundamental period of the structure equipped with the friction pendulum system is given by the expression:

$$T = 2\pi * \sqrt{\frac{R}{g}}$$

## 8.2 Modelling Criterions

For a correct evaluation of isolation device properties, a suitable choice of the stiffness value has to be done. Considering the slope of the hardening path of the force-displacement device behaviour, corresponding to sliding motion phase, the period T of the isolated structure is a function, only, of the radius of curvature of the concave surface and it is equivalent to the one of the pendulum:

$$T = 2\pi \cdot \sqrt{\frac{M}{K}} = 2\pi \cdot \sqrt{\frac{M}{\frac{M \cdot g}{R}}} = 2\pi \cdot \sqrt{\frac{R}{g}} \tag{8.8}$$

Otherwise, assuming the secant stiffness value $K_{eff}$, defined as the ratio between the maximum horizontal force and the corresponding displacement performed by the isolator:

$$K_{eff} = \left(\frac{1}{R} + \frac{\mu}{d}\right) \cdot W \tag{8.9}$$

Replacing the (8.7) in (8.8), it obtains:

$$T_{eff} = 2\pi \cdot \sqrt{\frac{M}{K_{eff}}} = 2\pi \cdot \sqrt{\frac{M}{\left(\frac{1}{R} + \frac{\mu}{d}\right) \cdot M \cdot g}} = 2\pi \cdot \sqrt{\frac{R \cdot d}{(d + \mu \cdot R) \cdot g}} \tag{8.10}$$

If the system may be represented by means of linear equivalent model, the period $T_{eff}$ differs from T for a 14%, maximum. Therefore, the gap of the dynamic response of the structure between the linear and non-linear models turns out to be negligible. In lack of requirements needed to use the linear equivalent model, in agreement with the codes (NTC08), a non-linear analysis has to be performed in order to take into account the different paths of the force-displacement behaviour, in particular the different rigidities.

Another important parameter which characterizes the friction sliding bearing behaviour, is the equivalent viscous damping coefficient. It gives a measure of the dissipated energy due to friction phenomenon, it can be estimated as:

$$\xi_{eff} = \frac{hysteretic\ cycle\ area}{2\pi \cdot K_{eff} \cdot d^2} \tag{8.11}$$

The previous formula is carried out from the equivalence between the dissipated energy for friction and viscous behaviour. Considering the hysteretic cycle equal to $4\mu Wd$ and remembering the (8.8), it can be obtained:

$$\xi_{eff} = \frac{4\mu Wd}{2\pi \cdot \left(\frac{1}{R} + \frac{\mu}{d}\right) \cdot W \cdot d^2} = \frac{2\mu}{\pi \cdot \left(\frac{d}{R} + \mu\right)} \tag{8.12}$$

From which can be noted how the equivalent damping coefficient is a function of the friction coefficient, the radius of curvature and the displacement demand, with reference to this latter, it can be taken as the design displacement for the limit state considered.
In general, the object value for isolated structure is the displacement for the life safeguard limit state (SLV).
At the same time, for designing the devices, related to the system fragility and the failure mechanisms, the collapse limit state displacement is used (SLC).

## 8.3 Linear modelling

The isolation system is idealized as a linear equivalent model by means of a linear spring, with its own stiffness and equivalent viscous damping coefficient, representing a simplification in the modelling and analysis phases, however some requirements have to be accomplished, according to NTC08, for using such linear model, as following:

- The equivalent stiffness of the isolation system has to be at least equal to the 50% of the secant one for cycles with a displacement of 20% of the reference one. For pendular systems such limitations result in:
  $\frac{R}{d_{dc}} \leq \frac{1}{3}\mu_{din}$

where $d_{dc}$ is the displacement of the centre of rigidity due to seismic action given by the limit state considered, R is the radius of curvature and $\mu_{din}$ the dynamic friction coefficient.

- The equivalent linear damping coefficient of the isolation system has to be lower than 30%

- The force-displacement characteristics of the isolation system have not to vary more than 10% due to the deformation velocity variation, within $\pm$ 30% of the design value, and the vertical action on the devices, within the design variability

- The increasing of the force at the isolation system for displacement between $0.5d_{dc}$ and $d_{dc}$, has to be at least equal to the 2.5% of the superstructure weight. Such requirement limits a radius of curvature up to 20 times the design displacement

Therefore, when, at least, one of these prescription is not respected, a non-linear modelling is required with a more suitable constitutive law and adopting the motion equations with a pitch by pitch integration.

# 9. DYNAMICS AND DESCRIPTION OF THE PROBLEM

The seismic isolation arises as one of the most breakthrough techniques for improving the seismic response of existing bridges, moreover, it is a practical solution also for new bridges when the traditional design way is not suitable or economic [7].

With the help of this technique, the superstructure is decoupled from the substructure by means of isolation devices, in particular, as regards this study, friction pendulum systems. As described in the previous chapter they are placed between the superstructure (deck) and the substructures (piers or abutments). In static conditions, they behave as traditional vertical unidirectional supports, but, during an earthquake, enhance the bridge flexibility lengthening its fundamental period and dissipating of the input energy. On the other hand, a longer period means higher displacements which can be controlled adding damping devices.

Finally, the seismic isolation reduces the horizontal seismic force acting on the deck which in turn reduces the force exchanged with the substructure and in turn with foundations.

The objective of this chapter is to study such devices, modelled, with a non-linear behaviour, showing, how the various parameters and their variations, involved inside the model, affect the response of the structure, by means of some available professional platforms, in order to identify a reliable way for dealing with the problem.

## 9.1 General information on the problem

The task is focused on a symmetric bridge, although, in particular, the pier-abutment interaction is at the centre of this study. Therefore, a suitable model needs to be identified to study the relative displacements, between the superstructure and the substructure one, which are made through the positioning of the FPSs.

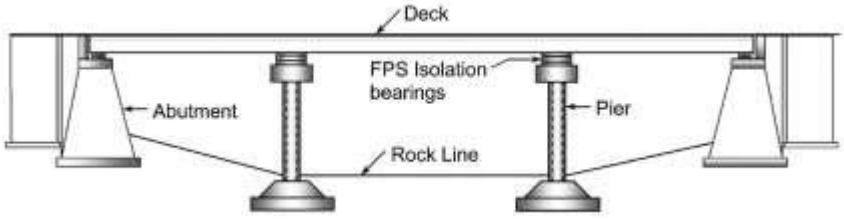


Figure 60-Bridge scheme under exam

It will be used a six-degree of freedoms model, where five of them concerns to the pier and the last one, the deck (5+1 d.o.f model), as shown in the picture.

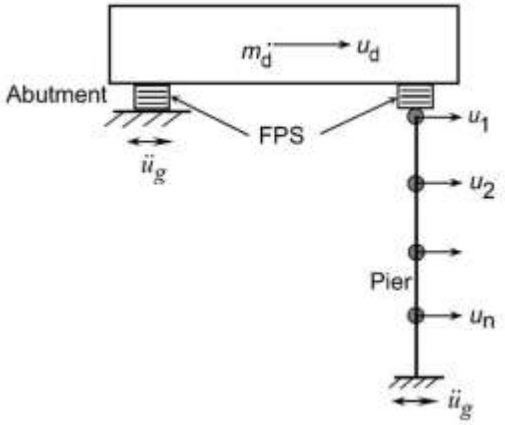


Figure 61-6 d.o.f mathematical model

The analysis performed, to take into account the non-linearities of the problem, is the non- linear dynamic analysis with pitch-by-pitch integration. The response of the structure is evaluated from a direct integration of the equations of motion of the structure subjected to a time history. This method of analysis is the most complex and complete one, it allows to know the stress-deformation behaviour of the whole structure and each of its components over the time. It is able to represent the hysteretic behaviour of the structure taking into account the non-linear behaviour of the devices. Besides, this kind of analysis is required by codes (NTC08) when the isolation system is not representable with a linear equivalent model.

## 9.2 Equations of motion

In this paragraph it will be shown the equations of motion which rule the interaction among piers, abutments, deck and isolators subjected to a seismic excitation. However, some starting hypothesis have to be taken into account:

- The structure under analysis is symmetric for sake of simplicity
- The deck, piers and abutments have to stay within the linear elastic field
- The isolator is modelled with a non-linear constitutive law depending on the relative sliding velocity

This system is based on Jangid's theory [7], where the bridge consists in the superstructure, made with a continuous rigid multi-span plate deck supported by the isolator devices, and the substructure, made with the abutments and piers in reinforced concrete. Whereas, as concern the isolator devices, the friction pendulum systems (FPS), their behaviours are described by (Zayas et al., 1990) [9].
Talking about the modelling of the structure systems in the previous figure, it has to pay attention to some considerations:

- The deck is only a mass $m_d$ placed on both the abutment and pier, detached from the superstructure by means of the devices, and considered as straight and rigid (without slope inclination)

- The abutment is modelled as a fully supported bearing on which the FPS, supporting one half of the deck ($m_d/2$), is placed, so one horizontal degree of freedom is assigned

- The pier is modelled as lumped mass systems, equally segmented, in which each node has a horizontal degree of freedom, so, the mass of each segment is equally distributed between the upper and lower nodes, and, furthermore, the node at the contact with the foundation is considered as fully supported bearing.

- The FPS is idealized as isotropic, it means equal characteristics in both horizontal directions, and with a bilinear force-displacement behaviour as shown in the figure 62

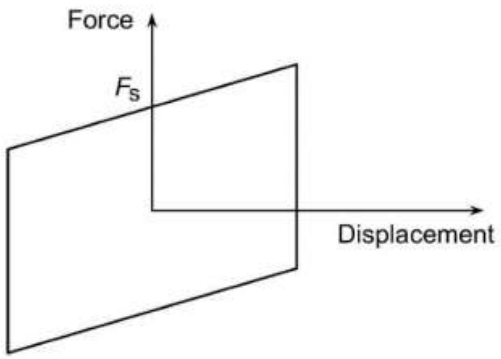


Figure 62-Bilinear stress-strain law of the isolator

- The bearing motion is characterized by a complete lack of stick-slip tendencies

- The analysis is performed only in the longitudinal direction of the structure, therefore, also, the seismic excitation. The transverse, vertical and back-up systems effects are neglected in this work.

Since the basic considerations for modelling are already given, it can start introducing the Jangid' s equations and modify them for considering, in particular, the pier-abutment interaction.
The equations system governing the isolated bridge motion are:

$$m_d \ddot{u}_d + F_a + F_p = -m_d \ddot{u}_g \tag{9.1}$$

$$[M]\{\ddot{u}\} + [C]\{\dot{u}\} + [K]\{u\} = -[M_g]\{1\}\ddot{u}_g \tag{9.2}$$

Where $m_d$ represents the mass of the deck, $F_a$ and $F_p$ are the forces exchanged at the level of isolation devices (FPS) the first one between the deck and the abutment and the second one between the deck and the pier. Whereas, [M], [C] and [K] are respectively the mass, damping and stiffness matrices of the system (nxn dimension, n is the number of nodes of the pier in which is subdivided), $[M_g]$ is the mass matrix associated to the ground acceleration $\ddot{u}_g$, and $\{\ddot{u}\}$, $\{\dot{u}\}$, $\{u\}$ are, respectively, the acceleration, velocity and displacement vectors, while $\{1\}$ is a unit vector representing the level at which the ground acceleration is acting.
The above-mentioned equations are written with respect to an absolute reference system, so, in other words, the displacements are referred to the base of the pier. Another way for describing the equations is by using the Kelly's theory [19]. This latter theory uses relative displacements (drift) instead of absolute ones, so:

$$\ddot{u}_d = \ddot{v}_d + \ddot{v}_{p,1} + \cdots + \ddot{v}_{p,n}$$
$$\ddot{u}_{p,n} = \ddot{v}_{p,1} + \cdots + \ddot{v}_{p,n}$$
$$\ddot{u}_{p,1} = \ddot{v}_{p,1}$$

And the equations (9.1) and (9.2) can be re-written:

$$m_d\left(\ddot{v}_d + \ddot{v}_{p,1} + \cdots + \ddot{v}_{p,n}\right) + F_a + F_p = -m_d \ddot{u}_g \tag{9.3}$$

$$[M]\{\ddot{v}\} + [C]\{\dot{v}\} + [K]\{v\} = -[M_g]\{1\}\ddot{u}_g \tag{9.4}$$

Where $\{\ddot{v}\}$, $\{\dot{v}\}$ and $\{v\}$ are, respectively, the relative acceleration, velocity and displacement vectors and the others remain the same previous saw.
At this time, it is necessary to explicate what $F_a$ and $F_p$, therefore, with the expression:

$$F_a = \frac{m_d g}{2R} u_{d,i} + \mu_d \frac{m_d g}{2}\, sgn(\dot{u}_{d,i}) \tag{9.5a}$$

$$F_p = \frac{m_d g}{2R} (u_{d,i} - u_{p,n)} + \mu_d \frac{m_d g}{2}\, sgn(\dot{u}_d - \dot{u}_{p,n}) \tag{9.5b}$$

It can be noted that $m_d g/2$ is half weight of the deck (W/2), then (W/2R) is the stiffness $k_d$.
Inside the previous equation two terms are present, the first is the elastic one, depending on the stiffness of the superstructure, and the second is the friction one, depending on the friction phenomenon, taking place by means of the FPS. The friction coefficient can be expressed by the following law:

$$\mu_d = f_{max} - (f_{max} - f_{min}) e^{-\alpha|\dot{u}_d|} \tag{9.6}$$

Where $f_{max}$ represents the maximum friction coefficient at high sliding velocity, $f_{min}$ represents the minimum one at low sliding velocity, $\alpha$ is a control parameter depending on the compressive stress at the contact, temperature and surface conditions, usually assumed equal to 30, and $|\dot{u}_d|$ is the absolute value of the sliding velocity.
Since, also $F_i$ is depending on both displacements and velocities, by replacing the relative physical quantities into (9.5):

$$F_p = \frac{m_d g}{2R} v_d + \mu_d \frac{m_d}{2} g\, segno(\dot{v}_d) \tag{9.7}$$

$$F_a = \frac{m_d g}{2R} (v_d + v_{p,n} + \cdots + v_{p,1}) + \mu_d \frac{m_d}{2} g\, segno(\dot{v}_d + \dot{v}_{p,n} + \cdots + \dot{v}_{p,1}) \tag{9.8}$$

Resuming, the whole system of equations can be written in the matrix form:

$$\begin{bmatrix} m_d & m_d & \dots & m_d \\ m_d & m_d + m_{p,1} & \dots & m_d + m_{p,1} \\ \vdots & \vdots & \ddots & \vdots \\ m_d & m_d + m_{p,1} & \dots & m_d + \sum m_{p,i} \end{bmatrix} \begin{pmatrix} \ddot{v}_d \\ \ddot{v}_{p,1} \\ \vdots \\ \ddot{v}_{p,n} \end{pmatrix} + \begin{bmatrix} 2c_d & c_d & \dots & c_d \\ c_d & c_{p,1} + c_d & \dots & c_d \\ \vdots & \vdots & \ddots & \vdots \\ c_d & c_d & \dots & c_{p,n} + c_d \end{bmatrix} \begin{pmatrix} \dot{v}_d \\ \dot{v}_{p,1} \\ \vdots \\ \dot{v}_{p,n} \end{pmatrix} +$$

$$+ \left( \begin{bmatrix} k_d & 0 & \dots & 0 \\ 0 & k_{p,1} & \dots & 0 \\ \vdots & \vdots & \ddots & \vdots \\ 0 & 0 & \dots & k_{p,n} \end{bmatrix} + \begin{bmatrix} 0 & 1 & \dots & 1 \\ 1 & 1 & \dots & 1 \\ \vdots & \vdots & \ddots & \vdots \\ 1 & 1 & \dots & 1 \end{bmatrix} \left( {}^{W}/_{2R} \right) \right) \begin{pmatrix} v_d \\ v_{p,1} \\ \vdots \\ v_{p,n} \end{pmatrix} +$$

$$+ \begin{pmatrix} {}^{W}/_{2R} \\ 0 \\ \vdots \\ 0 \end{pmatrix} u_d + \begin{pmatrix} 1 \\ 0 \\ \vdots \\ 0 \end{pmatrix} \mu_{d,p} \frac{\mathrm{W}}{2} \, sgn(\dot{v}_d) +$$

$$+ \begin{pmatrix} {}^{W}/_{2R} \\ 0 \\ \vdots \\ 0 \end{pmatrix} v_d + \mu_{d,a} \frac{\mathrm{W}}{2} \, sgn \left( \left[ \begin{pmatrix} 1 \\ 0 \\ \vdots \\ 0 \end{pmatrix} \dot{v}_d + \begin{pmatrix} 0 \\ 1 \\ \vdots \\ 0 \end{pmatrix} \dot{v}_{p,n+\dots+} \begin{pmatrix} 0 \\ 0 \\ \vdots \\ 1 \end{pmatrix} \dot{v}_{p,1} \right] \right) =$$

$$= - \begin{bmatrix} m_d & 0 & \dots & 0 \\ 0 & m_d + m_{p,1} & \dots & 0 \\ \vdots & \vdots & \ddots & \vdots \\ 0 & 0 & \dots & m_d + \sum m_{p,i} \end{bmatrix} \begin{pmatrix} 1 \\ 1 \\ \vdots \\ 1 \end{pmatrix} \ddot{u}_g \qquad (9.9)$$

with $\mu_{d,p} \propto (\dot{v}_d)$, and $\mu_{d,a} \propto \left( \left\| \left[ \begin{pmatrix} 1 \\ 0 \\ \vdots \\ 0 \end{pmatrix} \dot{v}_d + \begin{pmatrix} 0 \\ 1 \\ \vdots \\ 0 \end{pmatrix} \dot{v}_{d+\dots+} \begin{pmatrix} 0 \\ 0 \\ \vdots \\ 1 \end{pmatrix} \dot{v}_d \right] \right\| \right)$

## 9.3 Non-dimensional equations of motion

The non-dimensional form of the equation can be derived by using the concepts of both time scale and length scale. These concepts have been introduced first by Makris and Black [10, 11] for the analysis of the elastoplastic systems under pulse-type motions, and later extended to the case of ground motions without distinct pulses [12, 13, 14]. Moreover, they have been employed for studying other types of systems [15, 16], also including rocking columns [17] and rigid masses or rocking blocks mounted on single concave sliding bearings [18, 19].

The time scale is herein assumed equal to $1/\omega_g$, where $\omega_g$=2π/Tg is a circular frequency content of the ground motion input. However, the $\omega_g$ parameter is carried out from the ratio PGA/PGV (peak-ground-acceleration/peak-ground-velocity) which results a good indicator of the frequency content and of other characteristics of ground motion records, helping to reduce the scatter in the response [20].

The length scale is assumed as the ratio $IM/\omega_g^2$, where IM is a measure of the seismic intensity with the dimension of an acceleration and it is such that $\ddot{u}_g(t) = IM\ \lambda(\tau)$, where $\lambda(\tau)$ is a non-dimensional function of the time describing the seismic input history. Besides, introducing the following parameters:

- Mass ratio: $\gamma = \frac{m_p}{m_d}$

- Damping coefficients: $\xi_d = \frac{c_d}{2m_d\omega_d}$ $\xi_p = \frac{c_p}{2m_p\omega_p}$

- Natural frequencies: $\omega^2{}_d = \frac{k_d}{m_d}$ $\omega^2{}_p = \frac{k_p}{m_p}$

It is possible, manipulating the previous system of equation, to identify the non-dimensional form of the equations, wherein the non-dimensional displacement parameters appear:

$$\psi_d = \frac{v_d\omega_g^2}{IM}$$

$$\psi_p = \frac{u_p \omega_g^2}{IM}$$

where $\psi_d$ and $\psi_p$ respectively represent the motion of the superstructure and the substructure.
Similarly, also other non-dimensional parameters Π can be identified, controlling the system non-dimensional response to the seismic input $\lambda(\tau)$, these are:

$$\Pi_\mu = \mu(\dot{\psi}_d)\frac{g}{IM}$$

$$\Pi_\gamma = \gamma$$

$$\Pi_{\xi_p} = \xi_p \qquad \Pi_{\xi_d} = \xi_d$$

$$\Pi_{\omega_g} = \frac{\omega_d}{\omega_g} = \frac{T_g}{T_d} \qquad \Pi_p = T_p$$

where $\Pi_{\omega_p}$ measures the degree of isolation [21], $\Pi_{\omega_g}$ is the ratio between the isolator frequency and the circular frequency representative of the ground motion input, $\Pi_\gamma$ is the previous defined mass ratio, $\Pi_{\xi_p}$ and $\Pi_{\xi_d}$ describe the viscous damping inherent respectively to the system and the isolator. Finally, $\Pi_\mu$ measures the isolator strength, provided by the friction coefficient $\mu(\dot{\psi}_d)$, relative to the seismic intensity. Since this parameter depends on the response through the velocity $\dot{\psi}_d$ the following parameter is used in its stead:

$$\Pi^*_\mu = \mu_{max}\frac{g}{IM} \tag{9.10}$$

At the final stage, the non-dimensional response parameters relevant to the performance of the isolated system are:

$$\psi_{d,max} = \frac{v_{d,max}\omega_g^2}{IM}$$

$$\psi_{p,max} = \frac{u_{p,max}\omega_g^2}{IM}$$

$v_{d,max}$ is the peak isolator relative displacement (important for the design of the single concave sliding isolator and the seismic gap around the deck) and $v_{p,max}$ is the peak pier relative displacement (important for the design of the pier, related to internal forces developed). It is noteworthy how the non-dimensional seismic response of the system does not depend on the seismic intensity level IM, but it depends only on $\Pi_{\omega_p}, \Pi_{\omega_g}, \Pi_{\xi_p}, \Pi_{\xi_d}, \Pi_{\gamma}, \Pi^*{}_{\mu}$ and on the function $\lambda(\tau)$, describing the frequency content and time-modulation of the seismic input. It has to be highlighted that, even if $\Pi^*{}_{\mu}$ is based on the maximum friction coefficient $f_{max}$, the normalized system response depends on the other properties of the isolator such as $\alpha$ and $f_{min}$, which appear in the model developed by Mokha and Constantinou [5, 6] and control the friction variations. Nevertheless, for simplifying, once again the problem, in the following analysis, it is assumed $f_{max} = 3\, f_{min}$, extracted from regressions on the experimental results, while $\alpha$ is assumed equal to 30 [21].

# 10. NUMERICAL MODEL

## 10.1 Modelling with Matlab&Simulink software

The initial stage of this work consists in trying to develop an easy, fast and efficient instrument of calculation which allows the numerical modelling of the n+1 GDL system, with the hypothesis of non-linear behaviour of the device. Thanks to Simulink (internal app of Matlab software), it is possible to use a powerful and intuitive graphic interface. It is a block diagram environment for multidomain simulation and Model-Based Design. It supports system-level design, simulation, automatic code generation, and continuous test and verification of embedded systems. Simulink provides a graphical editor, customizable block libraries, and solvers for modelling and simulating dynamic systems. It is integrated with Matlab, enabling you to incorporate Matlab algorithms into models and export simulation results to Matlab for further analysis.
An example is given in the figure 63 in order to show the graphic interface and its functioning.

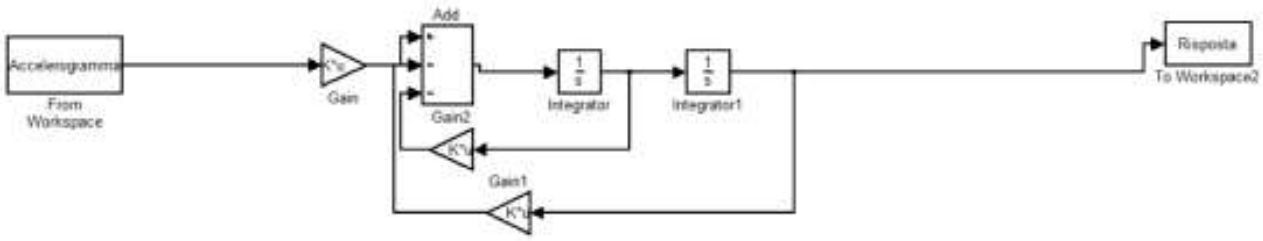


Figure 63-Simulink interface example

Starting from the left side, there is a block representing the input seismic time-history induced at the base of the structure due to the earthquake. Then, the software performs the pith-by-pitch integration. Two integrator blocks cascaded, equal to the order of the differential equations to solve, allow to carry out the velocity-history and displacement one, performed by the respective integrator blocks.
In addition, there are some “gain” blocks which multiply the acceleration-history, velocity and displacement ones. In this case this two “gain” blocks are the damping and the stiffness matrices of the system. Therefore, the algorithm, at each step and in a cyclic way, passing the sum block wherein

each contribution of the dynamic equation is summed, once multiplied for its own gain block, gives back the results by means of the “response” block on the right side.

Since a rough idea of the used software has been given, it can go further for describing how the algorithm has been implemented. The equations of motion reported in the previous paragraph are the basis for the development of the algorithm which has to take into account the pier-abutment interaction given by means of the deck.

This work starts by modelling the n+1 GDL system into the Matlab-Simulink environment. The structure is isolated with FPSs in which both superstructure and substructure work in the linear elastic field whereas, the devices work with a non-linear constitutive law.

The simulation process works because of the Matlab-Simulink worksheets interaction. The first defines the input variables, providing the assembling of the matrices involved in the equations, using the initial parameters, and the loading of the time-histories. The second takes the variables, carried out from the first one, and solve the equations of motion with a pitch-by-pitch integration. Then, the results return into the Matlab script for generating the data file.

The final Simulink worksheet is shown in the following figure. It can be seen how the signal enters from the left side, multiplied by a gain block which normalizes the equation with respect to the mass of the system. Thus, it proceeds with the double integration process as previous explained. However, in this case the normalized velocity vector enters also into the gain blocks 7, 8 and 9. These latter blocks are able to represent the mechanical friction behaviour of the FPS [22], depending on the velocity, and generate the friction contribution forces on both pier and abutment, given by means of FPS. Whereas, the normalized displacement vector also into the gain 5 and 11, representing the elastic contribution forces on both pier and abutment, again.

Finally, for testing the stability of the model, it was investigated which kind of integration algorithm performed the results in the more suitable way. By comparing the different results and on the basis of the efficiency of these ones, it was established that the ode3 with a fixed step of 0.0005 s is sufficient for the aim, because it was tested that smaller steps do not perform more refined results to justify the time lengthening of the analysis.

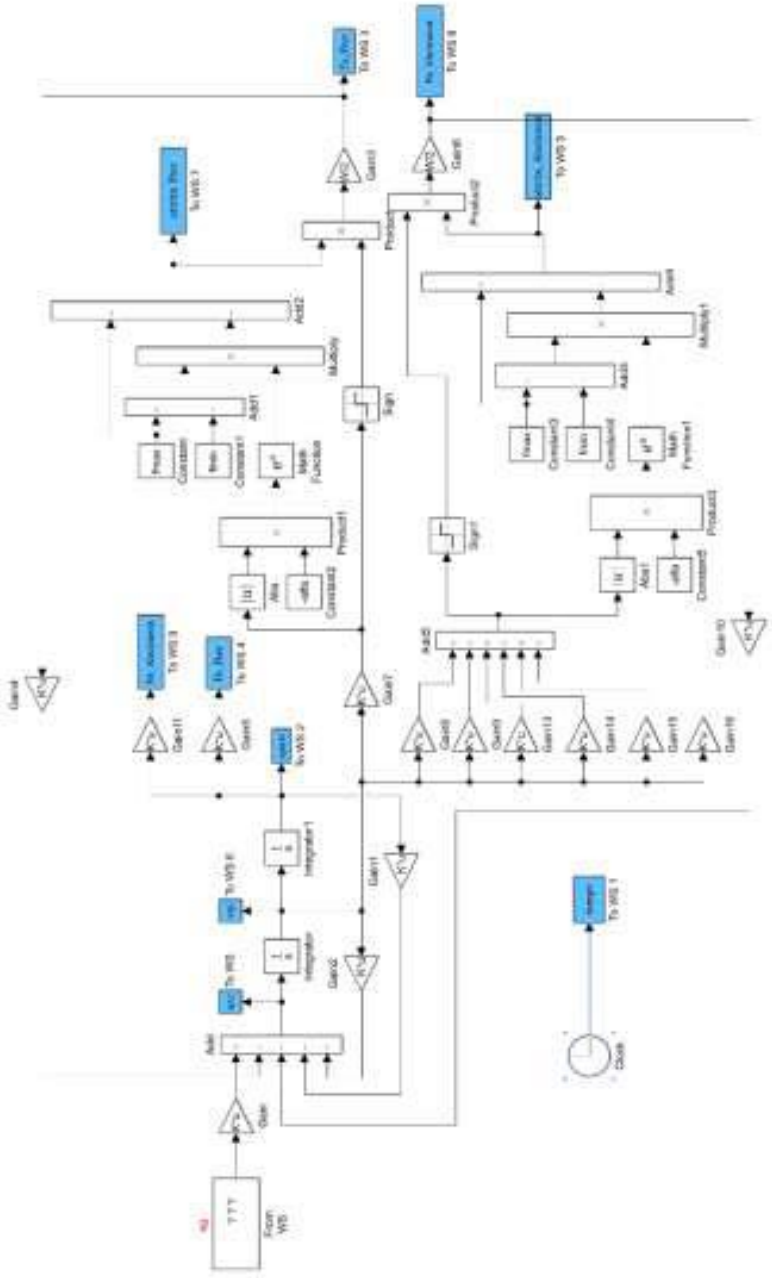

Figure 64-Simulink 6 d.o.f model

## 10.2 Modelling with sap2000 software

Since, a validation of the matlab-simulink model is needed, the same structure was modelled with the professional software sap2000, in order to verify the suitability of the results obtained with the matlab-simulink algorithm.

By means of this software, the 6 degree-of-freedom structure was defined, where the abutment and the pier was rigidly linked at the top, going to represent the deck. Then, between the superstructure and substructure, a sliding friction device was implemented, modelling it with the finite element

“NLink” (“Friction pendulum system” type), which is a non-linear link with biaxial behaviour that allows to model the friction slider in 3D, coupling the friction properties, defined by the shear deformations occurring due to the sliding between the two surfaces characterized by a variable radius of curvature (null for flat surfaces and higher than zero for concave surfaces). Moreover, a “gap” element is defined for representing the non-tensile strength of the device, because, as previous said in the hypothesis, it can work only in compression.

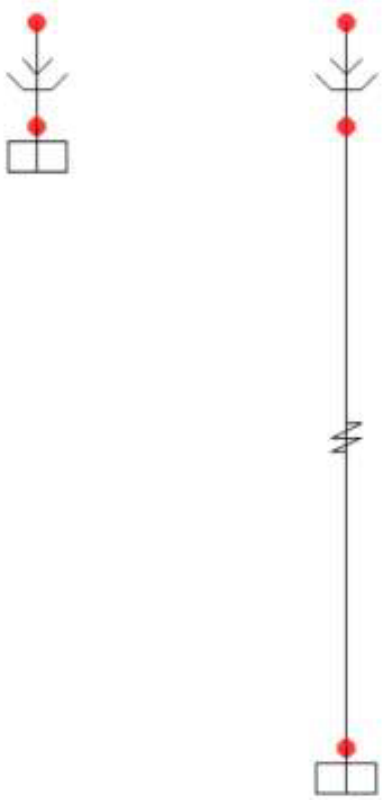

Figure 65-Sap2000 model

## 8.3 Numerical validation of the model

Finally, by comparing the results obtained with both Matlab-Simulink and Sap2000 for a single earthquake, the validation of the model has been reached. Different comparisons were made changing the parameters of the structure ($T_p$, $T_d/T_g$, $\gamma$ and $\mu$) and the results are showed below.

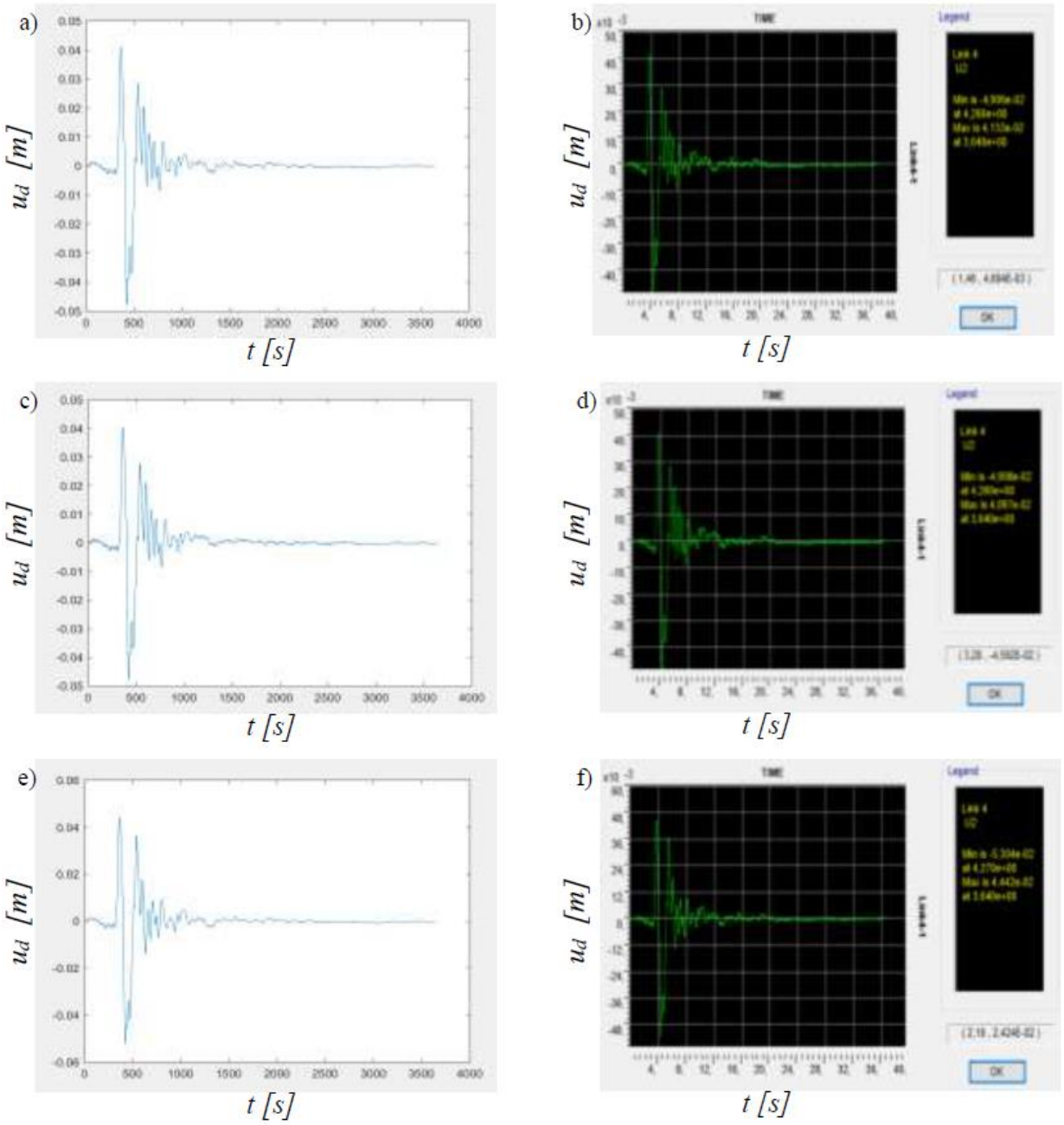


Figure 66-MATLAB® vs SAP2000® results comparison in terms of deck displacement: a) and b) for $f_{max}$ = 0.03, $f_{min}$= 0.01; c) and d) for $f_{max}$ = 0.03, $f_{min}$ = 0.015; e) and f) for $f_{max}$ = 0.025, $f_{min}$ = 0.01

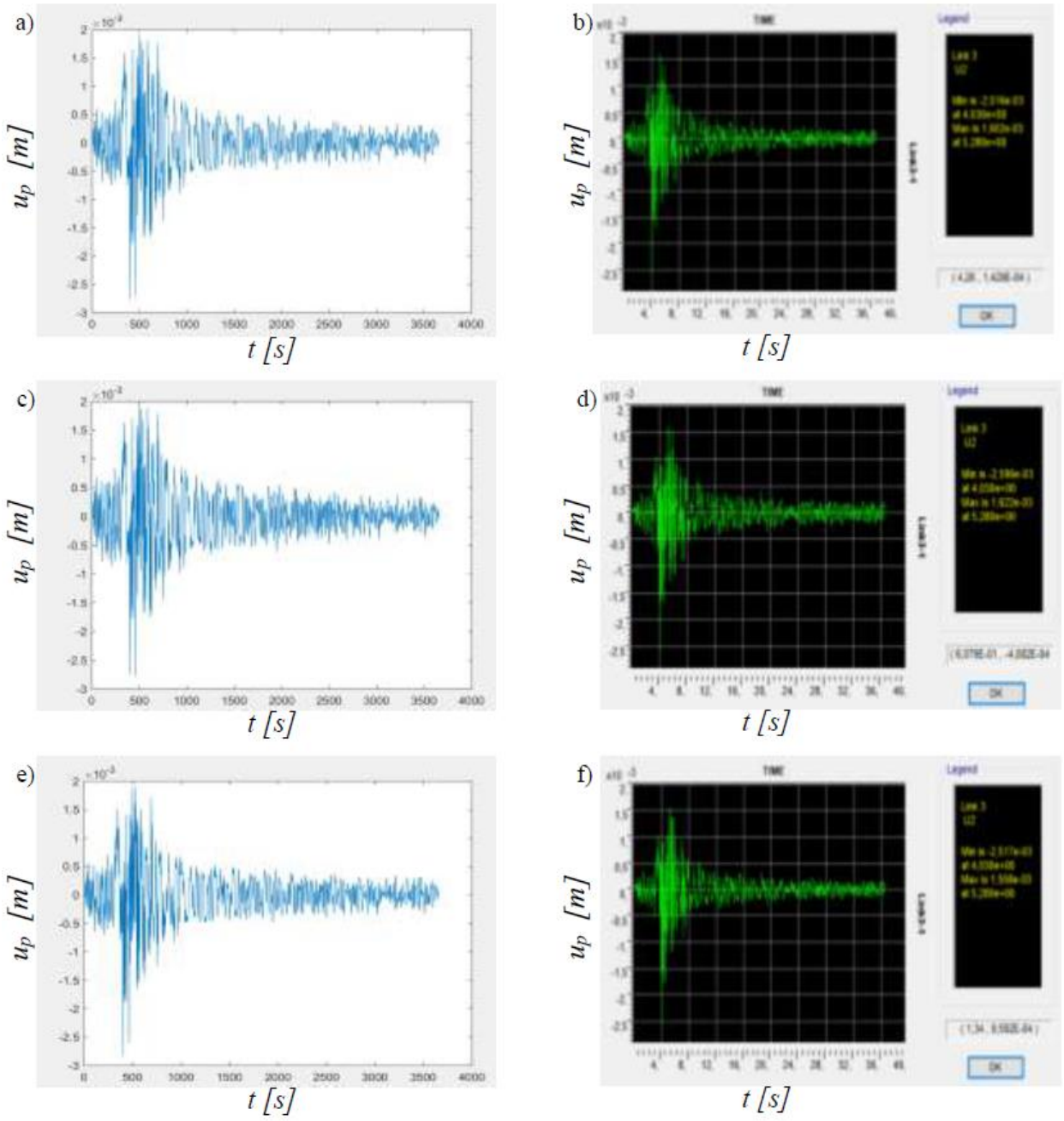


Figure 67-MATLAB® vs SAP2000® results comparison in terms of pier displacement: a) and b) for $f_{max}$ = 0.03, $f_{min}$= 0.01; c) and d) for $f_{max}$ = 0.03, $f_{min}$ = 0.015; e) and f) for $f_{max}$ = 0.025, $f_{min}$ = 0.01

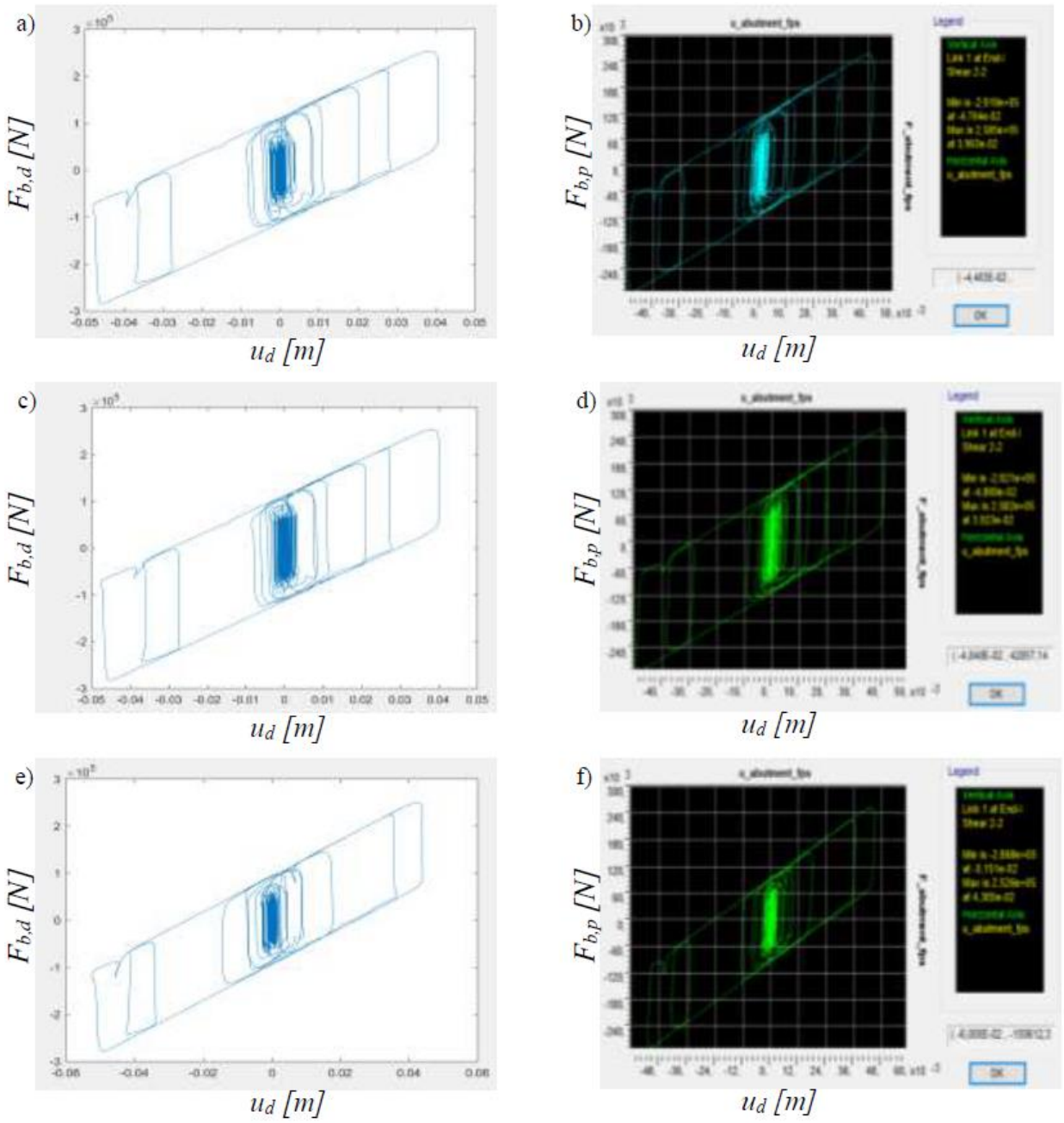


Figure 66-MATLAB® vs SAP2000® results comparison in terms of deck velocity dependence: a) and b) for $f_{max}$ = 0.03, $f_{min}$= 0.01; c) and d) for $f_{max}$ = 0.03, $f_{min}$ = 0.015; e) and f) for $f_{max}$ = 0.025, $f_{min}$ = 0.01

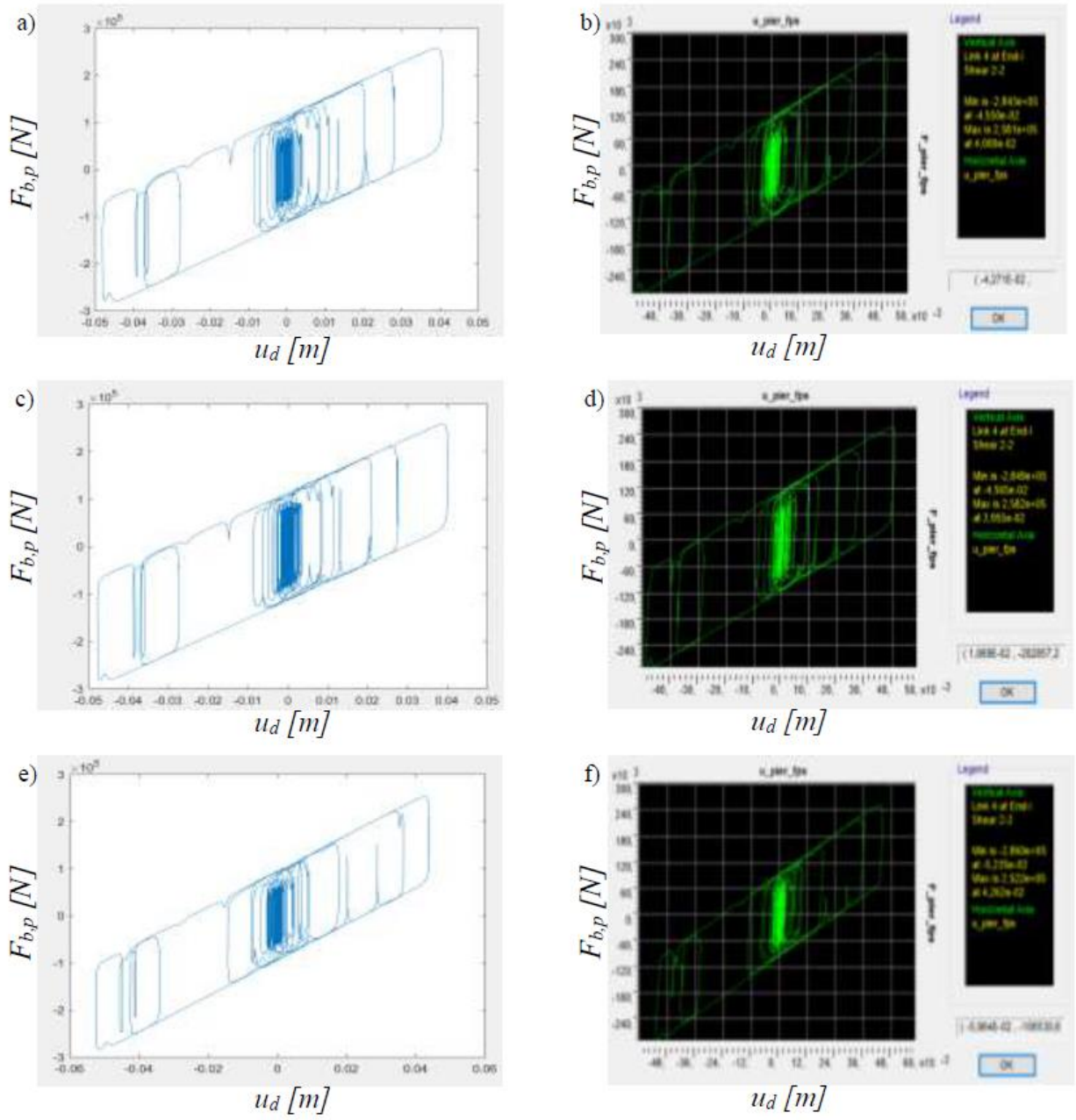


Figure 67-MATLAB® vs SAP2000® results comparison in terms of pier velocity dependence: a) and b) for $f_{max}$ = 0.03, $f_{min}$= 0.01; c) and d) for $f_{max}$ = 0.03, $f_{min}$ = 0.015; e) and f) for $f_{max}$ = 0.025, $f_{min}$ = 0.01

The figures 63-67 show how the results are similar and the tolerable differences are given due to the different integration algorithms of the two software.

# 11. PARAMETRIC STUDY

## 11.1 Modelling parameters

As concern the input parameters, they are extrapolated from an accurate work of searching among 15 papers present in literature. Two classes of input parameters can be distinguished. The first one is made of seismic input records (85 records), coming from natural earthquake event, which are:

- 45 far field records, $T_g$ (tables 1-3)

- 40 near fault records, $T_g$ (table 4)

The second one, whereas, involves a series of deterministic parameters, such following:

- 4 pier periods, $T_p$ [23]

- 15 non-dimensional isolation period ratios, $T_d/T_g$

- 3 mass ratios, $\gamma$

- 85 friction dynamic coefficient, related to sliding surfaces of the FPS, described by (9.6)

The results performed with Matlab & Simulink model are obtained through 1.300.500 analysis combining the parameters $T_p$, $T_d/T_g$, $T_g$, $\gamma$ e $\mu$. The script works with these 5 parameters by means of 4 cycles "for-end" settled, one into the other, where going for the outer to the inner ones, in order it can be noted, $T_d/T_g$, $T_p$, $\gamma$, $\mu$ and $T_g$.

## 11.2 Seismic input description

In the non-dimensional form system of equations, the seismic input is the described by the seismic intensity measure in the context of the Performance-Based Earthquake Engineering (PBEE), and by the non-dimensional function $\lambda(\tau)$, which describes the time-history of the ground motion and contains the information on the duration of strong shaking and the frequency content. For a given

site, these characteristics vary significantly from record-to-record and they are affected by many variables, including source-to-site distance, the earthquake magnitude and the local conditions. Thus, in the performance assessment of structures more than one record needs to be considered or a stochastic representation of the seismic input must be employed to describe the variability of these characteristics. Although the Response Spectrum or the Fourier Spectrum describe fully an earthquake ground motion, it is often more practical and convenient to characterize it in terms of few parameters. For this reason, many studies have been devoted in the last year to the identification of advanced IMs capable of synthetically describing the most important features of an earthquake and its effect on structures [24]. In the same context, significant research efforts have been made to define the best scalar measures representing the frequency content of the seismic input. These measures can be used conveniently as time-scales in developing non-dimensional problem formulations for the seismic response assessment of structural systems, as the one described in the previous section. In this work, the PGA and the ratio $\omega_g = PGA/PGV$ are used to define respectively the intensity measure IM and the time scale $1/\omega_g$. The ratio PGA/PGV has been extensively employed for analysing the influence of the ground motion characteristics on the performance of isolated systems [25, 26, 27], and numerous works have demonstrated that it provides useful information on the frequency content and other characteristics of an input motion [28-31]. In general, inverse correlation can be found between the PGA/PGV ratio and the magnitude, the source-to-site distance, the predominant period of the site [30], the duration, and also the stochastic bandwidth indicator, which gives a measure of the frequency band of a random process [31]. Results of seismological studies are often available that allow to estimate the probability distribution of PGA/PGV at a site [32]. For such reasons, the PGA/PGV has been preferred for this study to other time scales commonly employed in the literature such as the predominant period of the ground motion $T_m$ [11, 12, 13, 33]. However, it should be observed that a strong inverse correlation is found between PGA/PGV and $T_m$ [31]. Thus, these measures are equally good for describing the characteristics of the ground motion input. Moreover, for pulse-like near-fault ground motions, the pulse period and velocity amplitude have been found to correlate well with the peak inelastic response [10]. These two ground motion parameters are however not considered in this study for the nondimensionalization of the equation of motion because many ground motion records do not contain distinct pulses [12, 13].

In this work, two different types of records are considered. The first set consists of 45 far field (FF) records which have been widely used for studies on the effect of the PGA /PGV on the response of structures. These records are subdivided into three subsets based on their PGA/PGV ratios (high, medium or low), with 15 records in each subset, as reported in tables 1-3. Usually, high PGA/PGV ratios are associated with records of short duration and high energy content within the high frequency

range, whereas low PGA/PGV ratios denote records with long duration and high energy content within the low frequency range [28, 29, 34, 35]. Thus, low PGA/PGV ratios are expected to be more critical for isolated systems such as the one considered.

The second set of records consists of 40 near fault (NF) ground motions, whose characteristics are reported in table 4. This set of records has been included in the study to investigate whether the proposed ground motion parameters and non-dimensional formulation are capable of describing the essential characteristics of the seismic input and provide a non-dimensional response which is not strongly affected by the type of records considered. As expected, on average the NF records are characterized by low PGA/PGV ratios, below 0.8 g. Only in one case a high value of PGA/PGV, higher than 1 g, is observed.

Records with the same PGA/PGV ratio may have a different effect on the analysed system, depending on the influence of those features of the ground motion that PGA/PGV is not able to describe. Thus, despite the nondimensionalization involving the time scale $1/\omega_g$, a dispersion is expected in the normalized response. Obviously, the dispersion would be zero in the case of a harmonic input with circular frequency $\omega_g$.

## 11.3 Parameters ranges

This section illustrates the ranges within the parameters are moving. The parameters $\xi_d$ and $\xi_p$ are assumed respectively equal to 0 and 5%, the parameter $T_p$ is varied in the range between 0.05 (rigid superstructure) and 0.20 (flexible superstructure), $\gamma$ in the range between 0.10 and 0.20, $\Pi^*{}_\mu$ in the range between 0 (no friction) and 1.5 (very high friction), and $T_d/T_g$ in the range between 1.5 and 16. It is noteworthy that in design practice, high values of $\Pi^*{}_\mu$ should be avoided because they may cause stick and values of $T_d/T_g$ higher than 1.5, since $T_d$ is usually equal or higher than 0.4 s for isolated systems, and $T_g$ is, usually, smaller than unity.

## 11.4 Probabilistic study

The probabilistic response is evaluated by considering separately the set of far field records (for a total of 45 ground motions) and the set of near fault records (40 ground motions). The ode23 integration algorithm available in Matlab-Simulink is employed to solve the dynamic equations of motion for each value of the parameters varied in the parametric study and for the different ground motion considered. By assuming that the response parameters follow a lognormal distribution [21,

36], only the first two moments of the response need to be estimated to determine the response statistics. The lognormal distribution can be fitted to the generic response parameter D (i.e., the extreme values $\psi_{v_d}$, $\psi_{v_p}$) by estimating the sample geometric mean, GM(D), and the sample lognormal standard deviation, or dispersion β(D) defined as follows:

$$GM\ (D) = \sqrt[N]{d_1 \cdot \ldots \cdot d_N}$$

$$\beta\ (D) = \sqrt{\frac{(ln\ (d_1) - \ln[GM\ (D)])^2 + \cdots + (\ln(d_N) - \ln[GM\ (D)])^2}{N-1}}$$

Where $d_i$ denotes the i-th sample value of D, and N is the total number of samples. The sample geometric mean is an estimator of the median of the response and its logarithm coincides with the lognormal sample mean $\mu_{ln}\ (D)$. Under the lognormality assumption, the k-th percentile of the generic response parameter D can be expressed in function of the geometric mean and of the dispersion as:

$$d_k = GM(D) \cdot \exp[f(k) \cdot \beta(D)]$$

where $f(k)$ is a function assuming the values $f(50) = 0$, $f(84) = 1$ and $f(16) = -1$ [37].

| Earthquake | Date | Magn. | Site | Epic. Dist. (km) | Comp. | PGA(g) | PGV (m/s) | PGA(g)/PGV | Soil |
|---|---|---|---|---|---|---|---|---|---|
| Parkfield California | June 27 1966 | 5,6 | Temblor No. 2 | 7 | N65W | 0,269 | 0,145 | 1,86 | Rock |
| Parkfield California | June 27 1966 | 5,6 | Cholame, Shandon No. 5 | 5 | N85W | 0,434 | 0,255 | 1,7 | Rock |
| San Francisco California | Mar. 22 1957 | 5,25 | Golden Gate Park | 11 | S80E | 0,105 | 0,046 | 2,28 | Rock |
| San Francisco California | Mar. 22 1957 | 5,25 | State Bldg., S.F. | 17 | S09E | 0,085 | 0,051 | 1,67 | Stiff Soil |
| Helena Montana | Oct. 31 1935 | 6 | Carroll College | 8 | N00E | 0,146 | 0,072 | 2,03 | Rock |
| Lytle Creek | Sep. 12 1970 | 5,4 | Wrightwood, California | 15 | S25W | 0,198 | 0,096 | 2,06 | Rock |
| Oroville California | Aug. 1 1975 | 5,7 | Seismogr. StationOroville | 13 | N53W | 0,084 | 0,044 | 1,91 | Rock |
| San Fernando California | Feb. 9 1971 | 6,4 | Pacomia Dam | 4 | S74W | 1,075 | 0,577 | 1,86 | Rock |
| San Fernando California | Feb. 9 1971 | 6,4 | Lake Hughes,Station 4 | 26 | S21W | 0,146 | 0,085 | 1,72 | Rock |
| NahanniN.W.T., Canada | Dec. 23 1985 | 6,9 | Site 1, Iverson | 7,5 | LONG | 1,101 | 0,462 | 2,38 | Rock |
| Central Honshu Japan | Feb. 26 1971 | 5,5 | Yoneyama Bridge | 27 | TRANS | 0,151 | 0,059 | 2,56 | Stiff Soil |
| Near E. Coast of Honshu Japan | May. 11 1972 | 5,8 | Kushiro CentralWharf | 33 | N00E | 0,146 | 0,06 | 2,43 | Stiff Soil |
| Honshu Japan | Apr. 5 1966 | 5,4 | Hoshina–A | 4 | N00E | 0,27 | 0,111 | 2,43 | Stiff Soil |
| Monte Negro Yugoslavia | Apr. 9 1979 | 5,4 | Albatros Hotel,Ulcinj | 12,5 | N00E | 0,042 | 0,016 | 2,63 | Rock |
| Banja Luka Yugoslavia | Aug. 13 1981 | 6,1 | Seism. Station, Banja Luka | 8,5 | N90W | 0,074 | 0,032 | 2,31 | Rock |

Table 1-Subset of far field records corresponding to high PGA/PGV values [PGA(g)/PGV>1.2].

| Earthquake | Date | Magn. | Site | Epic. Dist. (km) | Comp. | PGA(g) | PGV (m/s) | PGA(g)/PGV | Soil |
|---|---|---|---|---|---|---|---|---|---|
| Imperial Valley California | May 18 1940 | 6,6 | El Centro | 8 | S00E | 0,348 | 0,334 | 1,04 | Stiff Soil |
| Kern County California | July 21 1952 | 7,6 | Taft Lincoln School Tunnel | 56 | S69E | 0,179 | 0,177 | 1,01 | Rock |
| Kern County California | July 21 1952 | 7,6 | Taft Lincoln School Tunnel | 56 | N21E | 0,156 | 0,157 | 0,99 | Rock |
| Borrego Mtn. California | April 8 1968 | 6,5 | San Onofre SCE Power Plant | 122 | N57W | 0,046 | 0,042 | 1,1 | Stiff Soil |
| Borrego Mtn. California | April 8 1968 | 6,5 | San Onofre SCE Power Plant | 122 | N33E | 0,041 | 0,037 | 1,11 | Stiff Soil |
| San Fernando California | Feb. 9 1971 | 6,4 | 3838 Lankershim Blvd., L.A. | 24 | S90W | 0,15 | 0,149 | 1,01 | Rock |
| San Fernando California | Feb. 9 1971 | 6,4 | Hollywood Storage P.E. Lot, L.A. | 35 | N90E | 0,211 | 0,211 | 1 | Stiff Soil |
| San Fernando California | Feb. 9 1971 | 6,4 | 3407 6$^{th}$ Street, L.A. | 39 | N90E | 0,165 | 0,166 | 0,99 | Stiff Soil |
| San Fernando California | Feb. 9 1971 | 6,4 | Griffith Park Observatory, L.A. | 31 | S00W | 0,18 | 0,205 | 0,88 | Rock |
| San Fernando California | Feb. 9 1971 | 6,4 | 234 Figueroa St., L.A. | 41 | N37E | 0,199 | 0,167 | 1,19 | Stiff Soil |
| Near East Coast of Honshu,Japan | Nov. 16 1974 | 6,1 | Kashima Harbor Works | 38 | N00E | 0,07 | 0,072 | 0,97 | Stiff Soil |
| Near East Coast of Honshu,Japan | Aug. 2 1971 | 7 | Kushiro Central Wharf | 196 | N90E | 0,078 | 0,068 | 1,15 | Stiff Soil |
| Monte Negro Yugoslavia | Apr. 15 1979 | 7 | Albatros Hotel, Ulcinj | 17 | N00E | 0,171 | 0,194 | 0,88 | Rock |
| Mexico Earthq. | Sept. 19 1985 | 8,1 | El Suchil, Guerrero Array | 230 | S00E | 0,105 | 0,116 | 0,91 | Rock |
| Mexico Earthq. | Sept. 19 1985 | 8,1 | La Villita, Guerrero Array | 44 | N90E | 0,123 | 0,105 | 1,17 | Rock |

Table 2-Subset of far field records corresponding to high PGA/PGV values [0.8<PGA(g)/PGV<1.2].

| Earthquake | Date | Magn. | Site | Epic. Dist. (km) | Comp. | PGA(g) | PGV (m/s) | PGA(g)/PGV | Soil |
|---|---|---|---|---|---|---|---|---|---|
| Long Beach California | Mar. 10 1933 | 6,3 | Subway Terminal, L.A. | 59 | N51W | 0,097 | 0,237 | 0,41 | Rock |
| Long Beach California | Mar. 10 1933 | 6,3 | Subway Terminal, .A. | 59 | N39E | 0,064 | 0,173 | 0,37 | Rock |
| Lower Calif. | Dec. 30 1934 | 6,5 | El Centro | 58 | S00W | 0,16 | 0,209 | 0,77 | Stiff Soil |
| San Fernando California | Feb. 9 1971 | 6,4 | 2500 Wilshire Blvd., L.A. | 40 | N61W | 0,101 | 0,193 | 0,52 | Stiff Soil |
| San Fernando California | Feb. 9 1971 | 6,4 | 3550 Wilshire Blvd., L.A. | 39 | WEST | 0,132 | 0,216 | 0,61 | Stiff Soil |
| San Fernando California | Feb. 9 1971 | 6,4 | 222 Figueroa St., L.A. | 41 | S37W | 0,129 | 0,186 | 0,69 | Stiff Soil |
| San Fernando California | Feb. 9 1971 | 6,4 | 3470 WilshireBlvd., L.A. | 39 | S90W | 0,114 | 0,186 | 0,61 | Stiff Soil |
| San Fernando California | Feb. 9 1971 | 6,4 | 4680 WilshireBlvd., L.A. | 38 | N15E | 0,117 | 0,215 | 0,54 | Stiff Soil |
| San Fernando California | Feb. 9 1971 | 6,4 | 445 Figueroa St., L.A. | 41 | S38W | 0,119 | 0,173 | 0,69 | Rock |
| San Fernando California | Feb. 9 1971 | 6,4 | Hollywood Storage L.A. | 32 | S00W | 0,106 | 0,17 | 0,62 | Stiff Soil |
| Near E. Coast of Honshu, Japan | May 16 1968 | 7,9 | Muroran Harbor | 290 | N00E | 0,226 | 0,334 | 0,68 | Stiff Soil |
| Near E. Coast of Honshu, Japan | June 17 1973 | 7,4 | Kushiro Central Wharf | 112 | N00E | 0,205 | 0,275 | 0,75 | Stiff Soil |
| Mexico Earthq. | Sep. 19 1985 | 8,1 | Zihuatenejo, Guerrero Array | 135 | S00E | 0,103 | 0,159 | 0,65 | Rock |
| Mexico Earthq. | Sep. 19 1985 | 8,1 | Teacalco, Cuerrero Array | 333 | N00E | 0,052 | 0,074 | 0,7 | Rock |
| Mexico Earthq. | Sep. 19 1985 | 8,1 | Mesa VibradoraC.U., Mexico City | 379 | N90W | 0,04 | 0,11 | 0,36 | Rock |

Table 3-Subset of far field records corresponding to high PGA/PGV values [PGA(g)/PGV<0.8].

| Earthquake | Year | Magn. | Site | Closest dist. (km) | Comp. | PGA(g) | PGV (m/s) | PGA(g)/PGV | Soil type |
|---|---|---|---|---|---|---|---|---|---|
| Imperial Valley-06 | 1979 | 6,53 | Subway Terminal, L.A. | 7,31 | SN | 0,180 | 0,545 | 0,33 | C |
| Imperial Valley-06 | 1979 | 6,53 | Subway Terminal, .A. | 0,07 | SN | 0,378 | 1,150 | 0,33 | C |
| Imperial Valley-06 | 1979 | 6,53 | El Centro | 7,05 | SN | 0,357 | 0,779 | 0,46 | C |
| Imperial Valley-06 | 1979 | 6,53 | El Centro | 3,95 | SN | 0,375 | 0,915 | 0,41 | C |
| Imperial Valley-06 | 1979 | 6,53 | El Centro | 1,35 | SN | 0,442 | 1,119 | 0,39 | C |
| Imperial Valley-06 | 1979 | 6,53 | El Centro | 0,56 | SN | 0,462 | 1,088 | 0,42 | C |
| Imperial Valley-06 | 1979 | 6,53 | El Centro | 3,86 | SN | 0,468 | 0,486 | 0,96 | C |
| Imperial Valley-06 | 1979 | 6,53 | El Centro | 5,09 | SN | 0,417 | 0,596 | 0,70 | C |
| Morgan Hill | 1984 | 6,19 | El Centro | 0,53 | SN | 0,814 | 0,623 | 1,31 | B |
| Loma Prieta | 1989 | 6,93 | El Centro | 9,96 | SN | 0,294 | 0,308 | 0,95 | B |
| Loma Prieta | 1989 | 6,93 | El Centro | 3,88 | SN | 0,944 | 0,970 | 0,97 | B |
| Landers | 1992 | 7,28 | El Centro | 2,19 | SN | 0,704 | 1,406 | 0,50 | B |
| Landers | 1992 | 7,28 | El Centro | 23,62 | SN | 0,236 | 0,566 | 0,42 | C |
| Northridge-01 | 1994 | 6,69 | El Centro | 5,43 | SN | 0,617 | 0,674 | 0,92 | B |
| Northridge-01 | 1994 | 6,69 | El Centro | 5,43 | SN | 0,518 | 0,674 | 0,77 | B |
| Northridge-01 | 1994 | 6,69 | El Centro | 5,92 | SN | 0,724 | 1,203 | 0,60 | C |
| Northridge-01 | 1994 | 6,69 | El Centro | 5,48 | SN | 0,426 | 0,878 | 0,49 | C |
| Northridge-01 | 1994 | 6,69 | El Centro | 6,5 | SN | 0,870 | 1,672 | 0,52 | C |
| Northridge-01 | 1994 | 6,69 | El Centro | 5,35 | SN | 0,594 | 1,303 | 0,46 | C |
| Northridge-01 | 1994 | 6,69 | El Centro | 5,19 | SN | 0,828 | 1,136 | 0,73 | B |
| Northridge-01 | 1994 | 6,69 | El Centro | 5,3 | SN | 0,733 | 1,227 | 0,60 | B |
| Kobe, Japan | 1995 | 6,9 | El Centro | 0,96 | SN | 0,854 | 0,963 | 0,89 | C |
| Kobe, Japan | 1995 | 6,9 | El Centro | 0,27 | SN | 0,645 | 0,726 | 0,89 | C |
| Kocaeli, Turkey | 1999 | 7,51 | El Centro | 10,92 | SN | 0,241 | 0,512 | 0,47 | B |
| Chi-Chi, Taiwan | 1999 | 7,62 | El Centro | 3,14 | SN | 0,664 | 0,777 | 0,85 | B |
| Chi-Chi, Taiwan | 1999 | 7,62 | El Centro | 9,96 | SN | 0,383 | 0,753 | 0,51 | C |
| Chi-Chi, Taiwan | 1999 | 7,62 | El Centro | 3,78 | SN | 0,286 | 0,461 | 0,62 | B |
| Chi-Chi, Taiwan | 1999 | 7,62 | El Centro | 0,66 | SN | 0,375 | 1,655 | 0,23 | B |
| Chi-Chi, Taiwan | 1999 | 7,62 | El Centro | 5,97 | SN | 0,224 | 0,409 | 0,55 | B |
| Chi-Chi, Taiwan | 1999 | 7,62 | El Centro | 5,3 | SN | 0,157 | 0,604 | 0,26 | B |
| Chi-Chi, Taiwan | 1999 | 7,62 | 3470 WilshireBlvd., L.A. | 0,32 | SN | 0,564 | 1,846 | 0,31 | B |
| Chi-Chi, Taiwan | 1999 | 7,62 | 4680 WilshireBlvd., L.A. | 0,91 | SN | 0,331 | 0,886 | 0,37 | B |
| Chi-Chi, Taiwan | 1999 | 7,62 | 445 Figueroa St., L.A. | 2,76 | SN | 0,310 | 0,678 | 0,46 | B |
| Chi-Chi, Taiwan | 1999 | 7,62 | Hollywood Storage L.A. | 5,18 | SN | 0,235 | 0,578 | 0,41 | B |
| Chi-Chi, Taiwan | 1999 | 7,62 | Muroran Harbor | 7 | SN | 0,127 | 0,437 | 0,29 | B |
| Chi-Chi, Taiwan | 1999 | 7,62 | Kushiro Central Wharf | 2,13 | SN | 0,212 | 0,684 | 0,31 | C |
| Chi-Chi, Taiwan | 1999 | 7,62 | Zihuatenejo, Guerrero Array | 1,51 | SN | 0,295 | 1,090 | 0,27 | B |
| Chi-Chi, Taiwan | 1999 | 7,62 | Teacalco, Cuerrero Array | 6,1 | SN | 0,133 | 0,621 | 0,21 | B |
| Chi-Chi, Taiwan | 1999 | 7,62 | Teacalco, Cuerrero Array | 9,35 | SN | 0,224 | 0,424 | 0,53 | B |
| Chi-Chi, Taiwan | 1999 | 7,62 | Mesa VibradoraC.U., Mexico City | 9,96 | SN | 0,303 | 0,676 | 0,45 | C |

Table 4-Near fault records

# 12. RESULTS

## 12.1 Results obtained for the FF record sets

This paragraph illustrates the results obtained for the far field record set. Figures from 71 to 78 show the statistics (*GM* and $\beta$ values) of the response parameters considered, obtained for the different values of the system parameters varying in the range of interest. In particular, figures 3 and 4 report the results concerning the normalized pier displacement $\psi_{p,max}$ for the two values of $T_p$ (0.05 s and 0.2 s). Fig. 71 shows the variation with the system parameters of the geometric mean of the normalized substructure displacement $GM(\psi_{p,max})$. The results obtained for the different values of $T_p$ are reported in separate figures to better highlight the influence of this parameter on the substructure response. In general, it is observed that $GM(\psi_{p,max})$ decreases for increasing values both of $T_d/T_g$ and mass ratio $\Pi_\gamma$, for this latter one the dependency is stronger for lower values of $T_p$, whereas it first decreases and then increases for increasing values of $\Pi^*{}_\mu$. Thus, there exists a value of $\Pi^*{}_\mu$, which is denoting the optimal value that minimizes $GM(\psi_{p,max})$. This optimal value strongly depends on the values assumed by the system parameters, especially, on the $T_d/T_g$ ratio. The values of the dispersion, $\beta(\psi_{p,max})$, represented in fig. 76, are, in general, relatively high. In general, the dispersion decreases for increasing values of $\Pi^*{}_\mu$, remains almost constant for varying values of $T_d/T_g$ and slightly increases for increasing values of the mass ratio $\Pi_\gamma$. The existence of an optimal value of the friction coefficient has been pointed out in many studies on system isolated by single concave sliding bearings [21,34, 38-41] and it is the results of two counteracting effects that follow an increase of the friction coefficient. The first effect is the increase of isolator strength, with associated increasing of forces transferred to the substructure. The second effect is an increasing of energy dissipation and a reduction of the pier displacements ($\psi_{p,max}$).

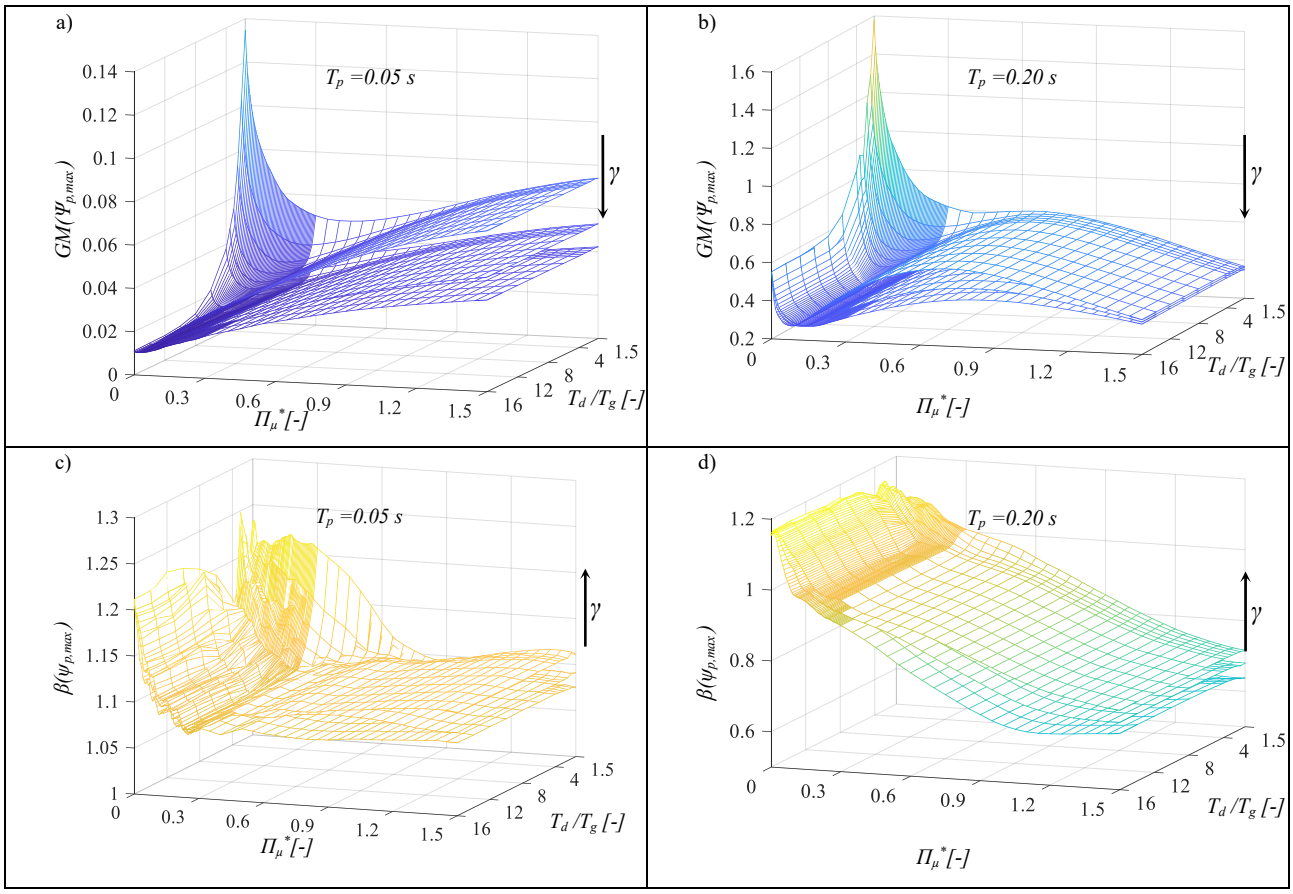


Figure 71-Non-dimensional displacement (a,b) and dispersion (c,d) of the pier cap, for far field records. The arrow denotes the increasing direction of γ=0.1-0.2.

Moreover, figures 73, 75 and 77 show the variation of the median values of the substructure displacement obtained by considering separately the three different subsets of far field records, characterized by different ranges of PGA/PGV values. It can be noted that, even if the trends observed for the different PGA/PGV ranges are very similar, the values oscillate in a range in the order of ten times. This justifies the high values of dispersion and may mean that PGA value is not the most suitable and efficient parameter as intensity measure for non-dimensioning of the pier cap displacement, however it is noteworthy how even if the median responses are different the optimal normalized friction value is the same independently to the record sets considered. Figure 83 shows the superposition curves of median responses for the all record sets in order to highlight that the minimum falls on the same normalized friction coefficient identifying an optimum value of this last. The example in fig. 83 is given for $T_d/T_g$ = 4, $\gamma$ = 0.15 and $T_p$ = 0.15 s, the optimum normalized friction coefficient results $\Pi^*_{\mu,opt}$=0.17.

As concern the normalized deck relative displacement $\psi_{d,max}$, generally, for increasing of $T_d/T_g$ values, $GM(\psi_{d,max})$ first increases until a peak and then decreases, by following a trend similar to the one of a displacement response spectrum of a s.d.o.f system with respect to the system vibration

period. Obviously, $GM(\psi_{d,max})$ decreases significantly as $\Pi^*_\mu$ increases. Furthermore, the values of $GM(\psi_{d,max})$ are only slightly influenced by $\Pi_\gamma$ and $T_p$.

It can be noted that the trends observed for the different PGA/PGV ranges are very close, or in other terms the median response obtained for the three records subsets for a given combination of $\Pi_\gamma$, $T_p$, and $T_d/T_g$ values are statistically not different. This confirms that the normalized response is not significantly affected by the record selection if $T_g$ is considered as ground motion parameter.

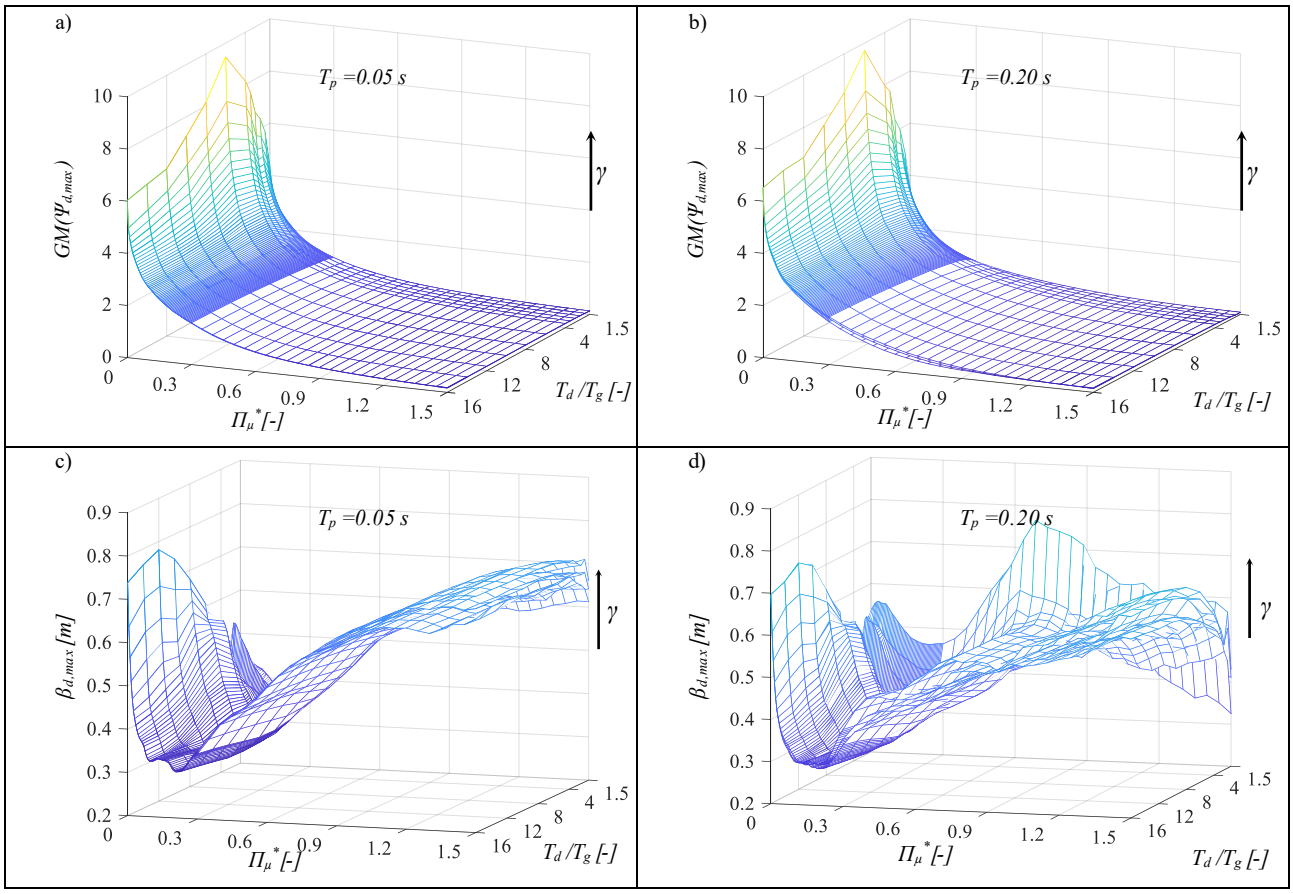


Figure 72-Non-dimensional relative displacement of the isolation level, for far field records. The arrow denotes the increasing direction of γ=0.1-0.2

The dispersion $\beta(\psi_{d,max})$ is in general quite low, in correspondence of the optimal values of the friction coefficient for $GM(\psi_{p,max})$ and increases moving far from these values.

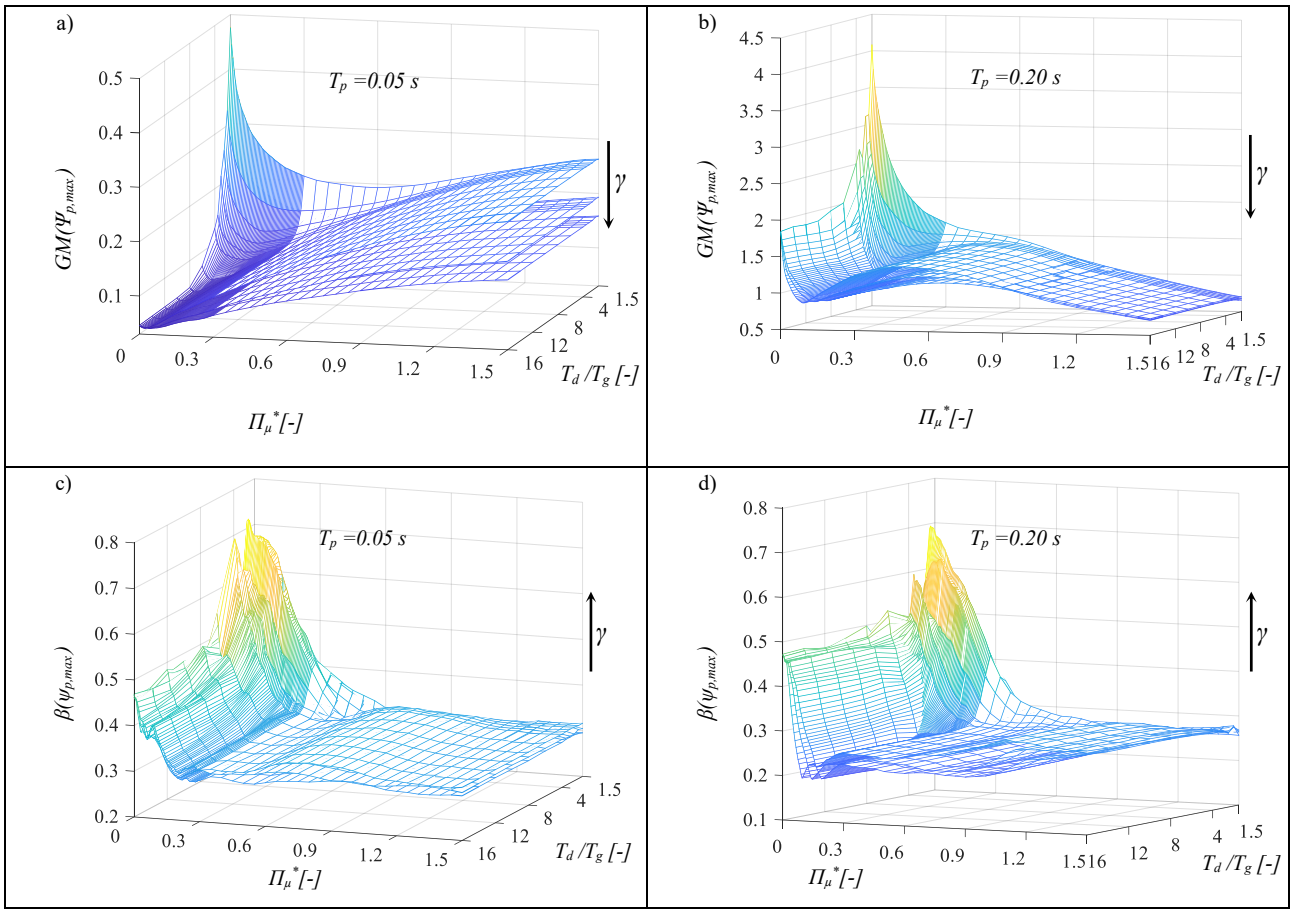


Figure 73-Non-dimensional displacement (a,b) and dispersion (c,d) of the pier cap, for far field records with high PGA/PGV ratios. The arrow denotes the increasing direction of γ=0.1-0.2.

## 12.2 Results obtained for the NF record sets

This paragraph illustrates the results obtained for the near fault record set. In particular, figs. 79 shows the statistics of the pier cap displacement (substructure) and figs. 80 shows the one of the isolator displacement (superstructure), for the different values of $T_p$, $\Pi_\gamma$ and $T_d/T_g$. The observed trends are very similar to those obtained for the far field records. This again confirms the importance of accounting for $T_d/T_g$ in evaluating the system performance and the fact that when $T_g$ is used as indicator of the frequency content of the seismic input, the normalized response does not depend significantly on other characteristics of the seismic input. For a given value of $T_p$, $\Pi_\gamma$ and $T_d/T_g$, the normalized median responses of both the isolation system and the substructure under far field ground motions are higher than the corresponding responses under the near fault ground motions.

This result is very interesting and only apparently contradicts the conclusion of other studies for which near fault records are more demanding for isolated systems than far field ones (e.g. [42, 43]).

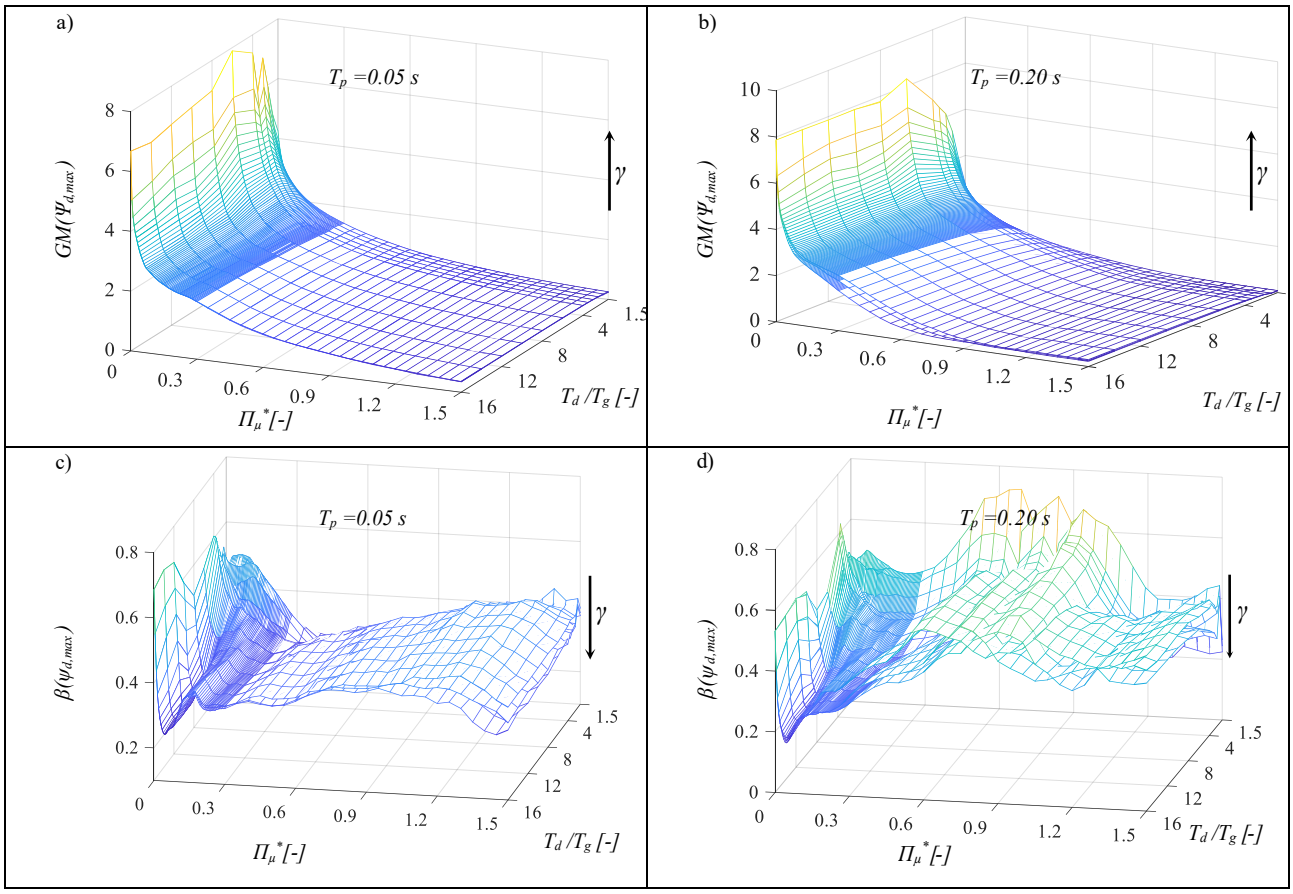


Figure 74-Non-dimensional relative displacement of the isolation level, for far field records with high PGA/PGV ratios. The arrow denotes the increasing direction of γ=0.1-0.2

In fact, NF records are more demanding for isolated systems because they are characterized by a higher energy content at low frequencies compared to FF records. However, this feature is already taken into account in this study by the parameter $T_d/T_g$. For the same $T_d/T_g$ value, FF records may induce higher displacement demands because, differently from the NF records, they are characterized by multiple cycles of large amplitudes rather than a single pulse. The work of Chopra and Chintanapakdee [44] has already demonstrated the importance of the number of large amplitude cycles on the maximum seismic response.

Moreover, the results reported in fig. 79 shows that, as in the case of FF records, there exists an optimal value of the normalized friction which minimizes the substructure median response.

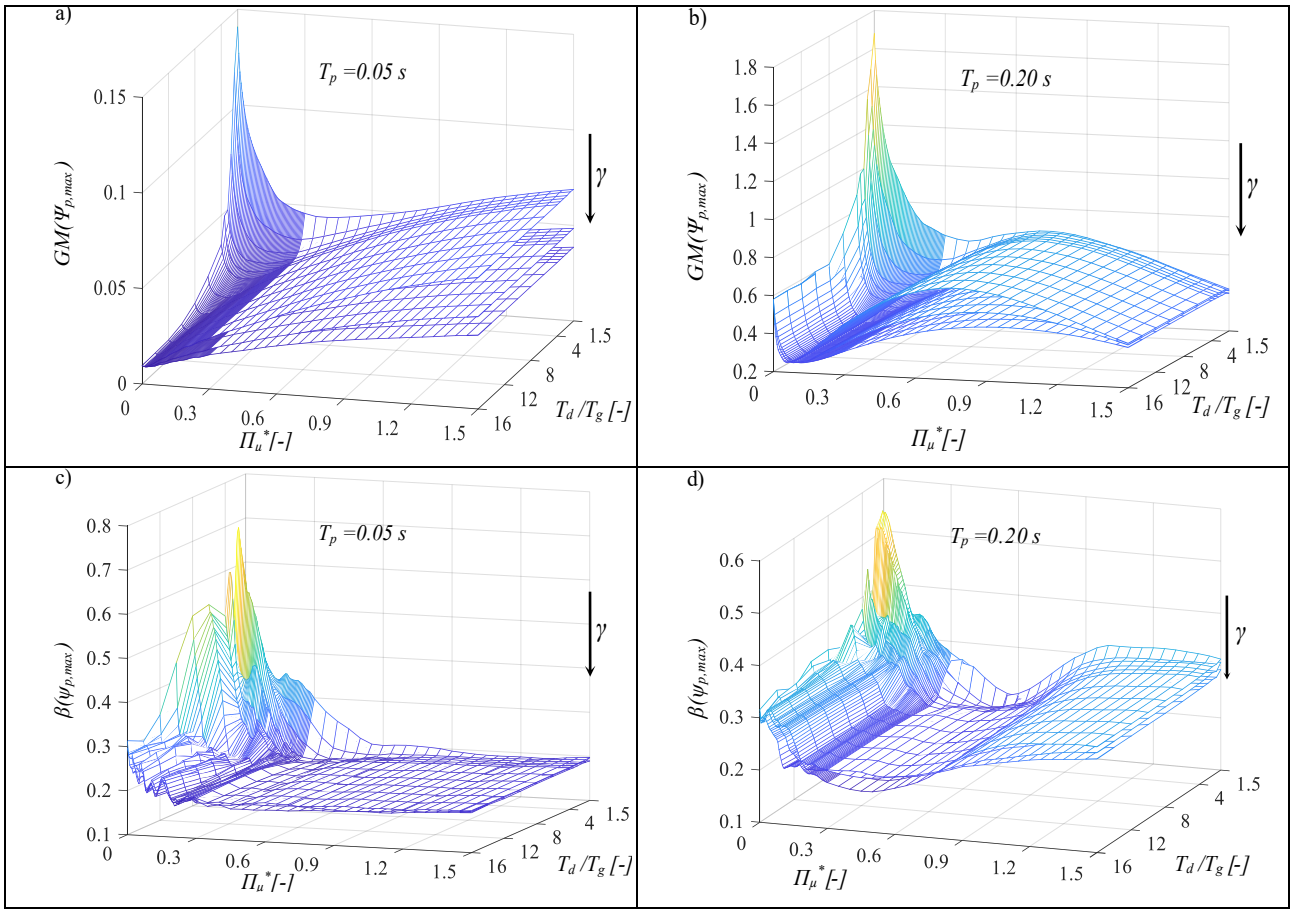


Figure 75-Non-dimensional displacement (a,b) and dispersion (c,d) of the pier cap, for far field records with intermediate PGA/PGV ratios. The arrow denotes the increasing direction of γ=0.1-0.2.

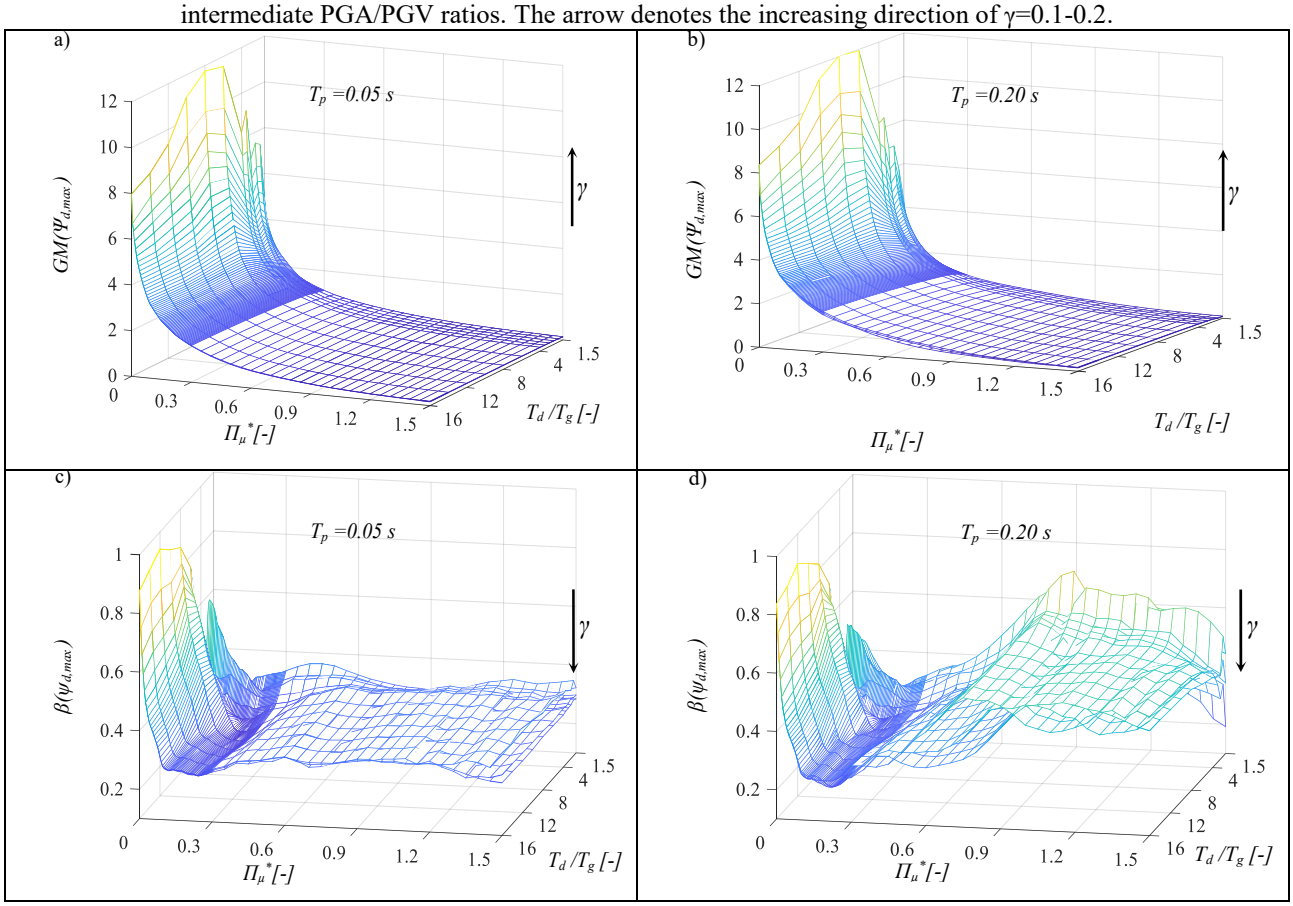


Figure 76-Non-dimensional relative displacement of the isolation level, for far field records with intermediate PGA/PGV ratios. The arrow denotes the increasing direction of γ =0.1-0.2

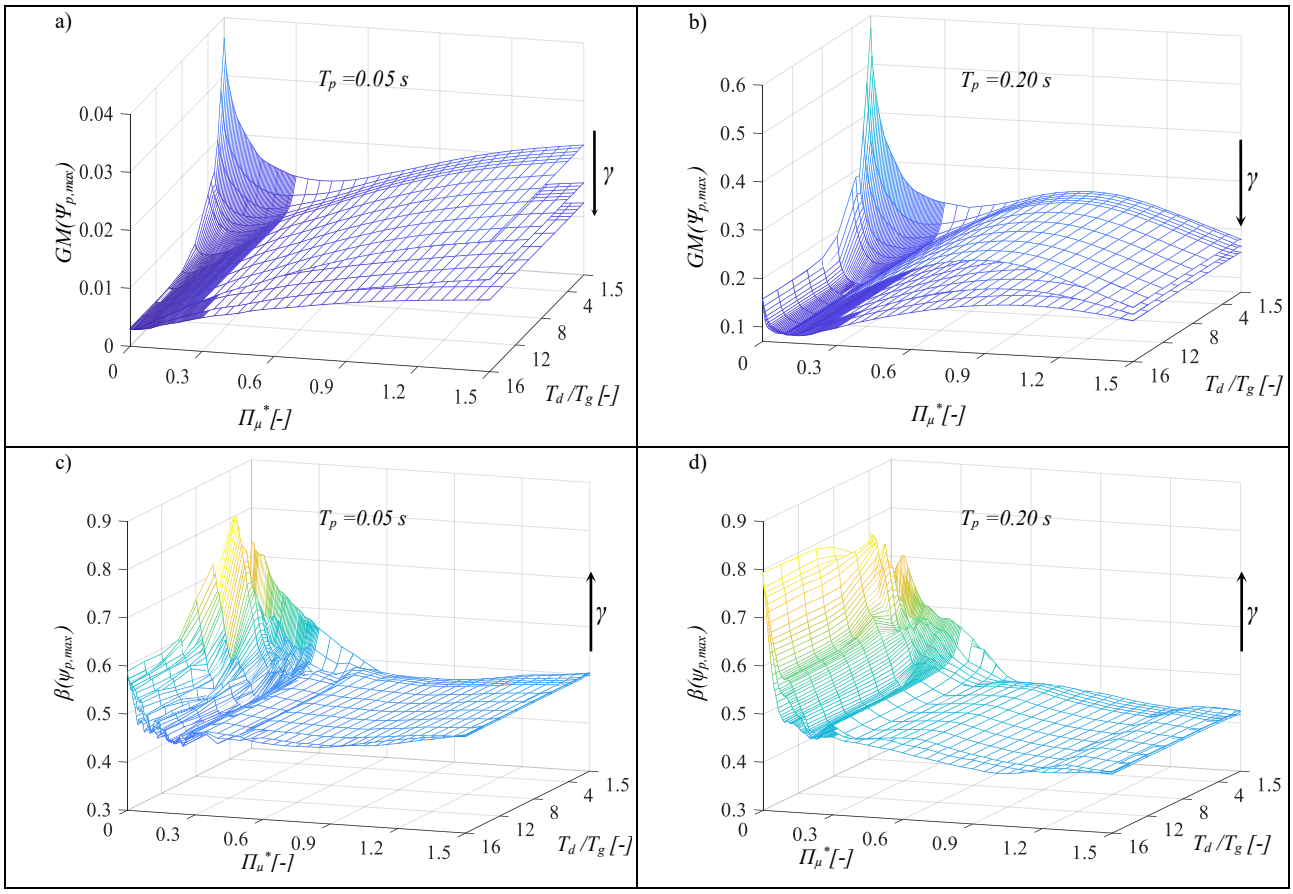


Figure 77-Non-dimensional displacement (a,b) and dispersion (c,d) of the pier cap, for far field records with low PGA/PGV ratios. The arrow denotes the increasing direction of γ=0.1-0.2.

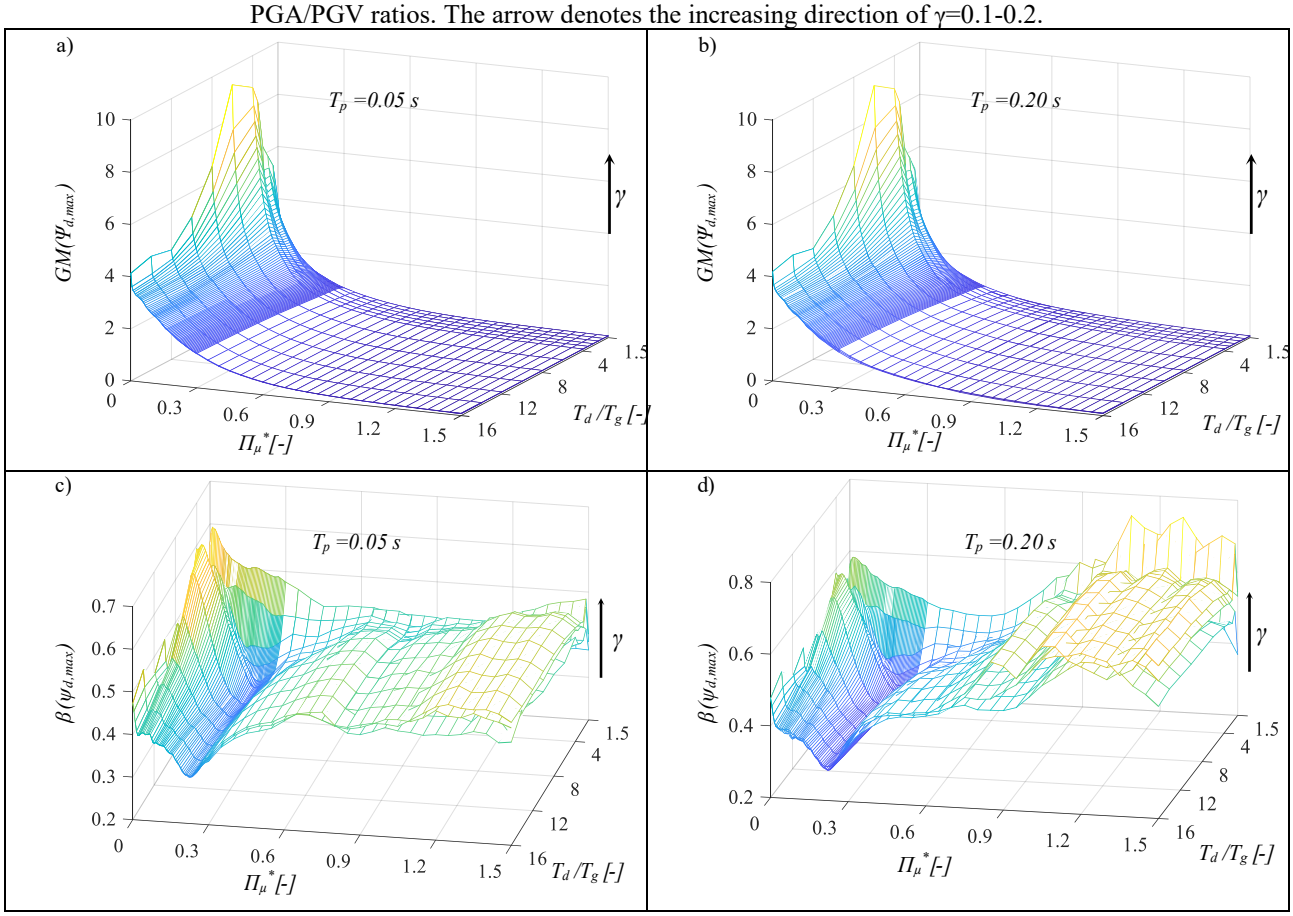


Figure 78-Non-dimensional relative displacement of the isolation level, for far field records with low PGA/PGV ratios. The arrow denotes the increasing direction of γ=0.1-0.2

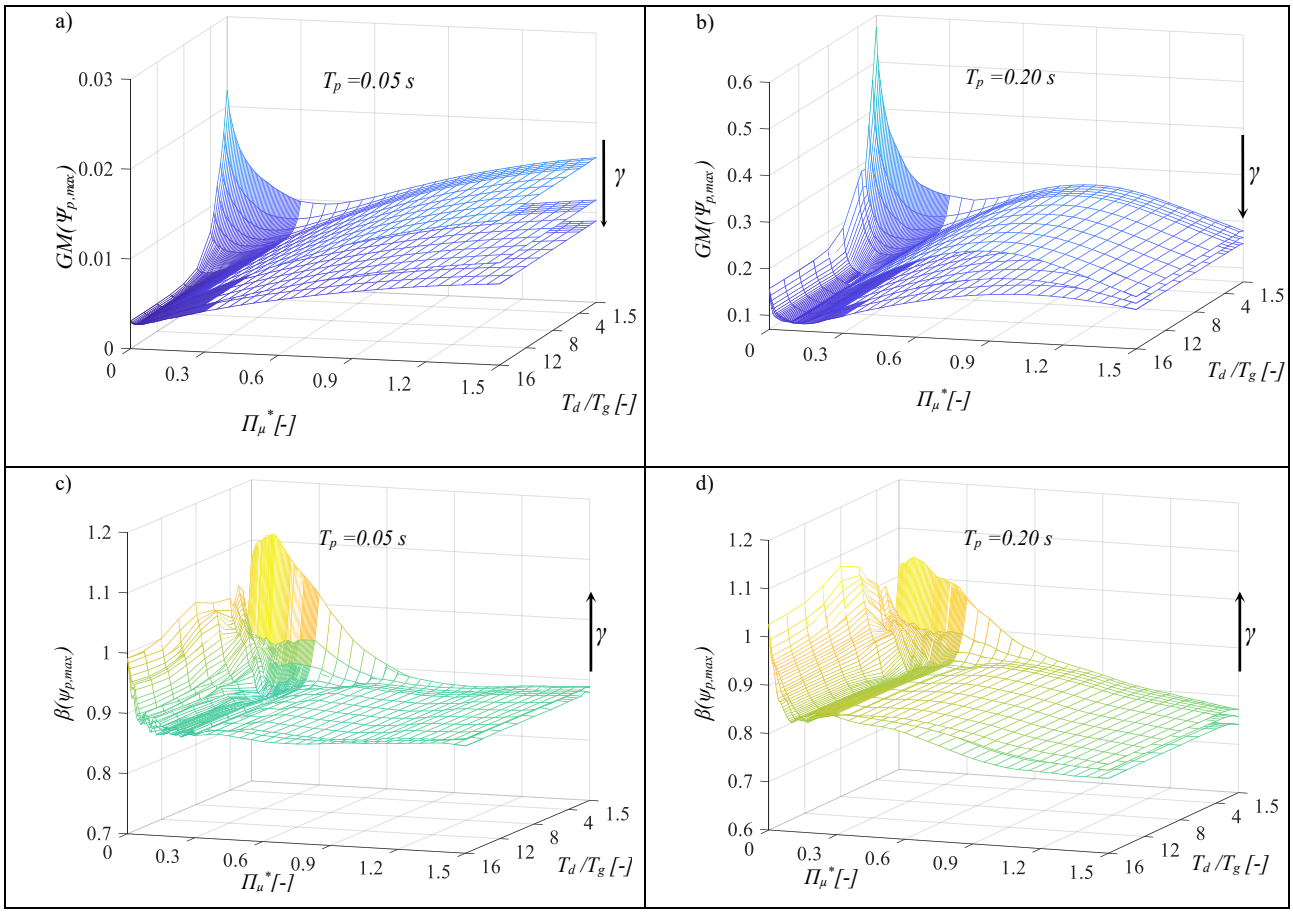


Figure 79-Non-dimensional displacement (a,b) and dispersion (c,d) of the pier cap, for near field records. The arrow denotes the increasing direction of γ=0.1-0.2.

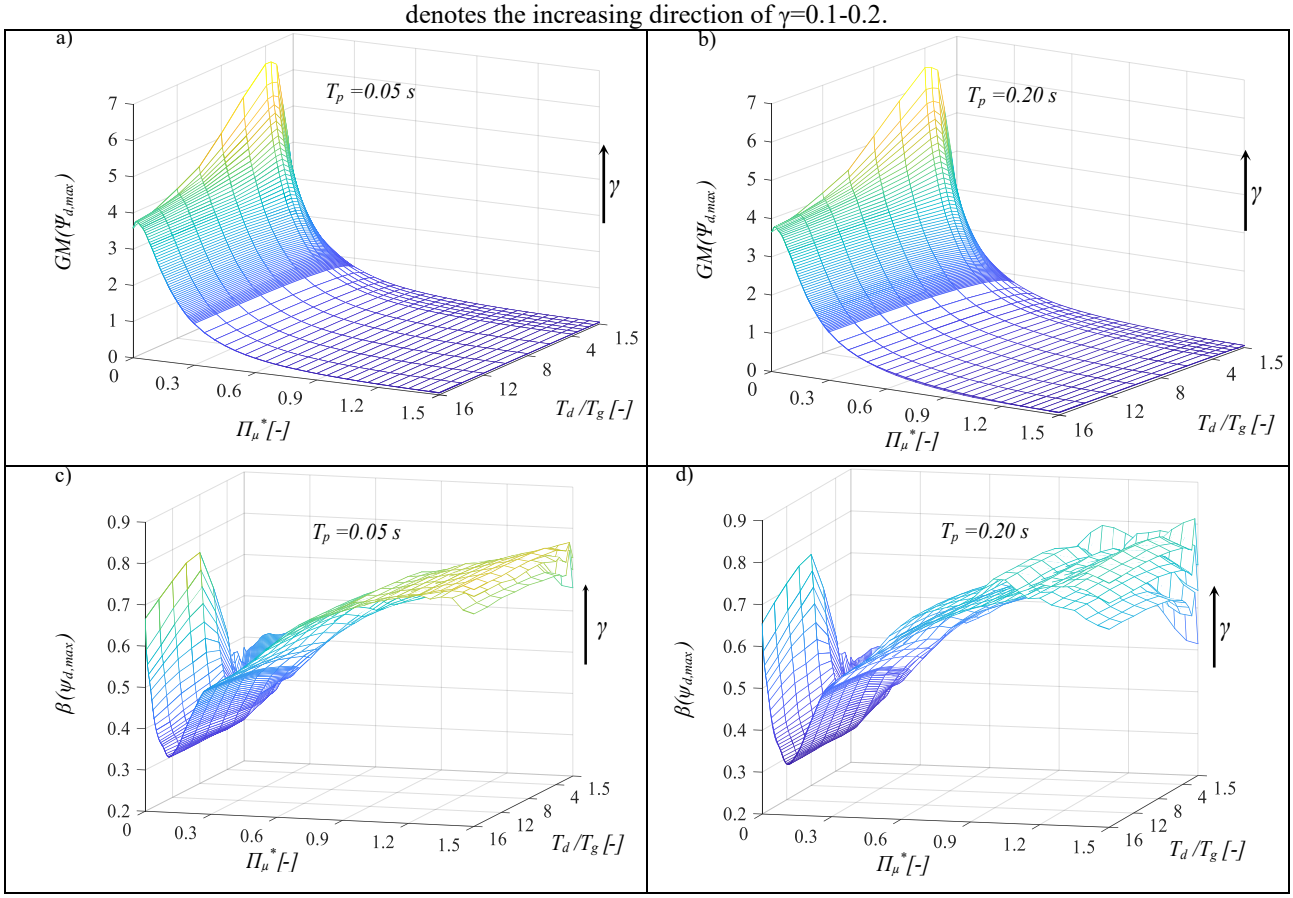


Figure 80-Non-dimensional relative displacement of the isolation level, for near fault records. The arrow denotes the increasing direction of γ=0.1-0.2

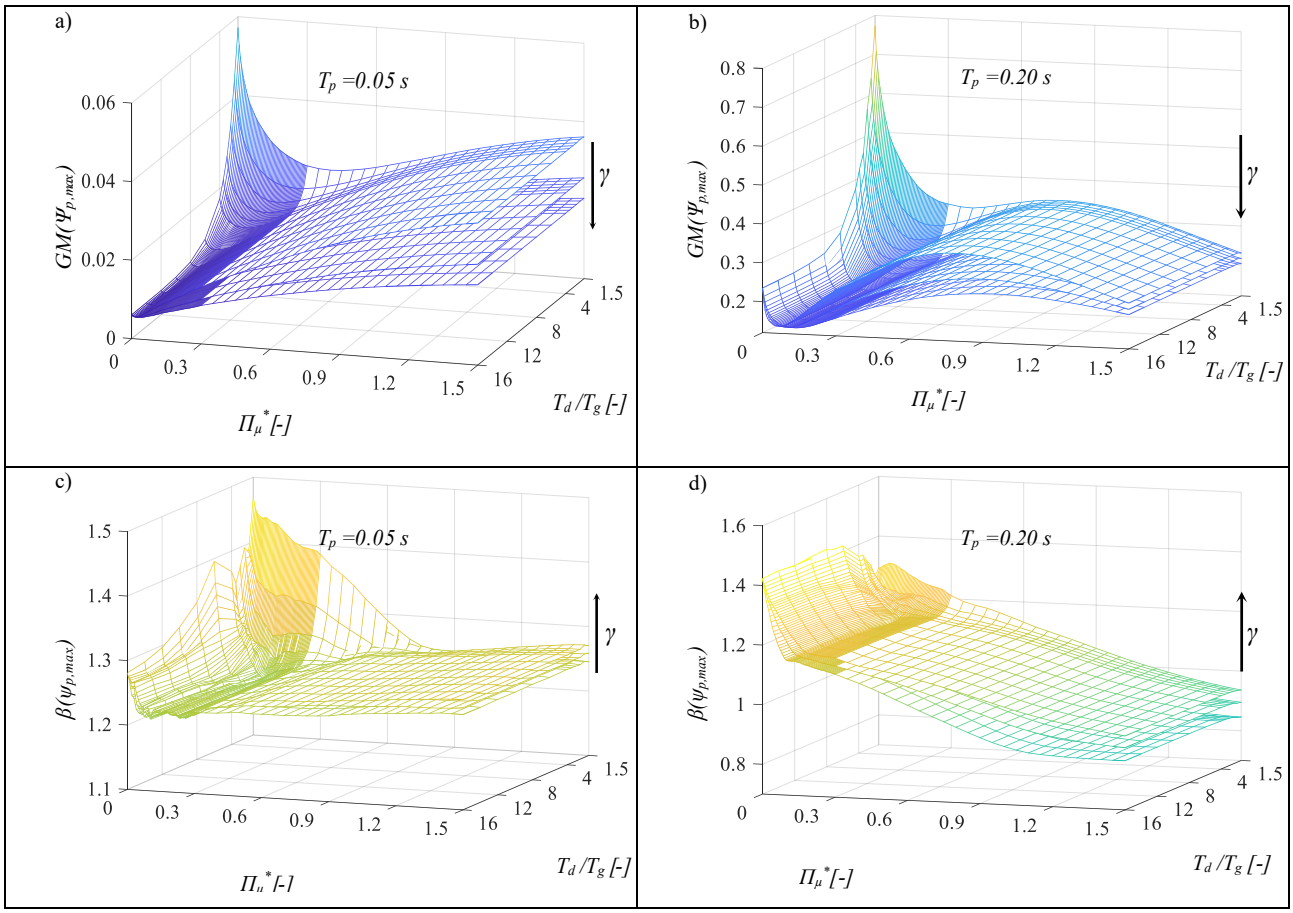


Figure 81-Non-dimensional displacement (a,b) and dispersion (c,d) of the pier cap, for both near fault and far field records. The arrow denotes the increasing direction of γ=0.1-0.2.

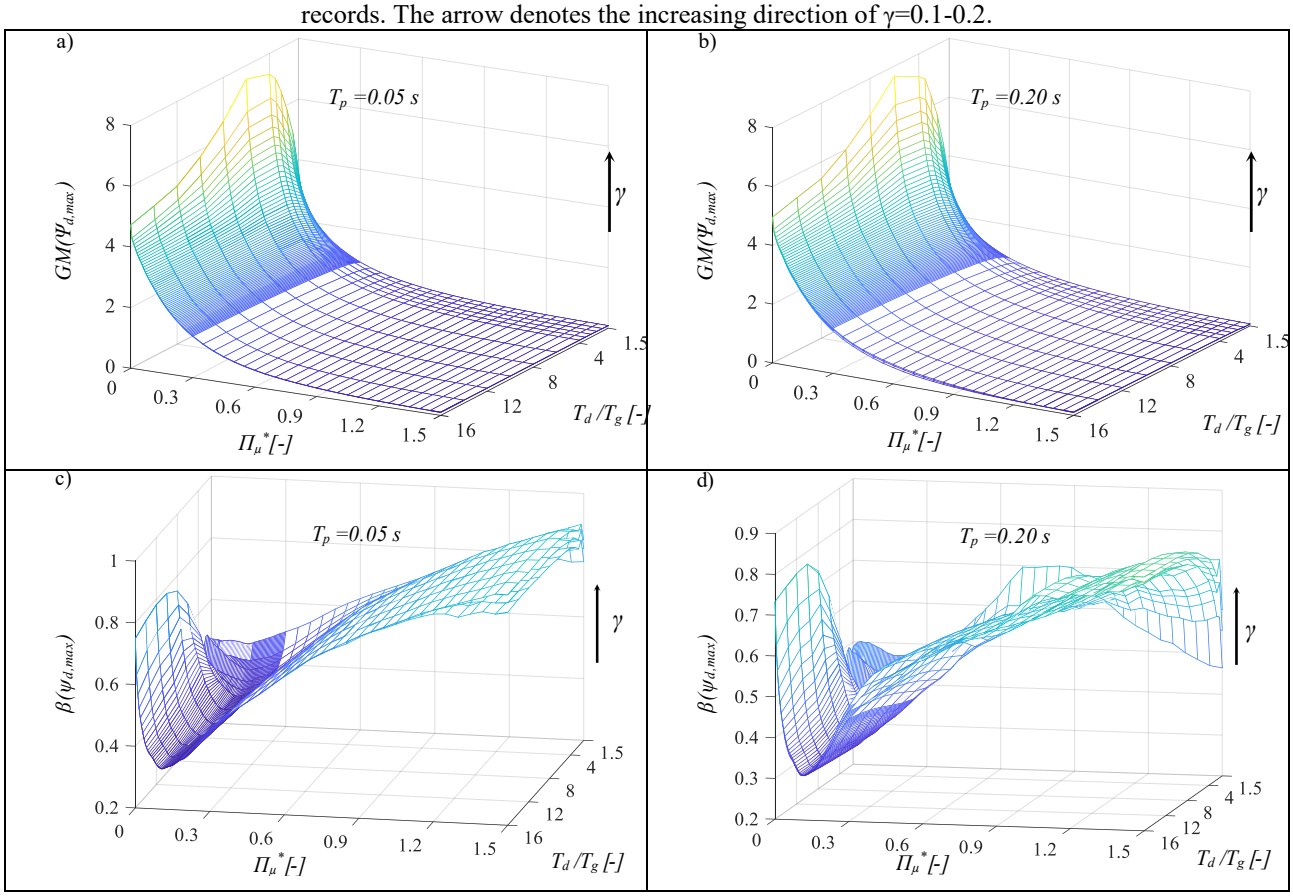


Figure 82-Non-dimensional relative displacement (a,b) and dispersion (c,d) of the isolation level, for both near fault and far field records. The arrow denotes the increasing direction of γ=0.1-0.2

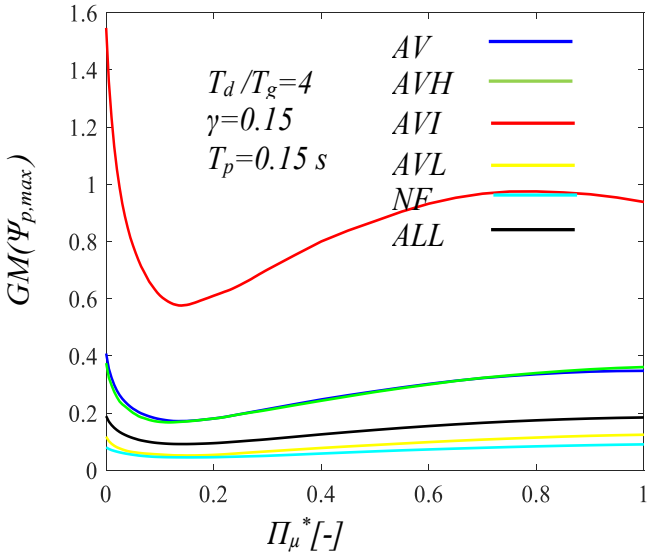


Fig. 83-Median response curves superposed for all record sets

## 12.3 Optimal sliding friction coefficient

The results reported in the previous paragraph in figs. 71-82 show that for each combination of the system properties (i.e., $\Pi_\gamma$, $T_d/T_g$, $T_p$) there exists an optimal value of the normalized sliding friction coefficient, $\Pi^*{}_{\mu,opt}$, such that the median (i.e., 50$^{th}$ percentile) normalized substructure displacement is minimized. Figs 84-89 show the variation of $\Pi^*{}_{\mu,opt}$ with these parameters for all seismic acceleration record sets.

In general, it is observed for all of record sets that, obviously, $\Pi^*{}_{\mu,opt}$ decreases significantly by increasing $T_d/T_g$. On the other hand, there is not a clear and significant trend of variation with $\Pi_\gamma$ and $T_p$, it means that it can be possible to consider the optimal values as independent from these two parameters.

As already discussed previously, the substructure displacement depends on the forces transmitted to the substructure, which in turn depend on both isolator displacement and the friction force. By increasing the friction, the displacement reduces, however the friction force increases. Thus, there is an optimum amount of friction minimizing the substructure response. The displacement reduction with $\Pi^*{}_\mu$ is more relevant for higher values of $T_d/T_g$ than for lower ones and it explains why the optimum friction value is lower for higher $T_d/T_g$ values. With regard to the dependency of the optimal friction on the type of records set considered, it is observed that the values of $\Pi^*{}_{\mu,opt}$ for all sets are very similar to each other, for $T_d/T_g$ values higher than 2 which are common in design practice.

Figs. 90-101 show the trend of the optimal friction coefficient $\Pi^*_{\mu,opt}$ that minimizes the 84th (figs. 90-95) and the 16th (figs. 96-101) percentiles of the substructure response under all record sets. The trends of variation of these percentiles are the same as the ones of the median responses (50th percentile).

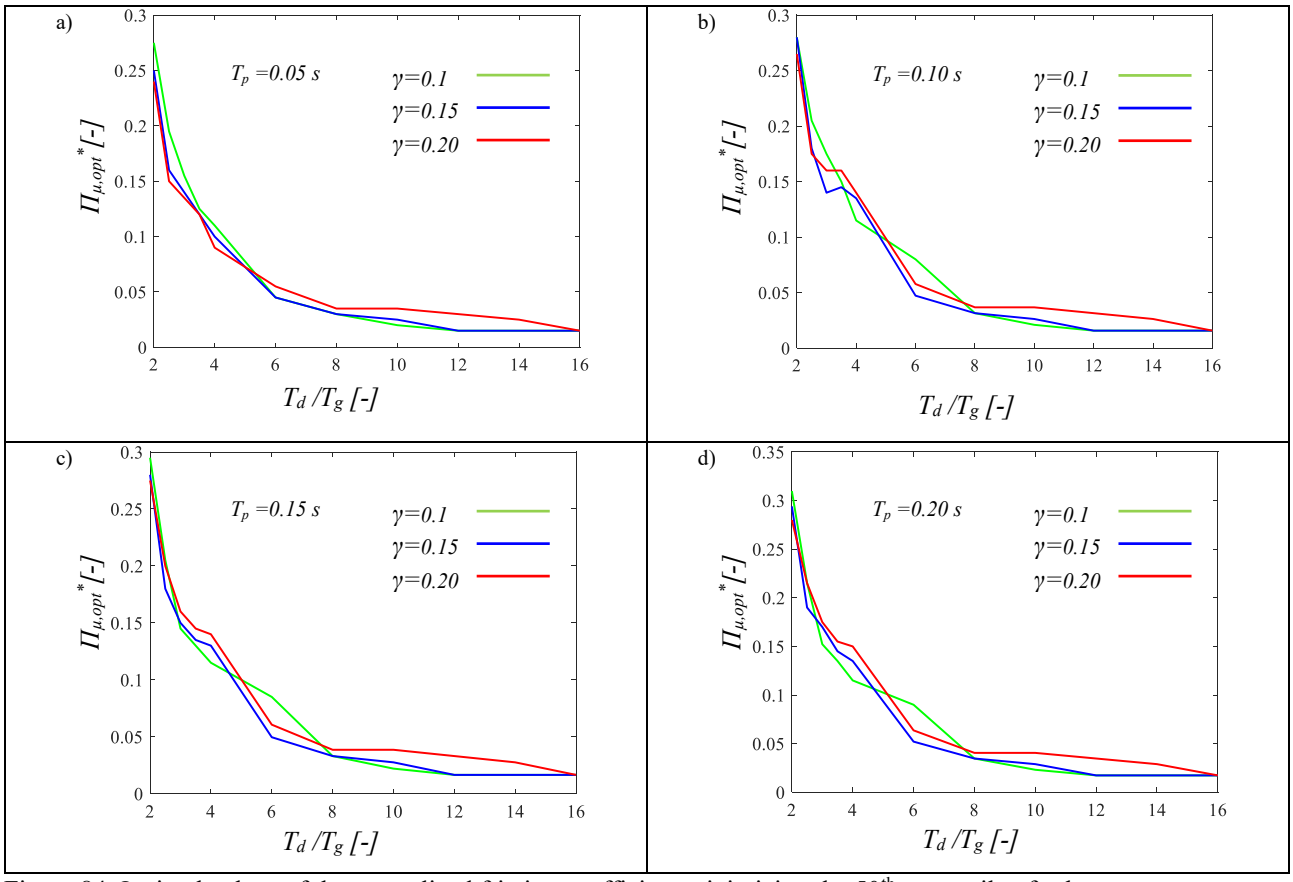


Figure 84-Optimal values of the normalized friction coefficient minimizing the 50$^{th}$ percentile of substructure response for fixed $T_p$ and varying γ, for far field records.

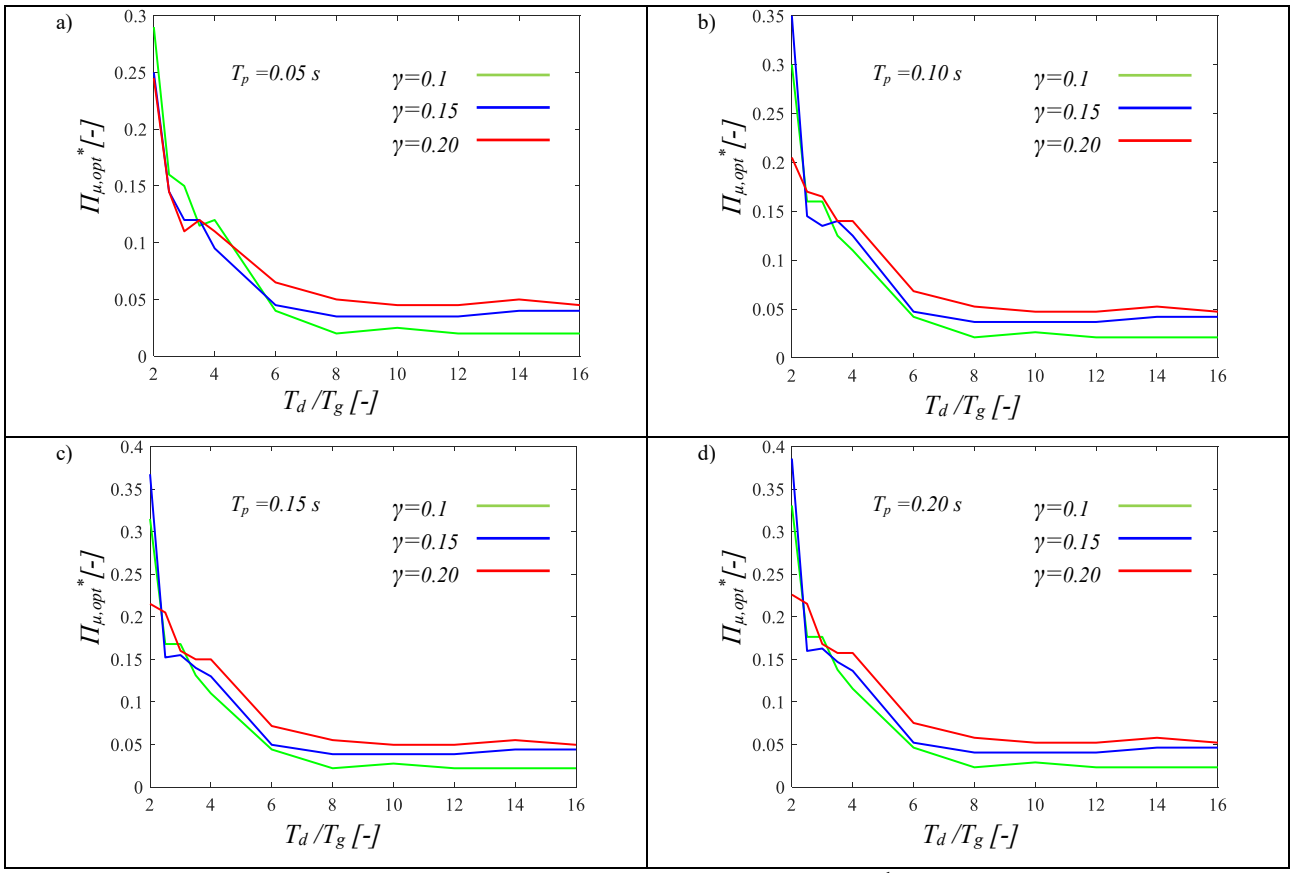


Figure 85-Optimal values of the normalized friction coefficient minimizing the 50th percentile of substructure response for fixed $T_p$ and varying γ, for far field records with high PGA/PGV ratios.

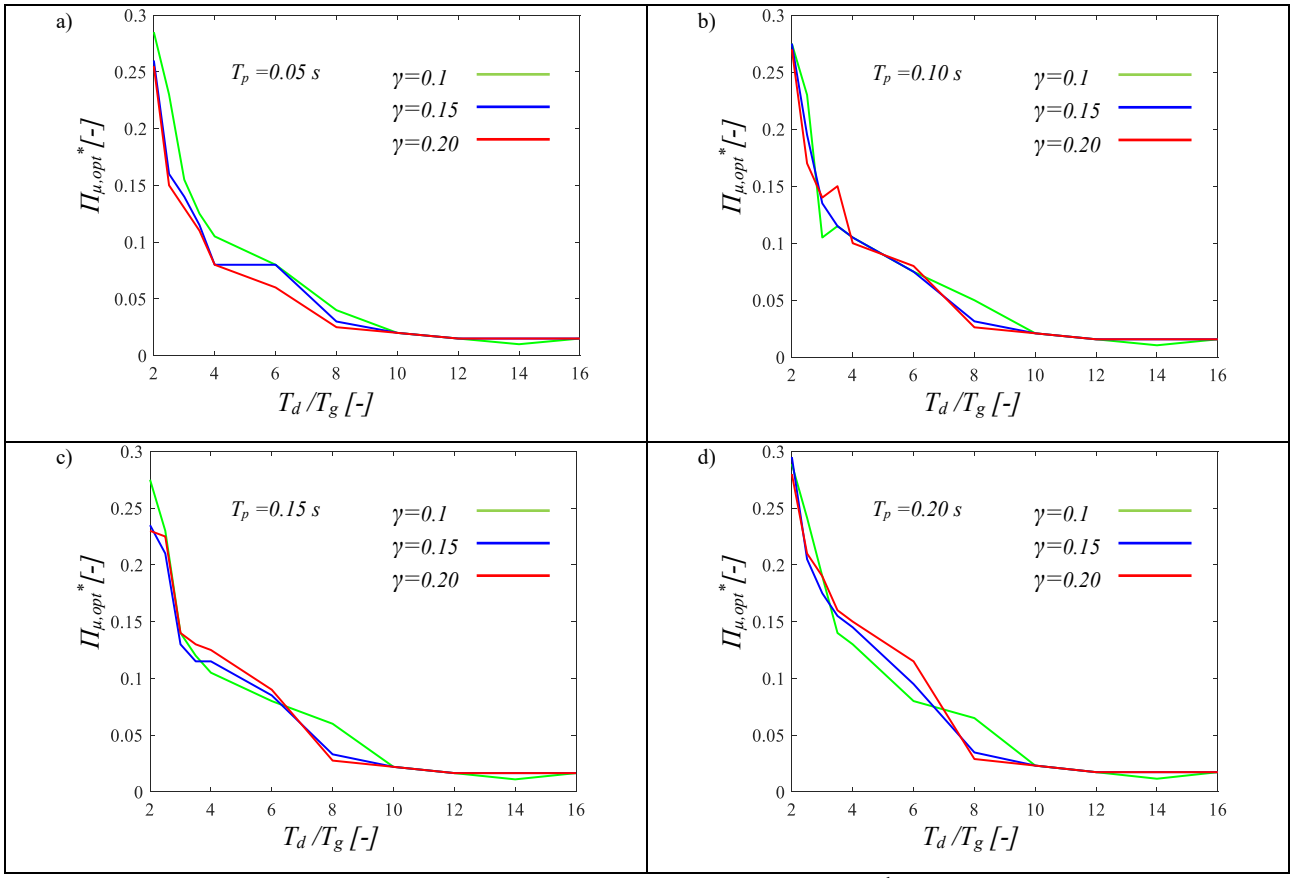


Figure 86-Optimal values of the normalized friction coefficient minimizing the 50th percentile of substructure response for fixed $T_p$ and varying γ, for far field records with intermediate PGA/PGV ratios.

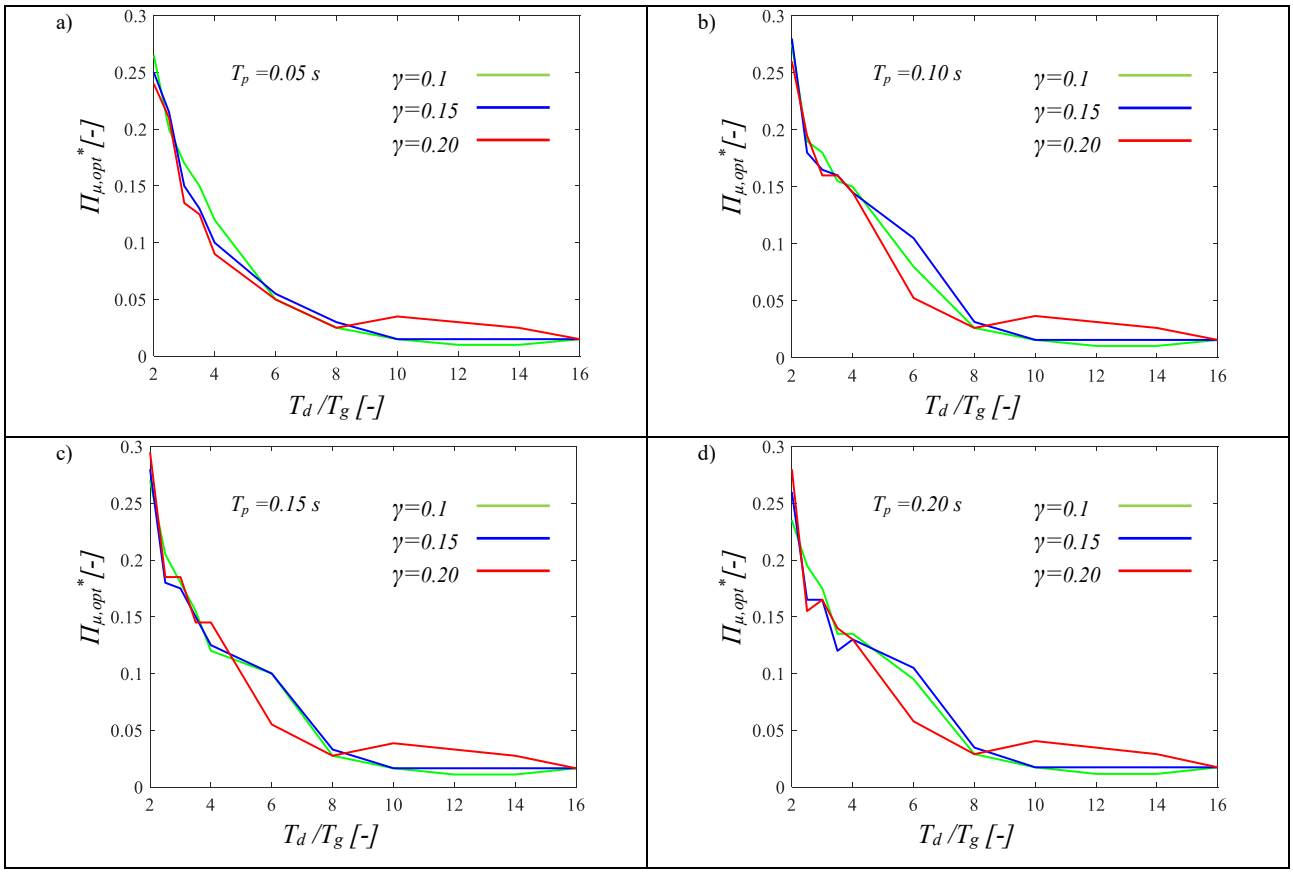


Figure 87-Optimal values of the normalized friction coefficient minimizing the 50$^{th}$ percentile of substructure response for fixed $T_p$ and varying γ, for far field records with low PGA/PGV ratios.

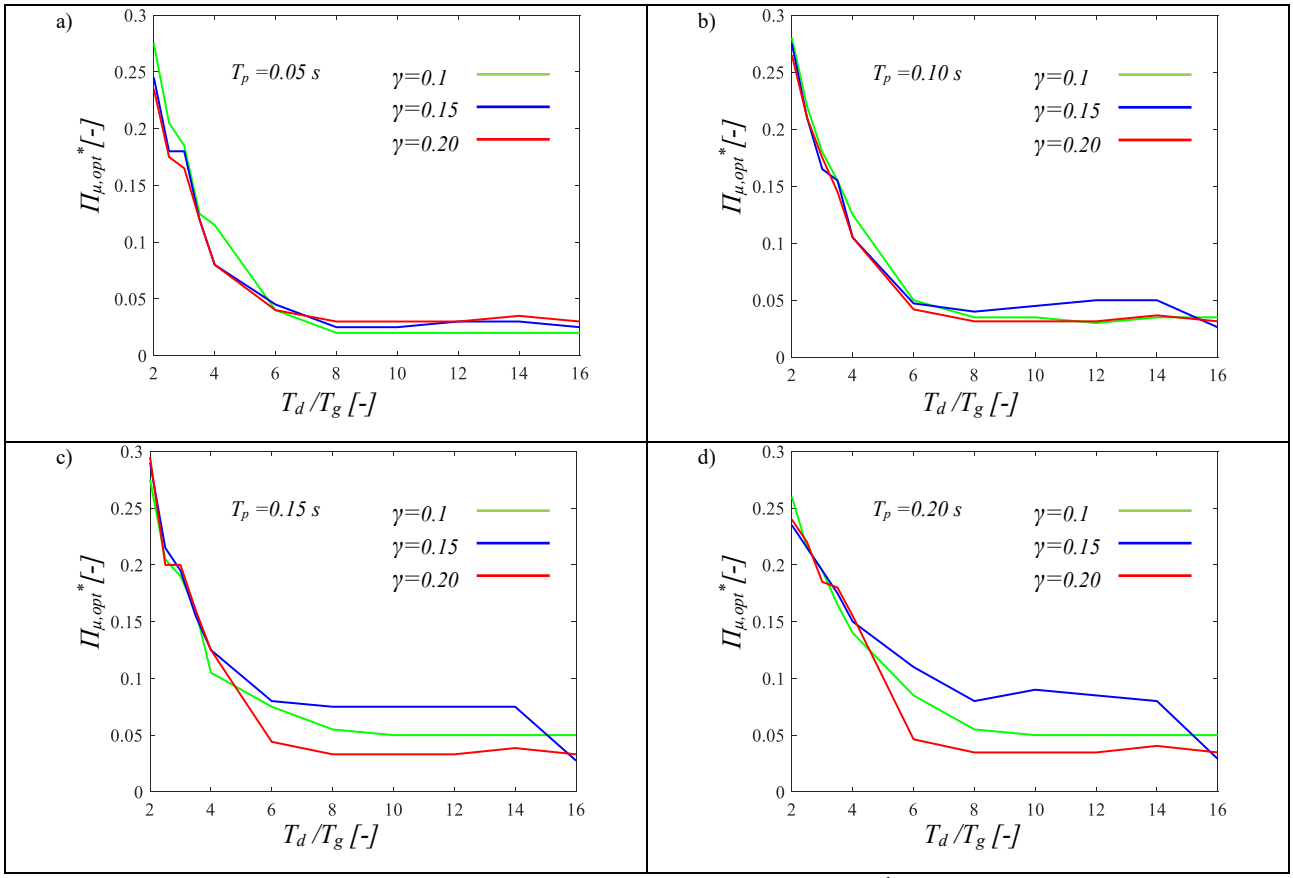


Figure 88-Optimal values of the normalized friction coefficient minimizing the 50$^{th}$ percentile of substructure response for fixed $T_p$ and varying γ, for near fault field records.

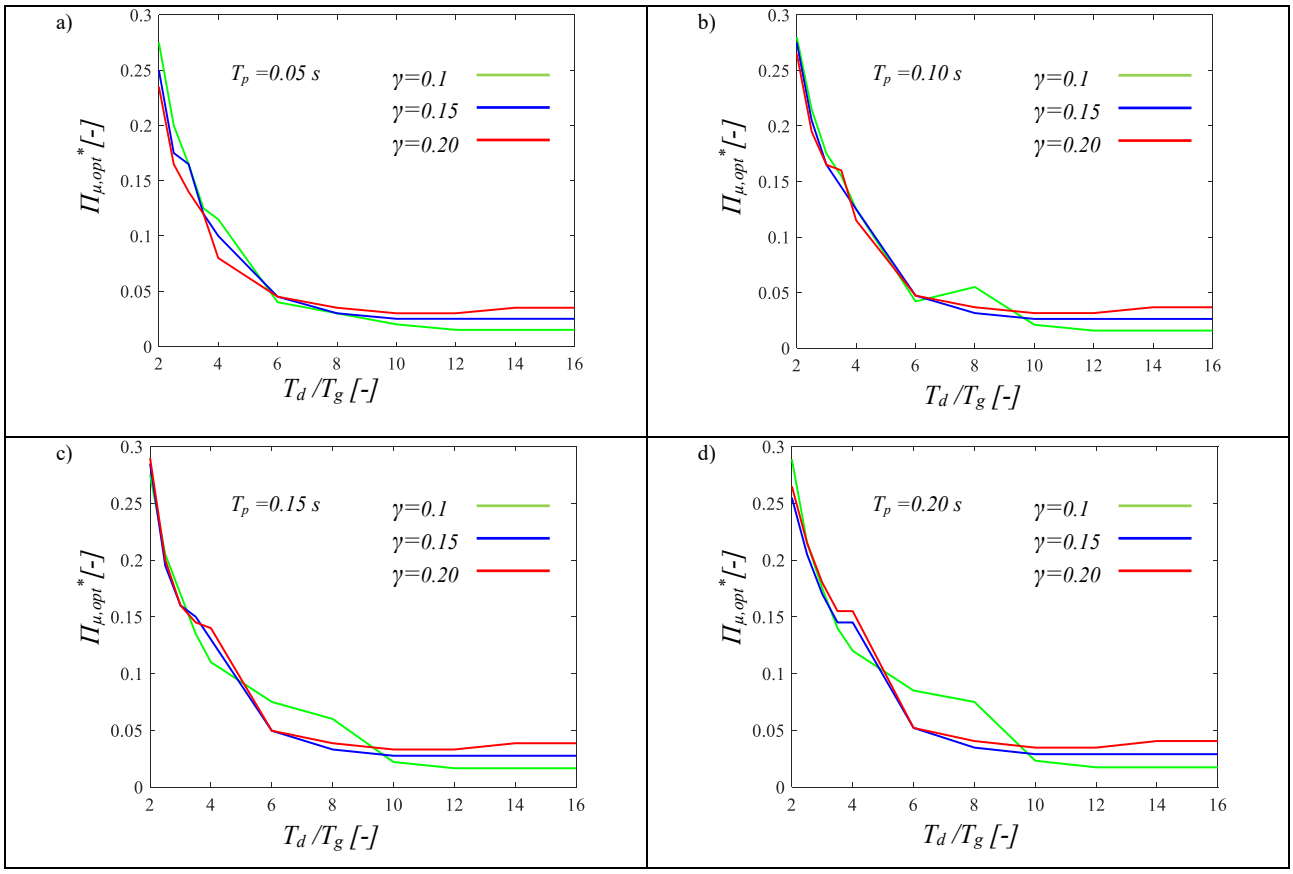


Figure 89-Optimal values of the normalized friction coefficient minimizing the 50$^{th}$ percentile of substructure response for fixed $T_p$ and varying γ, for both far field and near fault records.

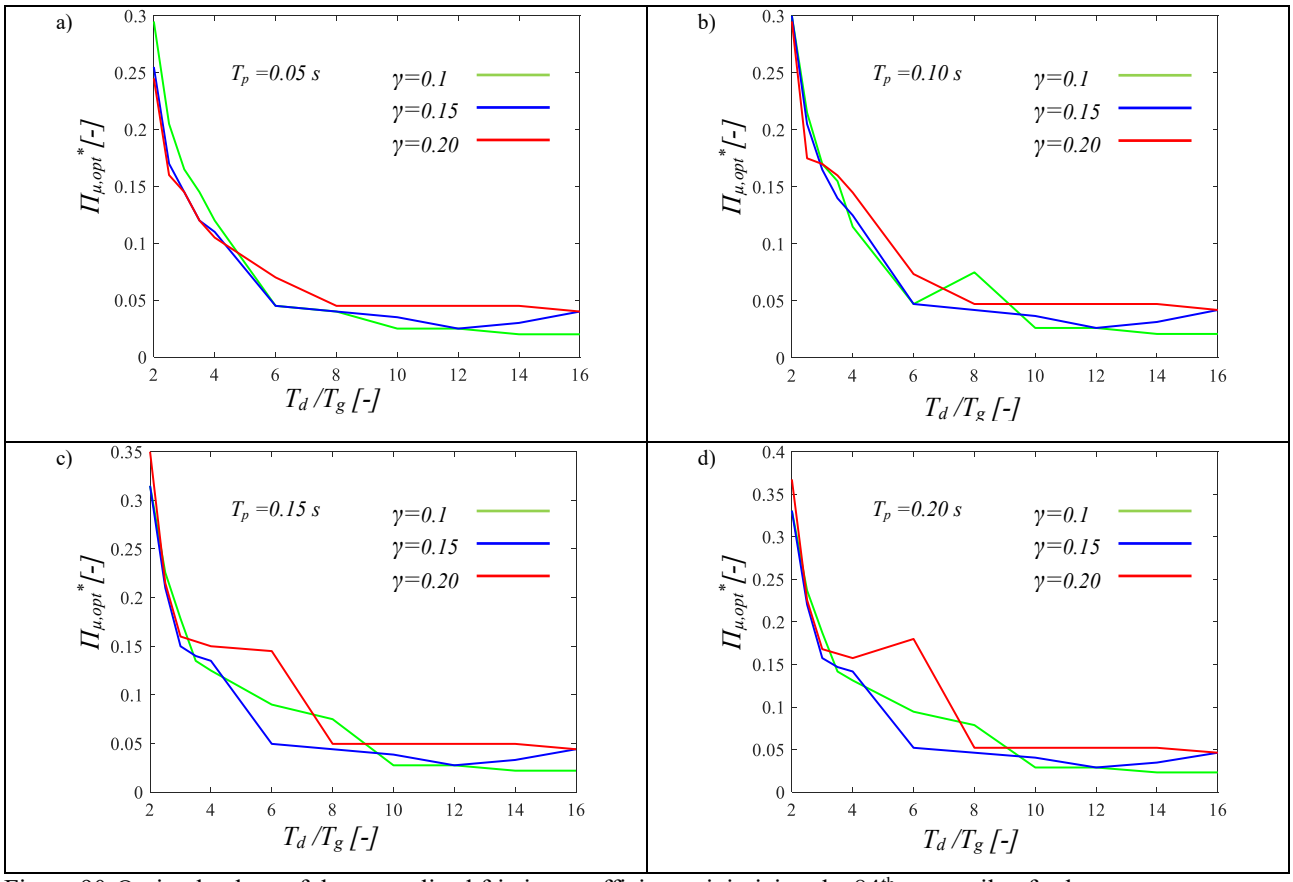


Figure 90-Optimal values of the normalized friction coefficient minimizing the 84$^{th}$ percentile of substructure response for fixed $T_p$ and varying γ, for far field records.

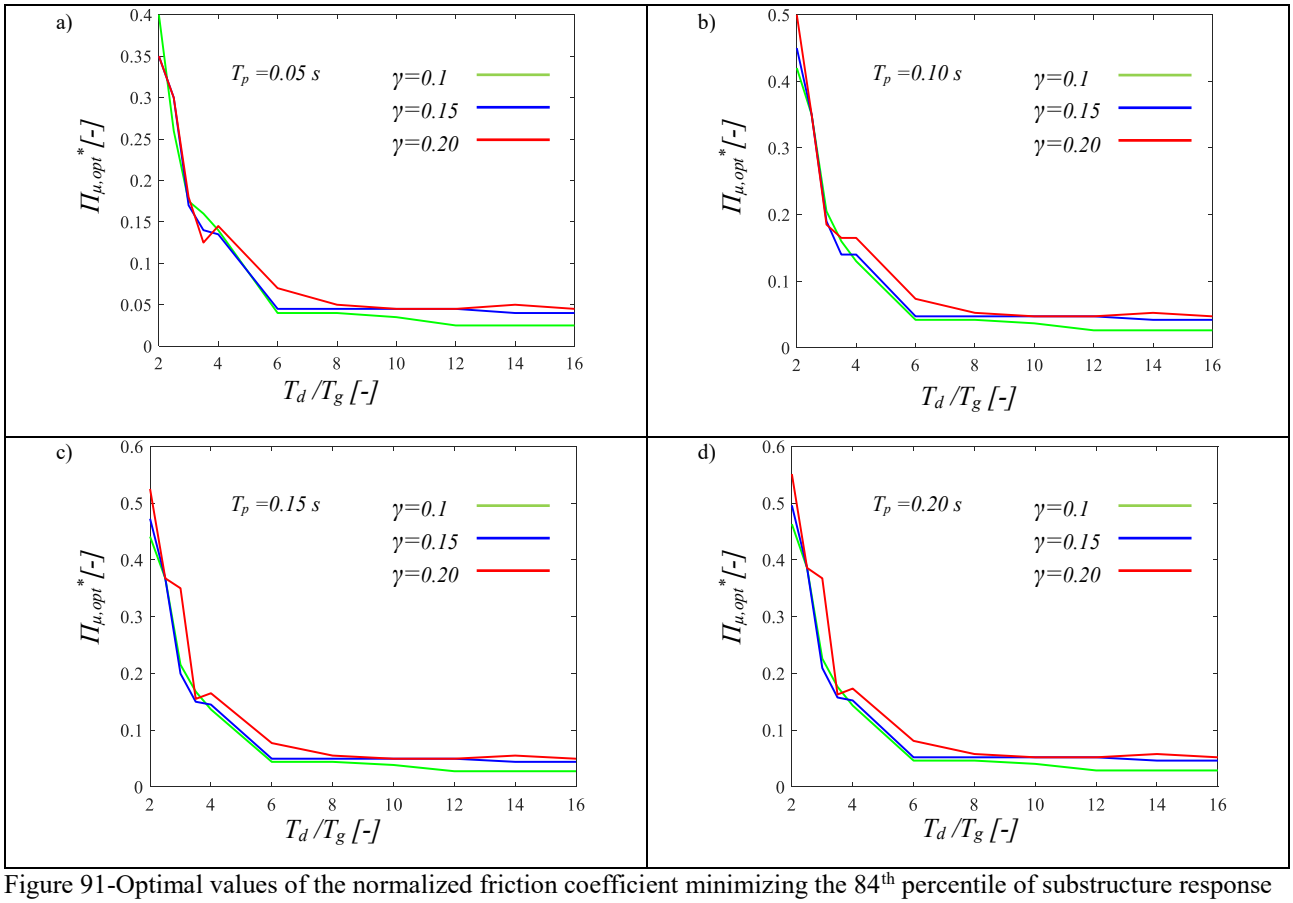


Figure 91-Optimal values of the normalized friction coefficient minimizing the 84$^{th}$ percentile of substructure response for fixed $T_p$ and varying γ, for far field records with high PGA/PGV ratios.

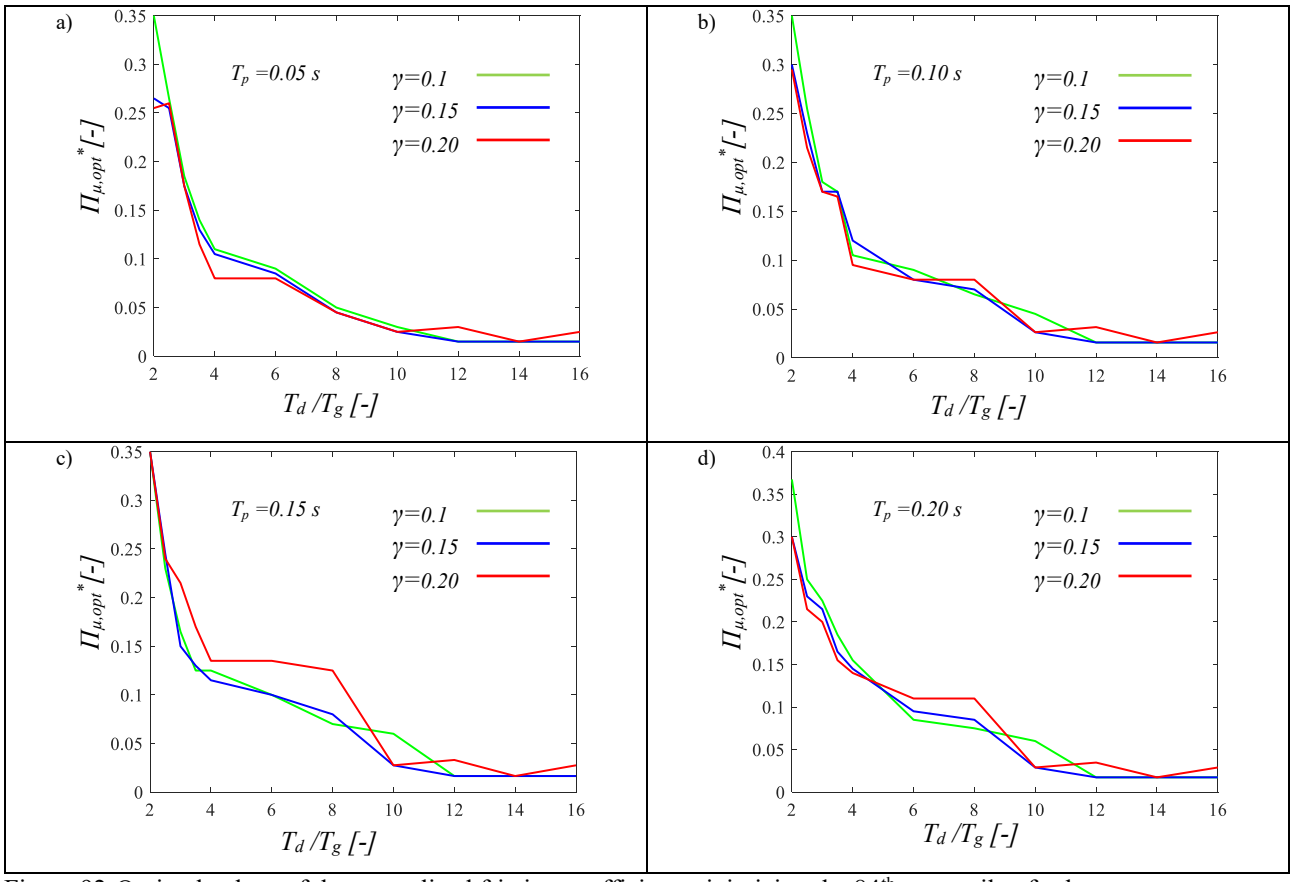


Figure 92-Optimal values of the normalized friction coefficient minimizing the 84$^{th}$ percentile of substructure response for fixed $T_p$ and varying γ, for far field records with intermediate PGA/PGV ratios.

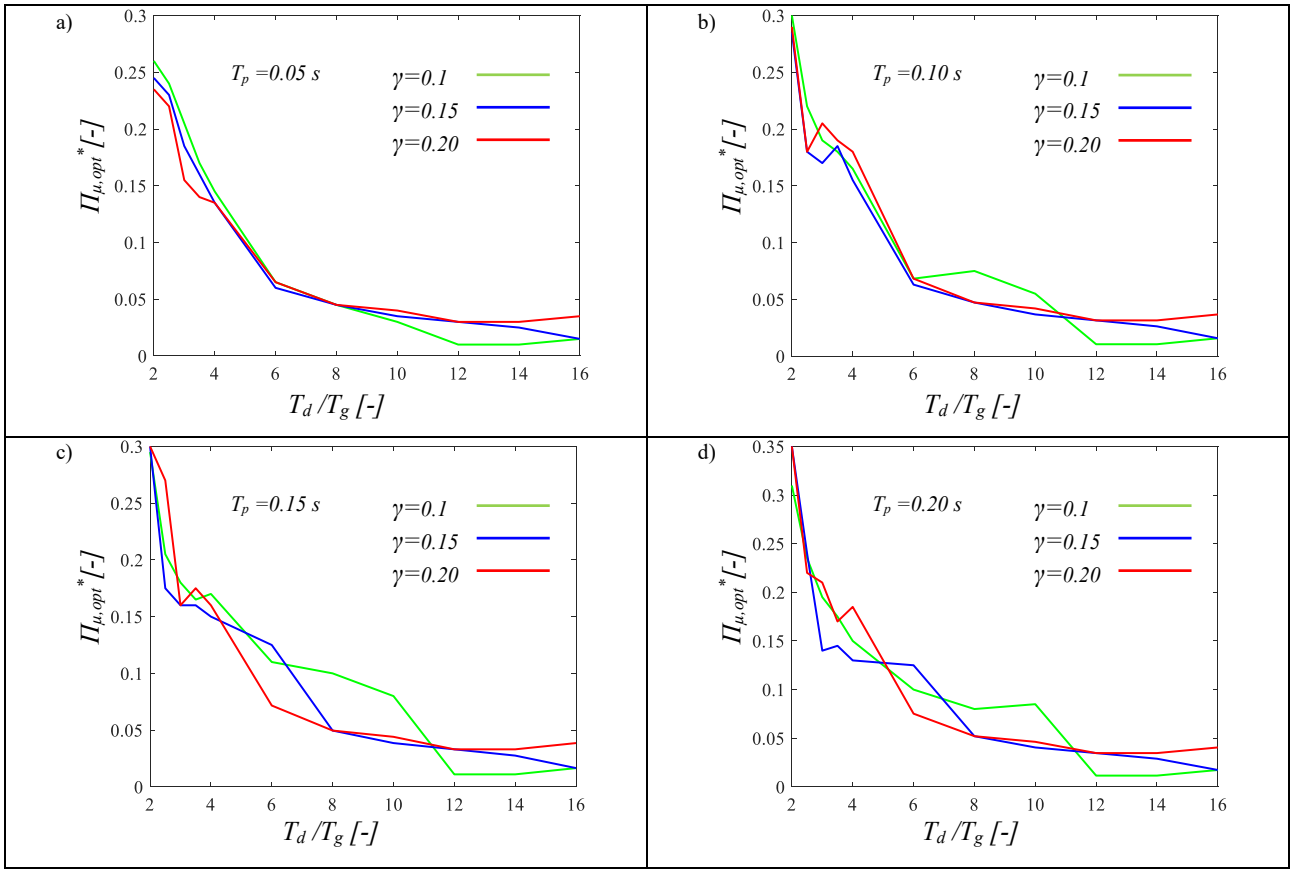


Figure 93-Optimal values of the normalized friction coefficient minimizing the 84$^{th}$ percentile of substructure response for fixed $T_p$ and varying γ, for far field records with low PGA/PGV ratios.

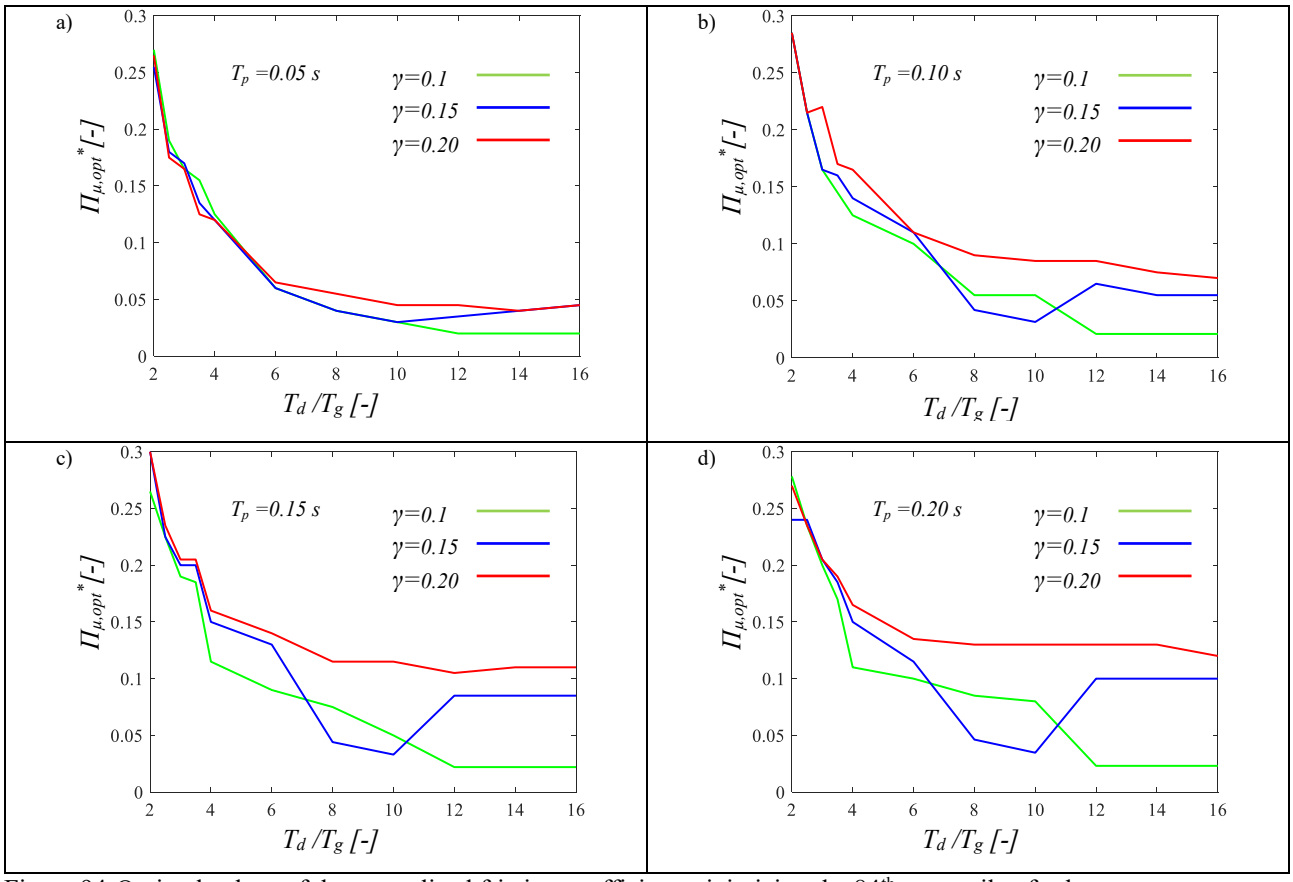


Figure 94-Optimal values of the normalized friction coefficient minimizing the 84$^{th}$ percentile of substructure response for fixed $T_p$ and varying γ, for near fault field records.

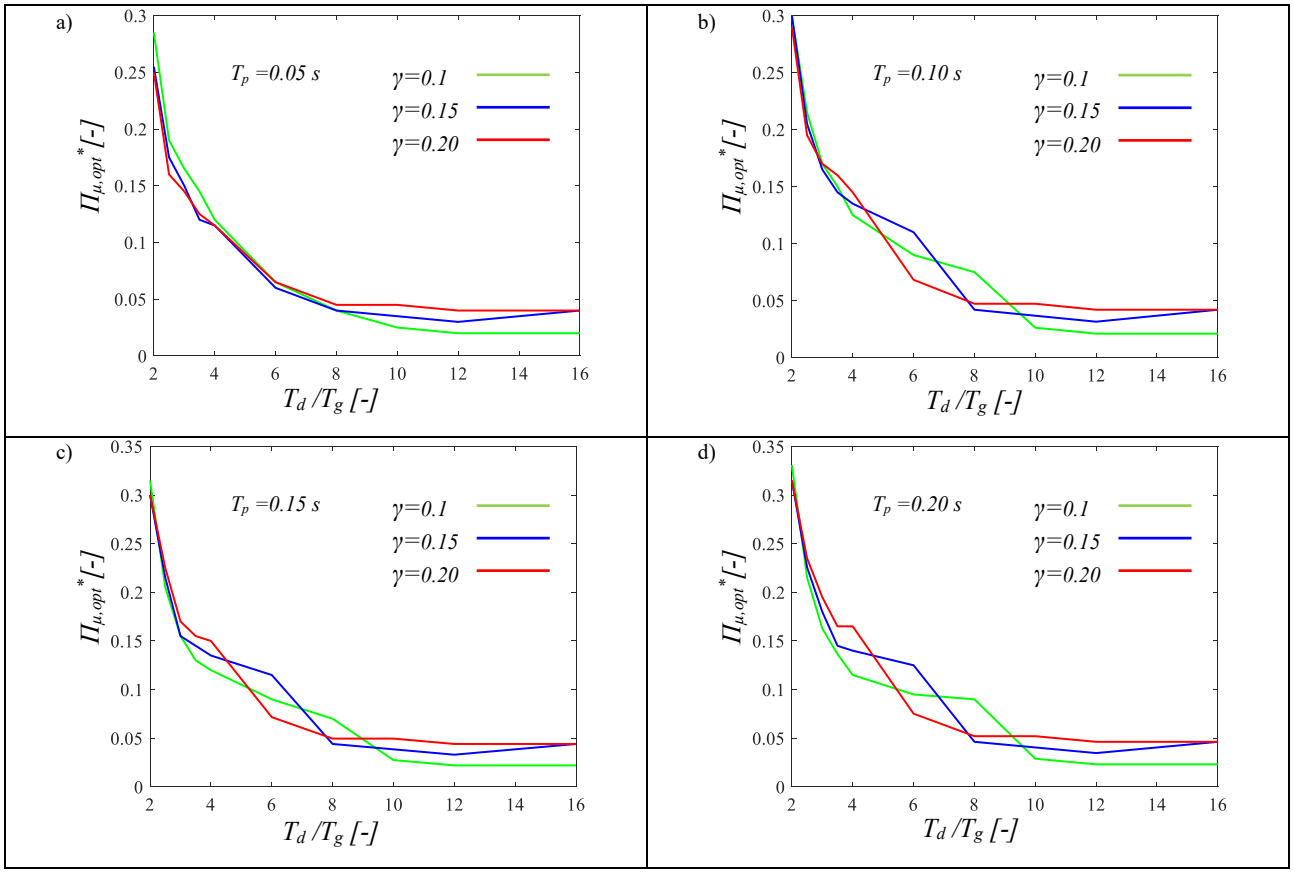


Figure 95-Optimal values of the normalized friction coefficient minimizing the 84$^{th}$ percentile of substructure response for fixed $T_p$ and varying γ, for both far field and near fault records.

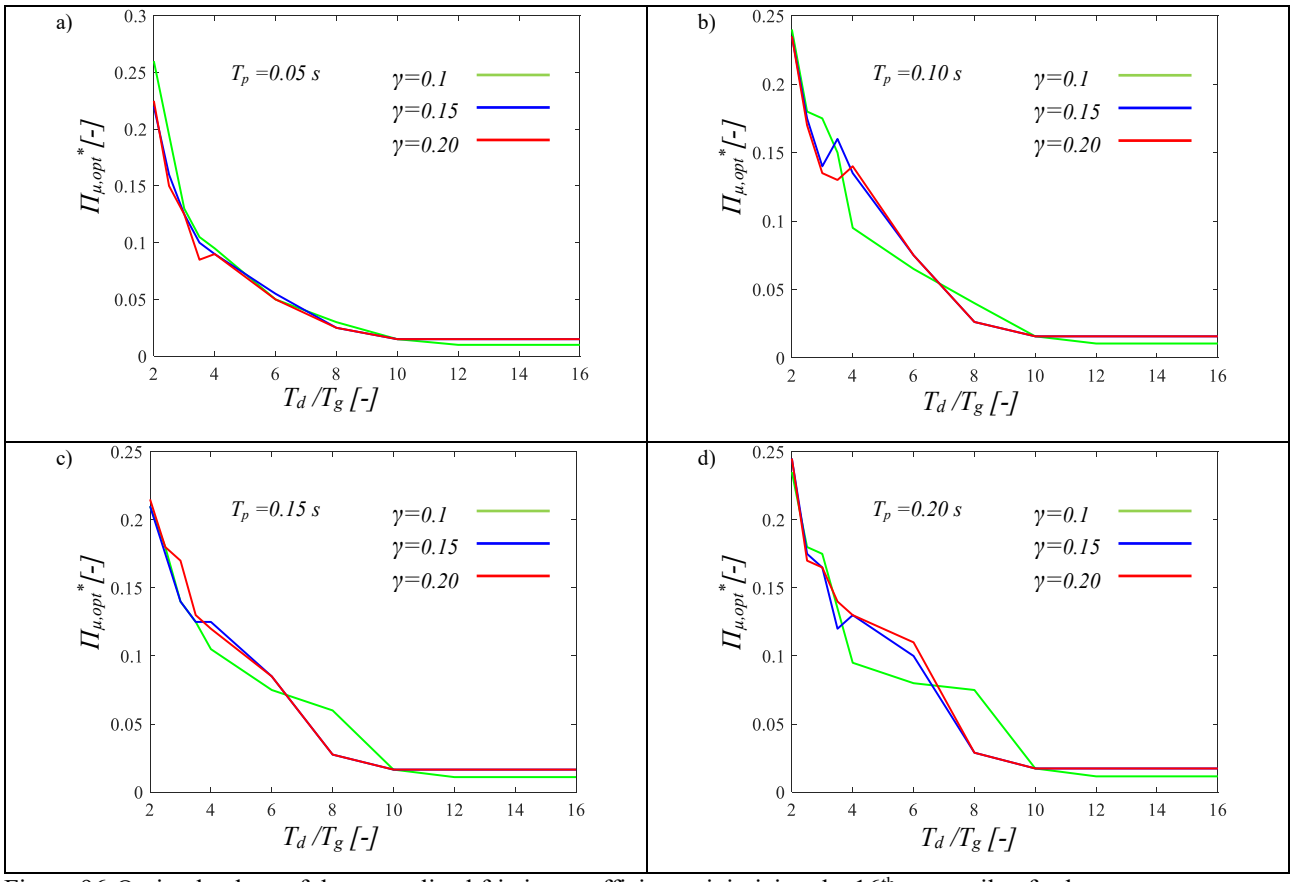


Figure 96-Optimal values of the normalized friction coefficient minimizing the 16th percentile of substructure response for fixed $T_p$ and varying γ, for far field records.

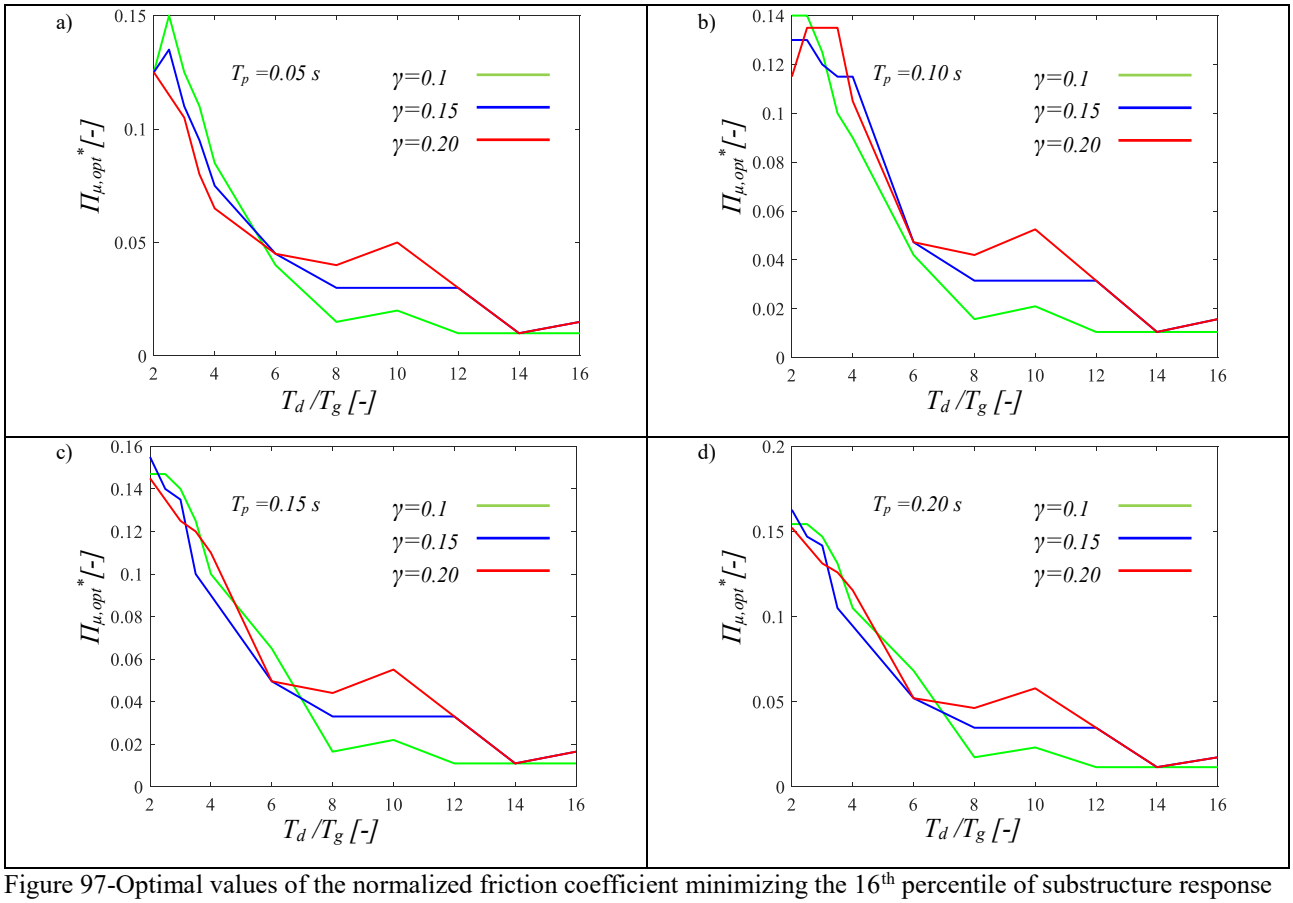


Figure 97-Optimal values of the normalized friction coefficient minimizing the 16th percentile of substructure response for fixed $T_p$ and varying γ, for far field records with high PGA/PGV ratios.

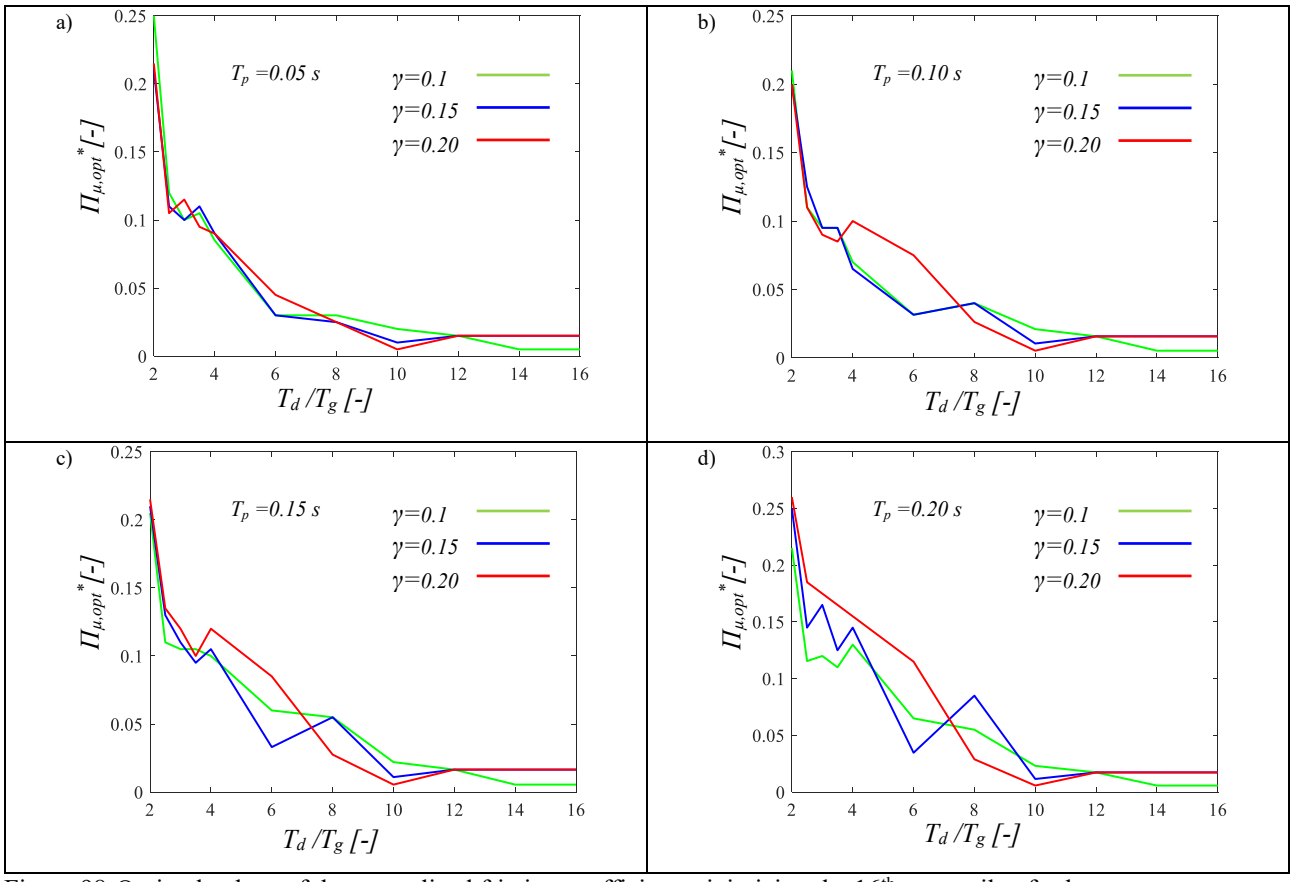


Figure 98-Optimal values of the normalized friction coefficient minimizing the 16th percentile of substructure response for fixed $T_p$ and varying γ, for far field records with intermediate PGA/PGV ratios.

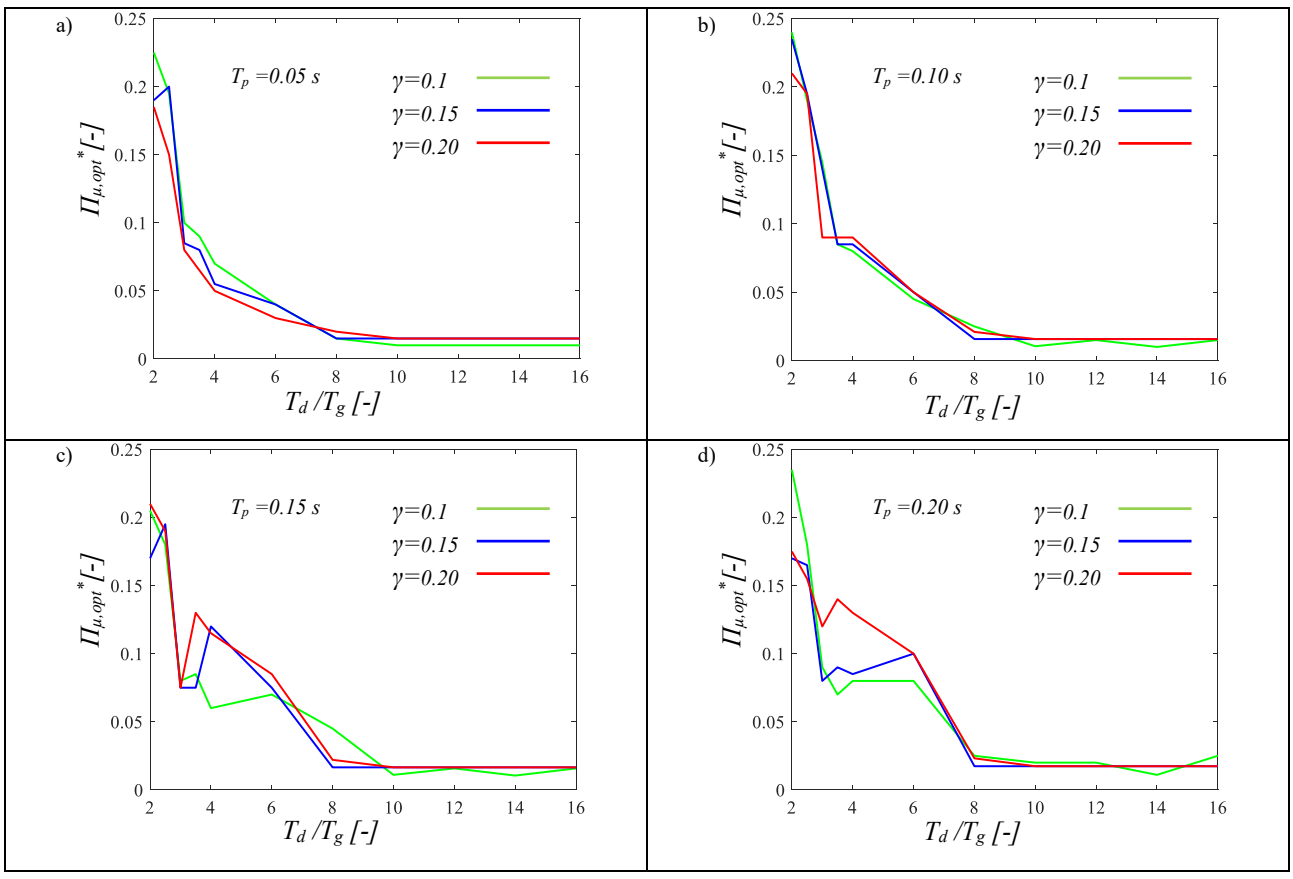


Figure 99-Optimal values of the normalized friction coefficient minimizing the 16th percentile of substructure response for fixed $T_p$ and varying γ, for far field records with low PGA/PGV ratios.

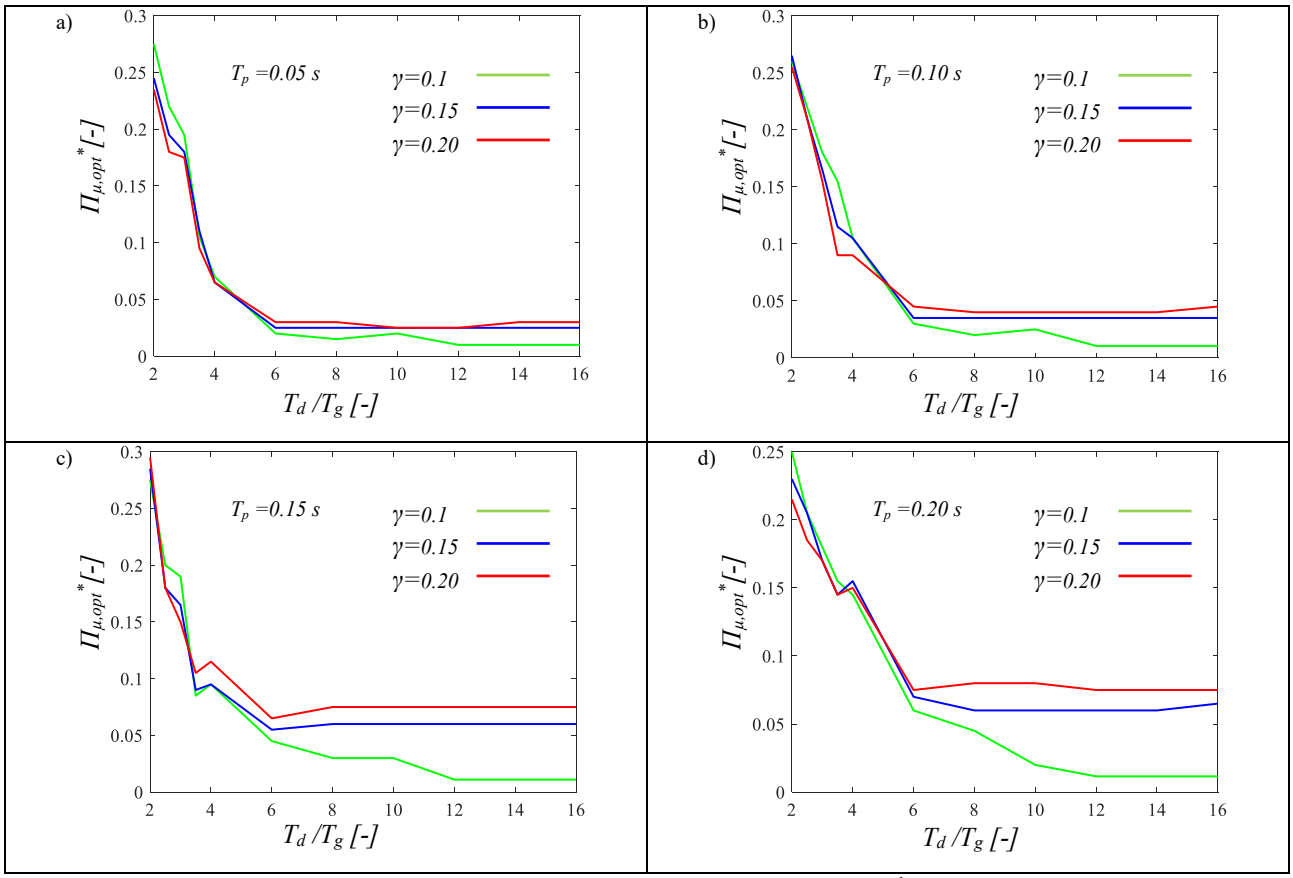


Figure 100-Optimal values of the normalized friction coefficient minimizing the 16th percentile of substructure response for fixed $T_p$ and varying γ, for near fault field records.

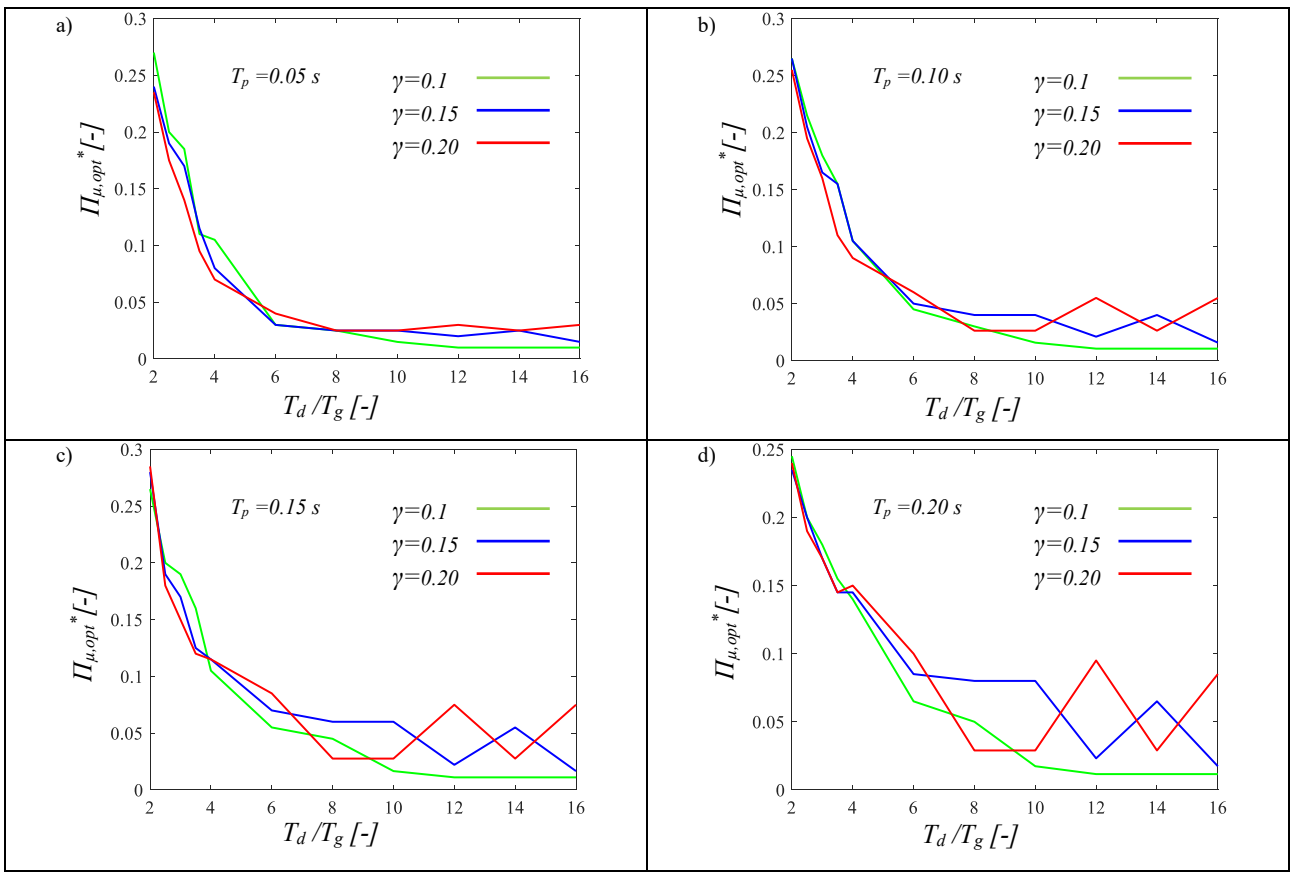


Figure 101-Optimal values of the normalized friction coefficient minimizing the 16th percentile of substructure response for fixed $T_p$ and varying γ, for both far field and near fault records.

## 12.4 Regression analysis

In this paragraph, the values of $\Pi^*_{\mu,opt}$ are recomputed by considering the response samples from both NF and FF record sets for evaluating the response statistics and a linear regression analysis is carried out to obtain a closed-form expression for $\Pi^*_{\mu,opt}$ as a function of $\Pi_{\omega_g}$, for the three percentile levels (i.e., 50$^{th}$, 84$^{th}$, and 16$^{th}$ percentiles).the regression formula is given in the following form:

$$\Pi^*_{\mu,opt} = c_1 + c_2 \cdot \Pi_{\omega_g} \geq 0 \tag{12.1}$$

where the parameters $c_1$ and $c_2$ are evaluated via Matlab. Table 1 reports the values of the coefficients of the regression expression, characterized by R-squared values of 0.97, 0.95 and 0.93 for the case of the 50$^{th}$, 84$^{th}$, and 16$^{th}$ percentiles respectively. These R-squared values are very high and demonstrate the effectiveness of the proposed regression form and the high influence of $\Pi_{\omega_g}$ on the results.

Eq. (12.1) can be used to design the optimum single concave sliding bearing properties for the isolated system, once the seismic intensity level PGA is assigned. In fact, according to the Eq. (9.10), the optimum friction coefficient can be easily calculated as:

$$\mu_{max,opt} = \frac{\Pi^*_{\mu,opt} \cdot PGA}{g}$$

This shows that the optimum friction coefficient increases linearly with the IM level.

Figs. 102a-c report the values of $\Pi^*_{\mu,opt}$ for the case, respectively, of the 50$^{th}$, 84$^{th}$ and 16$^{th}$ percentiles and the corresponding regression curves, whereas fig. 102d reports and compares the regression curves for the three percentiles considered. In figs. 102a-c the dispersion tendency of the results can be observed, described by the scatter of the values of $\Pi^*_{\mu,opt}$ with respect to the fitting curves. Therefore, the dispersion turs out to be quite high for low values of $T_d/T_g$, and it reduces for increasing values of $T_d/T_g$.

Multivariate nonlinear regression analysis is also performed to find an expression for $\psi_p(\Pi^*_{\mu,opt})$, i.e., the normalized absolute value of the peak displacement demand of the substructure corresponding to $\Pi^*_{\mu,opt}$, in function of $\Pi_\gamma$, $T_d/T_g$ and $T_p$ for the three percentile levels considered.

The expression form of $\psi_p(\Pi^*_{\mu,opt})$ is:

$$\psi_p(\Pi^*_{\mu,opt}) = c_1 + c_2 \cdot \Pi_{\omega_g} + c_3 \cdot \Pi_p + c_4 \cdot \Pi_\gamma + c_5 \cdot \Pi_{\omega_g} \cdot \Pi_p + c_6 \cdot \Pi_{\omega_g} \cdot \Pi_y + c_7 \cdot \Pi_p \cdot \Pi_y + c_8 \cdot \Pi^2{}_{\omega_g} + c_9 \cdot \Pi^2{}_p + c_{10} \cdot \Pi^2{}_\gamma$$

where $c_i$, (i=1,….,10) are the regression coefficients, whose values are reported in tables 1-2, as a function of the different percentile levels, while the multivariate nonlinear regression curves are reported in figs. 20 a-d. The regression R-squared values are 0.85, 0.88, 0.83 respectively for the 16$^{th}$, 50$^{th}$ and 84$^{th}$ percentiles.

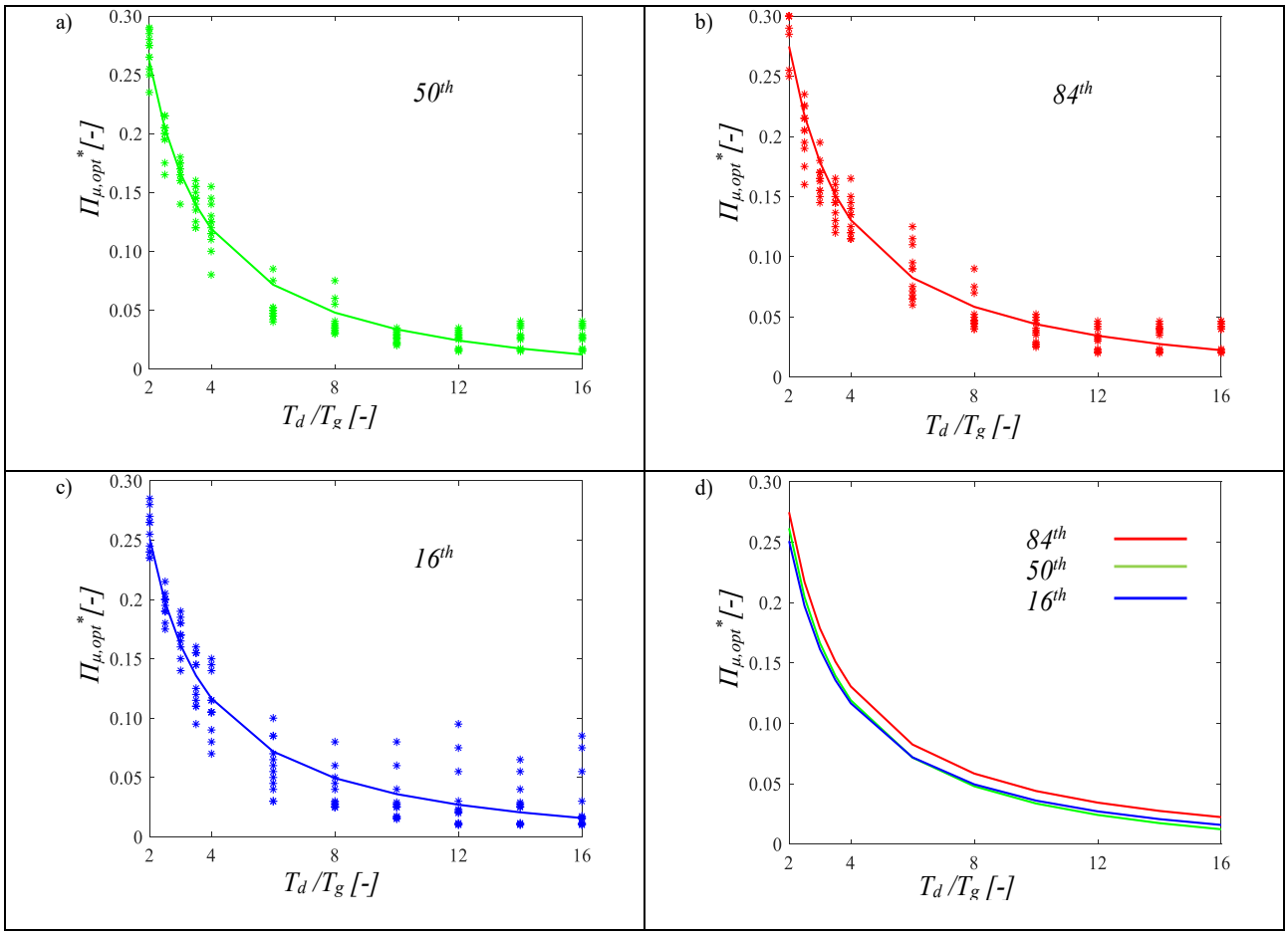


Figure 102-Optimal values of the normalized friction coefficient minimizing the 16$^{th}$ percentile of substructure response for fixed $T_p$ and varying γ, for both far field and near fault records.

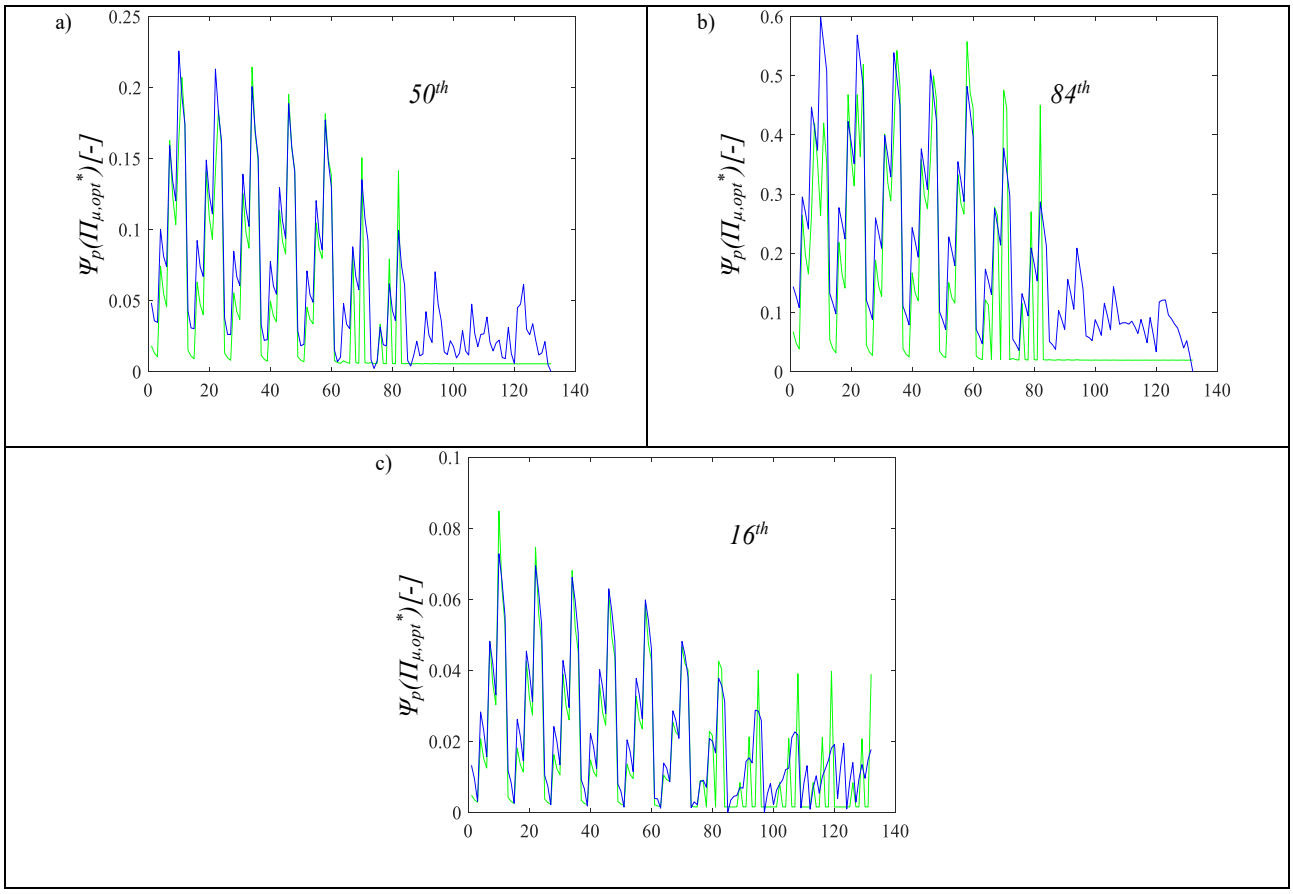


Figure 103-Comparisons of normalized absolute value of the peak displacement demand of the substructure, for all percentiles, comparisons between numerical response and estimated one, with multivariate nonlinear regression.

| | $\Pi_{50°,}$ | $\Pi_{16°,}$ | $\Pi_{84°,}$ |
|---|---|---|---|
| *R-squared* | 0.9654 | 0.9264 | 0.9517 |
| $c_1$ | -0.0234 | -0.0177 | -0.0138 |
| $c_2$ | 0.5699 | 0.5374 | 0.5774 |

Table 1: Values of linear regression coefficients for optimum normalized friction coefficient.

| | $\Psi_{50°,}$ | $\Psi_{16°,}$ | $\Psi_{84°,}$ |
|---|---|---|---|
| *R-squared* | 0.8834 | 0.8543 | 0.8309 |
| $c_1$ | 0.0546 | 0.0050 | 0.0361 |
| $c_2$ | -0.0121 | -0.0042 | -0.0215 |
| $c_3$ | 1.2592 | 0.2565 | 3.8882 |
| $c_4$ | -0.7464 | 0.0316 | -0.0776 |
| $c_5$ | -0.0957 | -0.0256 | -0.2479 |
| $c_6$ | 0.0216 | 0.0183 | 0.0278 |
| $c_7$ | -2.5186 | -0.4944 | -3.7173 |
| $c_8$ | 0.0008 | 0.0002 | 0.0016 |
| $c_9$ | 1.4619 | 0.9653 | 0.0567 |
| $c_{10}$ | 2.3050 | -0.4832 | -0.4919 |

Table 2: Values of multivariate nonlinear regression coefficients for normalized absolute peak displacement demand of the substructure.

# CONCLUSIONS

This work of thesis has investigated the relation between the ground motion characteristics and the optimal properties of single concave sliding bearings employed for the seismic isolation of structural systems. The ground motion characteristics have been described by the peak ground acceleration (PGA) and by the parameter $T_g$ related to the peak ground acceleration-to-velocity (PGA/PGV) ratio, which is known to affect significantly the structural response. These parameters have been employed to develop a non-dimensional formulation for evaluating the seismic behaviour of a six-degree-of-freedom model representative of the isolated system, by considering two different families of records corresponding to near fault and far field seismic inputs.
The result of the seismic analysis, carried out for different values of the non-dimensional parameters, characteristic of the problem, shows that:

- The ratio $T_d/T_g$ between the undamped fundamental circular frequency of the isolated system and the ground motion period affects strongly the normalized response. In particular, the geometric mean of the normalized isolator response first increases, until reaching a peak, and then it decreases, with the increasing ratio of $T_d/T_g$ (like a displacement response spectrum), whereas the geometric mean of the substructure response decreases for increasing values of $T_d/T_g$

- For the same values of the non-dimensional parameters, characterizing the system and the ground motion, the normalized isolator response under far field and near fault records are quite similar. FF records induce slightly higher displacement demands because, differently from the NF records, they are characterized by multiple cycles of large amplitudes rather than a single pulse. Whereas, the normalized substructure response shows a similar trend among the record sets but a relatively high dispersion with displacement response values varying in the order of ten times, nevertheless the optimum normalized friction coefficient turns to be independent to record sets.
  This similarity has been observed also for the three subsets of far field records having different PGA/PGV ratios.

- There exists an optimal value of the normalized friction coefficient that minimizes the normalized substructure displacement response. This optimal value decreases significantly

by increasing $T_d/T_g$, and it is only slightly affected by the other non-dimensional parameters.

- The proposed nondimensionalization of the problem confirms the findings of other studies that the optimal friction coefficient increases linearly with the seismic intensity level. Thus, higher values of friction are required to achieve the same response reduction under earthquakes with higher intensity.

In the final part of the work, regression expressions have been derived for the optimal values of the normalized friction coefficient minimizing the $50^{th}$, $16^{th}$ and $84^{th}$ percentile values of the normalized substructure displacements, as function of the identified system characteristic parameters and ground motion ones. These equations can be very useful for the preliminary design of the optimal single concave sliding bearing properties by also accounting for the influence of ground motion characteristics and demonstrate the high influence of the ratio $T_d/T_g$.

# REFERENCES


[1] Assemblea Generale del Consiglio Superiore dei lavori pubblici. (2008). "NUOVE NORME TECNICHE PER LE COSTRUZIONI". Gazzetta Ufficiale n. 29.

[2] Progetto DPC-INGV S1. (2016). Retrieved from http://esse1-gis.mi.ingv.it/

[3] M. C. Constantinou, A. S. Whittaker, Y. Kalpakidis, D. M. Fenz, G. P. Warn (2007), "PERFORMANCE OF SEISMIC ISOLATION HARDWARE UNDER SERVICE AND SEISMIC LOADING", Technical Report MCEER 07-0012, 2007.

[4] M. Dolce, D. Cardone, F. Croatto (2005), "FRICTIONAL BEHAVIOR OF STEEL – PTFE INTERFACES FOR SEISMIC ISOLATION", Springer, Bullettin of Earthquake Engeneering.

[5] Mokha, Constantinou, Reinhorn (1991). "TEFLON BEARINGS IN BASE ISOLATION. II. TESTING", J. Struct. Eng.

[6] Mokha, Constantinou, Reinhorn (1990). "TEFLON BEARINGS IN BASE ISOLATION. I. MODELLING", J. Struct. Eng.

[7] R. S. Jangid (2008), "STOCHASTIC RESPONSE OF BRIDGES SEISMICALLY ISOLATED BY FRICTION PENDULUM SYSTEM", Journal of Bridge Engineering.

[8] Priestley, Seible, Calvi (1996). "SEISMIC DESIGN AND RETROFIT OF BRIDGES".

[9] Zayas, V. A., Low, S. S., and Mahin, S. A. (1990), "A SIMPLE PENDULUM TECHNIQUE FOR ACHIEVING SIESMIC ISOLARTION", Earthquake Spectra, 6(2), 317 – 333.

[10] Makris, N., Black, C. J. (2003). "Dimensional Analysis of Inelastic Structures Subjected to Near Fault Ground Motions". Technical Report: EERC 2003/05. Earthquake Engineering Research Center, University of California, Berkeley.

[11] Makris, N., and Black, C. J. (2004). "Dimensional analysis of bilinear oscillators under pulse-type excitations." J. Eng. Mech., 130(9), 1019–1031.

[12] Karavasilis TL, Seo CY, Makris N. Dimensional Response Analysis of Bilinear Systems Subjected to Non-pulse like Earthquake Ground Motions. *Journal of Structural Engineering* 2011; **137**(5): 600–606.

[13] Dimitrakopoulos, E., Kappos, A. J., & Makris, N. (2009). Dimensional analysis of yielding and pounding structures for records without distinct pulses. Soil dynamics and earthquake engineering, 29(7), 1170-1180.

[14] Málaga-Chuquitaype, C. (2015). Estimation of peak displacements in steel structures through dimensional analysis and the efficiency of alternative ground-motion time and length scales. *Engineering Structures*, 101, 264-278.

[15] Tubaldi E., Dall'Asta, A. (2012). Transverse free vibrations of continuous bridges with abutment restraint. Earthquake Engineering & Structural Dynamics, 41(9): 1319-1340.

[16] Tubaldi E. (2015). Dynamic behavior of adjacent buildings connected by linear viscous/viscoelastic dampers. Structural Control and Health Monitoring, 22(8): 1086-1102.

[17] Makris N., Kampas G. (2016). Size versus Slenderness: Two Competing Parameters in the Seismic Stability of Free-Standing Rocking Columns, Bulletin of the Seismological Society of America, 106(1), DOI10.1785/01.

[18] Makris, N., Vassiliou M.F. (2011). The Existence of "Complete Similarities" in the Response of Seismic Isolated Structures and their Implication in Design. Earthquake Engineering and Structural Dynamics, 40(10):1103-1121.

[19] Vassiliou, M.F., Makris, N. (2012). Analysis of the rocking response of rigid blocks standing free on a seismically isolated base. Earthquake Eng. & Structural Dynamics, 41(2): 177-196.

[20] Castaldo, P, Tubaldi, E. Influence of ground motion characteristics on the optimal single concave sliding bearing properties for base-isolated structures. *Soil dynamics and earthquake engineering 104* 2018;
[21] Castaldo, P, Tubaldi, E. Influence of fps bearing properties on the seismic performance of base-isolated structures. *Earthquake Engineering and Structural Dynamics* 2015; **44**(15):2817–2836.
[22] Castaldo P., Amendola G., Palazzo B., Seismic fragility and reliability of structures isolated by friction pendulum devices: seismic reliability-based design (SRBD), *Earthquake Engineering and Structural Dynamics* 2017, **46**(3); 425–446, DOI: 10.1002/eqe.2798.
[23] Fragiacomo, M., Rajgelj, S., & Cimadom, F. (2003). Design of bilinear hysteretic isolation systems. Earthquake engineering & structural dynamics, 32(9), 1333-1352.
[24] Katsanos, E. I., Sextos, A. G., & Manolis, G. D. (2010). Selection of earthquake ground motion records: A state-of-the-art review from a structural engineering perspective. *Soil Dynamics and Earthquake Engineering*, *30*(4), 157-169.
[25] Dicleli, M., & Buddaram, S. (2006). Effect of isolator and ground motion characteristics on the performance of seismic-isolated bridges. *Earthquake engineering & structural dynamics*, *35*(2), 233-250.
[26] Liao, W. I., Loh, C. H., & Lee, B. H. (2004). Comparison of dynamic response of isolated and non-isolated continuous girder bridges subjected to near-fault ground motions. *Engineering Structures*, *26*(14), 2173-2183.
[27] Hameed, A., Koo, M. S., Dai Do, T., & Jeong, J. H. (2008). Effect of lead rubber bearing characteristics on the response of seismic-isolated bridges. *KSCE Journal of Civil Engineering*, *12*(3), 187-196.
[28] Zhu, T.J., Tso, W.K., and Heidebrecht, A.C. (1988). "Effect of peak ground A/V ratio on structural damage." *Journal of Structural Engineering*, Vol. 114, pp. 1019–1037.
[29] Tso, W. K., Zhu, T. J., & Heidebrecht, A. C. (1992). Engineering implication of ground motion A/V ratio. *Soil Dynamics and Earthquake Engineering*, 11(3), 133-144.
[30] Sawada T, Hirao K, Yamamoto H, Tsujihara O. Relation between maximum amplitude ratio and spectral parameters of earthquake ground motion. In: Proc. 10th world conf. on earthquake engineering, vol. 2. 1992, p. 617–22.
[31] F. Pavel & D. Lungu (2013) Correlations Between Frequency Content Indicators of Strong Ground Motions and PGV, Journal of Earthquake Engineering, 17:4, 543-559.
[32] Jafarian, Y., Kermani, E., & Baziar, M. H. (2010). Empirical predictive model for the v max/a max ratio of strong ground motions using genetic programming. *Computers & Geosciences*, 36(12), 1523-1531.
[33] Rathje, E. M., Faraj, F., Russell, S., and Bray, J. D. (2004). "Empirical relationships for frequency content parameters of earthquake ground motions." Earthquake Spectra, 20(1), 119–144.
[34] Castaldo P., Ripani M. Optimal design of friction pendulum system properties for isolated structures considering different soil conditions. *Soil Dynamics and Earthquake Engineering* 2016; 90:74–87. DOI:10.1016/j.soildyn.2016.08.025.
[35] Vassiliou F M, Tsiavos A, Stojadinović B. Dynamics of inelastic base-isolated structures subjected to analytical pulse ground motions. *Earthquake Engineering & Structural Dynamics*, 2013;**42**(14): 2043–2060.
[36] Porter KA. An overview of PEER's performance-based earthquake engineering methodology. Proceedings, *Proceedings of the 9th International Conference on Application of Statistics and Probability in Civil Engineering* (*ICASP9*), San Francisco, California, 2003.
[37] Luco N, Cornell CA. Structure-specific scalar intensity measures for near-source and ordinary earthquake ground motions. *Earthquake Spectra* 2007; **23**(2): 357-92.
[38] Jangid RS. Optimum frictional elements in sliding isolation systems. *Computers and Structures* 2000; **76**(5): 651–661.

[39] Jangid RS. Optimum friction pendulum system for near-fault motions. *Engineering Structures*

2005; 27(3): 349–359.
[40] Fragiacomo, M., Rajgelj, S., & Cimadom, F. (2003). Design of bilinear hysteretic isolation systems. Earthquake engineering & structural dynamics, 32(9), 1333-1352.
[41] Iemura H, Taghikhany T, Jain S. Optimum design of resilient sliding isolation system for seismic protection of equipments. *Bulletin of Earthquake Engineering* 2007; **5**(1):85–103.
[42] Pinto PE, Giannini R, Franchin P. *Seismic Reliability Analysis of Structures*, IUSS Press, Pavia, Italy, 2003.
[43] Ryan K, Chopra A. Estimation of Seismic Demands on Isolators Based on Nonlinear Analysis. *Journal of Structural Engineering* 2004; **130**(3): 392–402.
[44] Mollaioli F, Lucchini A, Cheng Y, Monti G. Intensity measures for the seismic response prediction of base-isolated buildings. *Bulletin of Earthquake Eng.* 2013; **11**(5): 1841–1866.